Available online at www.sciencedirect.com

SciVerse ScienceDirect

Solar Energy 95 (2013) 392–430

SOLAR ENERGY

www.elsevier.com/locate/solener

Review

Equipment and methodologies for cloud detection and classification: A review

R. Tapakis, A.G. Charalambides *

Cyprus University of Technology, Department of Environmental Science and Technology, Lemesos 3603, Cyprus

Received 3 May 2012; received in revised form 28 August 2012; accepted 25 November 2012
Available online 29 December 2012

Communicated by: Associate Editor David Renne

Abstract

The penetration and acceptance of Renewable Energy Systems (RESs) has already taken place in our lives. Solar energy is the feedstock/source for various applications of RES, and thus, the knowledge of the intensity of the incident solar irradiance is essential for monitoring the performance of such systems. A lot of experimental work and modeling has already been conducted for calculating solar irradiance due to various factors, such as location and season. The major unpredictable factor in defining the solar irradiance and the

Abbreviations: AATSR, Advanced Along Track Scanning Radiometer; Ac, Altocumulus; AI, Artificial Intelligence; ALOS, Land Observation Satellite; AMI, Active Microwave Instrument; AMSU, Advanced Microwave Sounding Unit; ANNs, Artificial Neural Networks; As, Altostratus; ASIVA, All Sky Infrared Visible Analyzer; ATSR, Along-Track Scanning Radiometer; AVHRR, Advanced Very High Resolution Radiometer; AVNIR-2, Advanced Visible and Near Infrared Radiometer type 2; BCT, Bispectral Composite Threshold; BMSs, Building Management Systems; BPNN, Back Propagation Neural Network; CALIOP, Cloud-Aerosol LIDAR with Orthogonal Polarization; CALIPSO, Cloud-Aerosol LIDAR and Infrared Pathfinder Satellite Observation; CART, Cloud And Radiation Testbed; Cb, Cumulonimbus; CBH, Cloud Base Height; CTH, Cloud Top Height; Cc, Cirrocumulus; CCD, Charge Coupled Device; CERES, Clouds and Earth's Radiant Energy System; Ci, Cirrus; CMOS, Complementary Metal Oxide Semiconductor; CNES, Centre National d' Etudes Spatiales; Cs, Cirrostratus; Cu, Cumulus; DGR, Diffuse to Global irradiance Ratio; DMSP, Defense Meteorological Satellite Program; DNI, Direct Normal Irradiance; EMCCD, Electron Multiplying Charge Coupled Devise; ERS, European Remote Sensing; ETM+, Enhanced Thematic Mapper plus; EUMETSAT, EuropeanOrganisation for the exploitation of METeorologicalSATellites; FL, Fuzzy Logic; FOV, Field Of View; FY, Fengyun; GLCMs, Gray Level Co-occurrence Matrices; GMS, Geostationary Meteorological Satellite; GOESs, Geostationary Operational Environmental Satellites; GOME, Global Ozone Monitoring Experiment; GOMO, Global Ozone Monitoring by Occultation of Stars; GPS, Global Positioning System; HAD, Heteroscedastic Discriminant Analysis; ICI, Infrared Cloud Imager; IHS, Intensity, Hue, and Saturation space; IIR, Imaging Infrared Radiometer; IR, Infrared; IRAS, Infrared Spectrometer; IRR, IR Radiometer; JAXA, Japan Aerospace Exploration Agency; k-nn, k-nearest neighbor; LDA, Linear Discriminant Analysis; LIDAR, Light Detection And Ranging; LW, longwave; MERIS, MEdium Resolution Imaging Spectrometer; MFRSR, Multi-Filter-Rotating Shadowband Radiometer; MISR, Multi-angle Imaging SpectroRadiometer; MLP, MultiLayer Perceptron; MMCR, MilliMeter wave Cloud Radar; MMWR, MilliMeter Wave Radars; MODIS, Moderate Resolution Imaging Spectroradiometer; MOS-1, Marine Observation Satellite 1; MPL, micropulse; MS, Microwave Sounder; MSG, Meteosat Second Generation; MTP, Meteosat Transition Programme; MTSAT, Multifunctional Transport Satellites; MW, MicroWave; MWR, MicroWave Radiometer; NASA, National Aeronautics and Space Administration; NIR, Near IR; NOAA, National Oceanic and Atmospheric Administration; Ns, Nimbostratus; OMI, Ozone Monitoring Instrument; PCA, Principal Component Analysis; PNNs, probabilistic neural networks; POES, Polar Operational Environmental Satellite; PV, photovoltaic; QDA, Quadratic Discriminant Analysis; R/B, Ratio Red/Blue; RES, Renewable Energy Systems; RGB, Red-Green-Blue; RH, Relative Humidity; RNNs, Recurrent Neural Networks; ROI, Region Of Interest; RSS, Rotating Shawdowband Spectroradiometer; Sc, Stratocumulus; SEVIRI, Spinning Enhanced Visible and Infrared Imager; SGP, Southern Great Plains; SMSs, Synchronous Meteorological Satellites; SOM, Self-Organizing Map; SSM/I, Special Sensor Microwave Imager; SST, Sea Surface Temperature; St, Stratus; SVM, Support Vector Machine; SW, shortwave; T_b, Brightness Temperature; TIROS, Television InfraRed Observation Satellite-#; TMI, TRMM Microwave Imager; TRMM, Tropical Rainfall Measuring Mission; TUVR, Total Ultraviolet Radiometer; UFSCM, Unit-Feature Spatial Classification Method; UFS, Unit Feature Space; UV, ultraviolet; VHRR, Very high Resolution Radiometer; VIRR, Visible and InfraRed Radiometer; VIRS, Visible Infrared Scanner; VIS, visible; VISSR, Visible and Infrared Spin Scan Radiometer; VTIR, Visible and Thermal Infrared Radiometer; WFC, Wide Field Camera; WMO, World Meteorological Organization; WSI, Whole Sky Imager; WSIRCMS, Whole Sky Infra Red Cloud Measuring System; WV, Water Vapor.

* Corresponding author. Address: Corner of Athinon and Anexartisias, 57, Lemesos 3603, Cyprus. Tel.: +357 25 002306; fax: +357 25 002668.
E-mail address: a.charalambides@cut.ac.cy (A.G. Charalambides).

http://dx.doi.org/10.1016/j.solener.2012.11.015

performance of solar systems is the presence of clouds in the sky. So far, various researchers proposed several models for estimating solar irradiance in correlation with cloud coverage and cloud type. This paper reviews the up-to-date research in automatic cloud detection and classification. It initiates with a brief introduction to clouds types and classification. Then, a detailed description of the equipment used for the measurements is provided, either ground based or satellite integrated. Finally, it concludes with an analysis of the existing algorithms for cloud classification, including a presentation of the up-to-date experimental results.

Keywords: Clouds; Automatic cloud classification; Solar irradiance

Contents

1. Introduction

During the past few years, there has been major progress in the use of solar technologies (Thirugnanasambandam et al., 2010), especially as Renewable Energy Systems (RESs) for the production of electricity. Such technologies include residential and large scale photovoltaic (PV) parks (El Chaar et al., 2011; Parida et al., 2011), solar troughs and solar tower power plants (Barlev et al., 2011), solar dish technologies (Kongtragool and Wongwises, 2003) and the upcoming construction of commercial solar updraft towers (Pretorius and Kroger, 2006; Zhou et al., 2010). Still, solar RES have not yet achieved high penetration in the energy sector compared to the existing fossil fuel power plants mainly due to their dependency on the sun's irradiance and in most cases, due to the lack of affordable storage options. In the case of concentrating PVs for example, the energy production is severely reduced in the presence of clouds "in front" of the sun due to their exclusive dependence on direct radiation (Parida et al., 2011). A temporal independence from solar irradiance can only be achieved in solar thermal power plants, using thermal storage; yet, this solution leads to higher construction cost. By now, most of the solar thermal power plants employ a

thermal storage medium in order to stabilize the instantaneous variations between the load and the alternating solar energy, improving the system operability and stability. However, the variable feed-in tariff option motivates the operators of solar thermal power plants to optimize the plant's performance over maximum profit (Wittmann et al., 2008). Consequently, the knowledge of, and the ability to predict the amount of solar irradiance is essential for planning an optimized operation strategy of the plant (Eck and Hirsch, 2007; Herrmann et al., 2004; Medrano et al., 2010; Sharma et al., 2009).

The continuous development of technologies that use solar energy, leads to the need of accurate knowledge of the amount of the incident solar irradiance on the surface of the earth. This will enable for: (1) the prediction of the energy output of the systems, (2) the regulation of the systems, (3) better design of the systems and the possible energy storage units, (4) resource assessment calculations for a specific area and finally, (5) increased profit given structure of energy markets.

Several researchers have proposed various models to calculate the solar irradiance, either based on the Angstrom equation (Angstrom, 1924) or other more complex models based on various parameters. The main parameters (used for the computation of solar irradiance) that affect the value of average daily global solar irradiance are: (1) extraterrestrial radiation, (2) solar declination, (3) ratio of sunshine duration (day length over maximum possible sunshine duration), (4) air temperature, (5) earth surface albedo, (6) relative humidity, (7) cloudiness, (8) precipitation, (9) evaporation, (10) atmospheric composition, (11) aerosol optical depth, (12) geographical location and (13) Soil Temperature (Ahmad and Tiwari, 2011; Ulgen and Hepbasli, 2004).

From these parameters, the most profound parameter for solar irradiance variations is cloudiness, because although it can be predicted, the spatial and temporal resolution of the predictions is very low, resulting to an uncertainty in solar energy generation prediction, especially for Solar Power Systems without energy storage, such as PV parks (Mills et al., 2009). The other parameters can be computed using existing numerical forecasting methods (Ahmad and Tiwari, 2011; Badescu, 2002; Barbaro et al., 1986; Kasten and Czeplak, 1980).

Several models however, do correlate cloudiness to solar irradiance. The earlier models take into consideration only the effect of the cloud coverage (in oktas) to the total solar irradiance (Ahmad and Tiwari, 2011), whereas more recent models take into account the cloud type, the location of the cloud in relation to the sun's position, resulting to the obscuring of the sun and the subsequent reduction in Direct Normal Irradiance (DNI), and the total cloud coverage that affects diffuse irradiance (Hammer et al., 2003). The influence of clouds on solar irradiance is due to reflection, absorption and scattering of the irradiance by cloud particles and depends strongly on the volume, shape, thickness and composition of the clouds (Badescu, 1999; Bakirci, 2009; Deneke et al., 2008; Kokhanovsky, 2004; Ododo et al., 1996; Orsini et al., 2002).

Furthermore, the detection and classification of clouds and estimation of the cloud height are essential for the numerical weather prediction models and the computation of cloud motion winds (Menzel, 2001; Orun et al., 2000; Szantai et al., 2002) and for precipitation estimation (Hong et al., 2004; Manoj et al., 2010).

Until the end of the last century, the determination of cloud coverage was prepared by human observers, yet the increased need for accuracy and world-wide measurements prompted research for computer based algorithms that would distinguish the clouds in the sky and give information about their class and physical properties (Goodman and Henderson-Sellers, 1988; Key et al., 1989; Ruprecht, 1985).

Numerous researchers proposed several methods for cloud classification, employing different instruments for their measurements and different techniques for the classification of the clouds, as will be analyzed in the next chapters of the paper. The measuring instruments may be: (1) ground based, (2) integrated on satellites or (3) positioned on meteorological balloons. The classifiers (programs/software based algorithms for measuring/calculating/evaluating the cloud class) range from simple ones using threshold or rule-based techniques to more complicated ones, consisting of supervised neural networks methods using numerous features and huge libraries as a training set.

The aim of the present paper is to provide a detailed review on the different techniques and equipment used for automatic cloud classification and provide a table of the experimental results of the published research in the field. The review initiates with a brief introduction to clouds and their effect on incident solar irradiance on the earth's surface. The third chapter consists of a detailed description of the equipment used for the measurements; ground based, satellite integrated or meteorological balloon based. Finally in the fourth chapter, an analysis of the existing algorithms for automatic cloud classification, including a presentation of a table of the up-to-date experimental results, is provided.

2. Cloud types and classification

However, not all clouds have the same effect on irradiance. There are different types of clouds with different dimensions, opacity and properties depending on several parameters, resulting to a different effect on solar irradiance. Moreover, a single cloud has a different effect on solar irradiance compared to multiple clouds or overcast skies, since the reduction of the irradiance depends on whether the cloud obscures the sun or not and on the cloud coverage. The presence of a cloud in the sky in relation to the sun's position, may result in the obscuring of the sun and a reduction in DNI. In contrast, during cloudy conditions diffuse irradiance is enhanced due to the reflection of

solar irradiance from the base of the clouds and from the scattering of direct irradiance due to cloud particles. Furthermore, diffuse irradiance in overcast skies has on average higher value compared with skies with few clouds. Consequently, during cloudy conditions global irradiance is reduced, even though, sometimes, the presence of clouds results to short-term enhancement of global irradiance (Duchon and O'Malley, 1999; Kasten and Czeplak, 1980; Orsini et al., 2002) even to extreme values of over 140% of the estimated value from clear sky models (Emck and Richter, 2008; Piacentini et al., 2011).

In this chapter, we analyze the different cloud types based on the World Meteorological Organization (WMO) classification (WMO, 1956, website) and the estimation of solar irradiance for cloudy sky conditions.

A cloud is an aggregate of minute, suspended particles of water, ice, or both, that are in sufficient concentrations to be visible; a collection of 'hydrometeors', a term that also includes in some cases, due to the distance of the observer, the precipitation particles that fall from them. Today, the term 'cloud' also includes those clouds that are nearly invisible to the human eye, but are readily detectable in satellite thermal imagery (WMO, 1956, website).

Clouds are classified using a Latin "Linnean" system based on genera and species, originally developed by Howard (1803), an amateur meteorologist in 1802 (Rogers and Yau, 1989). The modern classification scheme which is used up to date is based on Howard's system and is detailed in "The International Cloud Atlas" (WMO, 1956). For former classifications, Getzelman (1989) presented a literature review based on the way artists painted the sky.

Clouds are generally defined according to the phases of water present and the temperature of the top part of the cloud (cloud top) (American Meteorological Society, website) and are classified based on: (1) the genera, that is the main characteristic form of a cloud, (2) the species, that depend on the peculiarities in shape and differences in the internal structure of a cloud, (3) the varieties, that define the special characteristics of the arrangement and transparency of a cloud, (4) the supplementary features and accessory clouds, where minor cloud forms are attached to the main part of the cloud and (5) the mother cloud, that defines the origin of a cloud, in the cases where the cloud was formed from another cloud (Ahrens, 2009; Cotton et al., 2011; Glickman, 2000; Vasquez, 1989).

Table 1
Classification of clouds based on their altitude for different polar regions (Ahrens, 2009, NOAA – National Weather Service, website).

Level	Polar region	Temperate region	Tropical region
High clouds	3–8 km	5–13 km	6–18 km
Middle clouds	2–4 km	2–7 km	2–8 km
Low clouds	Surface-2 km	Surface-2 km	Surface-2 km

In addition to the standardized genus-species system, the WMO also classifies clouds by altitude and divides the troposphere vertically into three levels; low, middle, and high. Each level is defined by a range of vertical heights at which each type of cloud typically appears, although the height of the clouds depends on the polar region of the observation as shown in Table 1 (NOAA, website).

The clouds are divided in ten types as follows (Ahrens, 2009; Cotton et al., 2011, NOAA – National Weather Service, website), Rogers and Yau, 1989; WMO, 1956):

- *High level clouds*: **Cirrus (Ci)**, **Cirrocumulus (Cc)** and **Cirrostratus (Cs)**. They are typically thin and white in appearance, but can appear in a magnificent array of colors when the sun is low on the horizon.
- *Mid-level clouds*: **Altocumulus (Ac)**, **Altostratus (As)**, and **Nimbostratus (Ns)**. They are composed primarily of water droplets; however, they can also be composed of ice crystals when temperatures are low enough.
- *Low level clouds*: **Cumulus (Cu)**, **Stratocumulus (Sc)**, **Stratus (St)**, and **Cumulonimbus (Cb).** They are composed of water droplets.

Fig. 1 (Cloud Appreciation Society, website) presents a visual representation of the ten main cloud types.

In addition to the type division, clouds can further be classified in species, and sometimes divided further into varieties, which define the special characteristics of the clouds, and are related to the cloud transparency and the arrangements of the macroscopic cloud elements. Table 2 (WMO, 1956) presents the most common species and varieties per cloud type.

Apart from the ten types of clouds, one should also consider fog and contrails. Even though they have similar characteristics as clouds, they have a different origin.

Fog occurs frequently around bodies of water close to the earth's surface and other places where cool air mixes with warmer air and vice versa. It is formed from water droplets suspended in the atmosphere and reduces visibility at the earth's surface (Ahrens, 2009; Cotton et al., 2011).

Contrails or vapor trails are artificial clouds that are artificially generated by the condensation of water vapor from the exhaust of aircraft engines. The exhaust gases are very hot, and when they come in contact with the cold surrounding air, they may precipitate into a cloud of microscopic water droplets. If the air is cold enough, this trail will comprise of tiny ice crystals. The formation of the contrails depends on the level of moisture in the atmosphere and the altitude that the plane is flying at. Contrails are the artificial counterparts of cirrus clouds, since they are high level clouds of the same form. Like cirrus clouds, contrails reflect solar radiation and absorb and emit thermal infrared radiation causing cloud radiative forcing depending on many factors, such as optical depth and coverage of the contrail. They may affect local climatic conditions, as they can persist for many hours if the relative

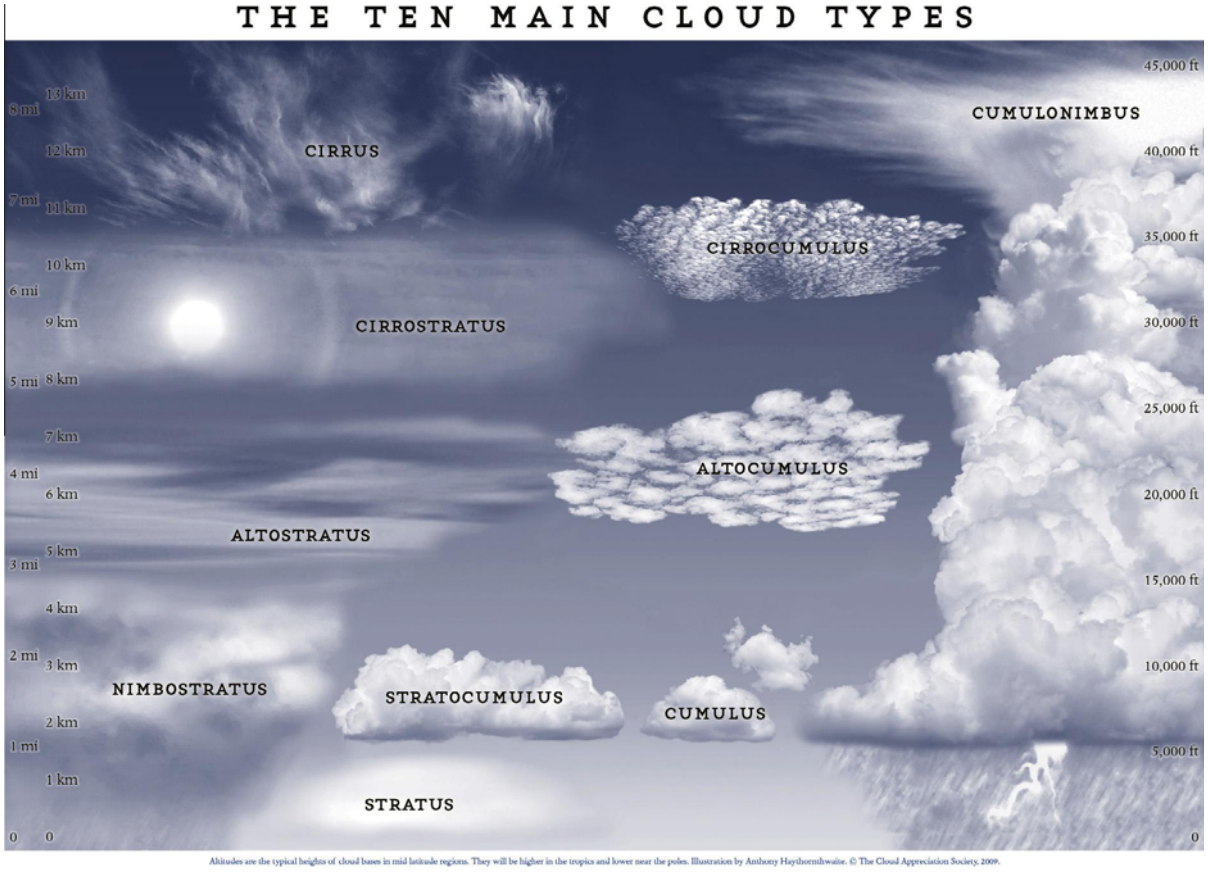

Fig. 1. The 10 main cloud types (Cloud Appreciation Society, website).

humidity of the surrounding air is high (Ahrens, 2009; Cotton et al., 2011; Degrand et al., 2000; Minnis et al., 2004).

An alternative classification of clouds takes into account their particulate composition. Water clouds are composed entirely of water droplets (ordinary and/or supercooled), ice-crystal clouds are composed entirely of ice crystals, and mixed clouds are a combination of the first two. The particulate composition of clouds depends on their height level. Within the high cloud family, cirrostratus and cirrus are always ice-crystal clouds, while cirrocumulus may be mixed. Mid-level clouds can either be mixed or water clouds. Low-level clouds are usually water ones and occasionally mixed, except from cumulonimbus, that is always mixed (Cotton et al., 2011).

The appropriate classification of clouds is the basic prerequisite for predicting their motion and the incident solar radiation that passes through them for different reasons, such as:

- Different types of clouds decrease, at a different proportion, the incident solar radiation that passes through them.
- There is a direct correlation of the incident solar radiation with the dimensions and opacity of the cloud.
- Ice crystals and water drops have a different impact at the absorption and scattering of incident solar radiation.
- Due to different altitudes at which different types of clouds are located, the clouds may be affected by different air flows thereby moving in different directions at different speeds.
- Furthermore, due to the dissimilar weather conditions due to difference in altitude, clouds may have a divergent development over time; with some of them leading to rain.

Thus, with knowledge of cloud type, size, motion and development, one can calculate and predict the solar radiation reaching a solar RES site and calculate the energy production of the given site.

3. Measuring equipment for cloud classification

In this chapter, the numerous measuring instruments used for obtaining the necessary data for cloud classification are presented. Ground equipment is mainly used to measure data for a specific location, whereas satellites are used for measuring data over continents. Ground equipment has a small field of view, limiting the ability of monitoring the formation of clouds and their movement over a large sky area. Nevertheless, since the state of the sky is measured on-site, they provide a very sufficient accuracy for the local variations of solar irradiance due to clouds.

Table 2
The 10 cloud types and their most common species and varieties. The letters in parentheses denote accepted abbreviations (World Meteorological Organization, 1956).

Genera	Species	Varieties
Cirrus (Ci)	uncinus, fibratus, spissatus, castellanus	intortus, radiatus, vertebratus
Cirrostratus (Cs)	nebulosus, fibratus	–
Cirrocumulus (Cc)	castellanus, floccus, lenticularis	undulatus
Altocumulus (Ac)	castellanus, floccus, lenticularis	translucidus, opacus, undulatus, perlucidus
Altostratus (As)	–	translucidus, opacus
Nimbostratus (Ns)	–	–
Stratocumulus (Sc)	castellanus, lenticularis	perlucidus, translucidus opacus
Stratus (St)	fractus, nebulosus	–
Cumulonimbus (Cb)	calvus, capillatus,	–
Cumulus (Cu)	fractus, humilis, mediocris, congestus	–

On the other hand, satellites provide large-scale cloud information and multispectral measurements from different sensors, but the provided data is in low resolution and may contain errors; small clouds are often overlooked due to the limited analysis and low or thin clouds are frequently not distinct from land (Dybbroe et al., 2005a, 2005b; Heinle et al., 2010, Ricciardelli et al., 2008). The cost of the equipment is an important factor for cloud measurements, since the usage of satellites is much more expensive than most ground instruments. Yet, some specialized ground meteorological observing systems such as RADARs may be equally expensive as the satellites (Clothiaux et al., 1998; Seiz et al., 2002; Wang and Sassen, 2004).

3.1. Ground equipment

Ground equipment is used to detect clouds on the sky at a specific location, although it may be integrated onto a moving vehicle (Heinle et al., 2010). The ground equipment can be divided in three groups. The first group includes the irradiance meters that measure global diffuse and direct irradiance and radiometers that measure the incident electromagnetic radiation of a specific spectrum at the specified location. The second group includes sky spectral cameras that photograph the state of the sky in the visible (VIS), infrared (IR) or ultraviolet (UV) spectrum while the third group includes radars that measure the backscattered electromagnetic signal of the instrument.

3.1.1. Irradiance meters–radiometers

The first category of equipment includes those equipment that measure the radiation received on site; pyranometer, pyrheliometer, pyrradiometer, photometer, IR pyrometers and radiometers. The concept of using these instruments is based in the fact that all objects having a temperature above absolute zero radiate electromagnetic radiation due to their molecular oscillations. As the temperature of an object increases, these oscillations become more intense and the emitted radiation increases and peaks at gradually shorter wavelengths. This results to the fact that everything in nature has a distinct spectral signature of reflected, emitted and absorbed radiation. This signature allows the distinction of different objects, such as sun, clouds, sky molecules, land, sea, ice and buildings. The measurement of the electromagnetic radiation within the VIS, IR and UV spectrum is called radiometry and the measuring instruments are called radiometers, although each instrument has a different name according to the measuring spectrum, such as IR radiometers, UV radiometers and MicroWave Radiometers (MWRs). (Borengasser et al., 2008). Furthermore, Spectroradiometers are automated radiometer systems that scan at a pre-specified spectral range, at predefined scanning steps allowing measurements at multiple wavelengths using only one instrument. Depending on their spectral range, they are named IR specroradiometers, UV spectroradiometers, spectrophotometers for visible light, etc. (Estupiñán et al., 1996; Kim et al., 2006; Vasaras et al., 2001; Winiecki and Frederick, 2005).

A pyranometer is an instrument for measuring the total global shortwave radiation (300–3000 nm), while a pyrheliometer is used for measuring the DNI (200–4000 nm) (ISO 9060:1990; WMO, 2008). A pyrradiometer is used for measuring the net total downward radiation flux (solar, terrestrial, and atmospheric) at the range of 300–60,000 nm (Orsini et al., 2002). In general, these instruments produce an electrical signal proportional to the solar irradiance (Lester and Myers, 2006). Irradiance meters measure the broadband solar radiation in order to estimate the daytime surface energy budget, i.e. the energy balance between incoming energy from the Sun and outgoing thermal (longwave) and reflected (shortwave) energy emitted from the earth. Solar irradiance during a day can be estimated computationally, using clear sky models for every location without of course taking into account the effect of clouds and irradiance measurements naturally integrate the effects of clouds on the intensity of solar irradiance (Dupont et al., 2008; Martínez-Chico et al., 2011). Experimentally, to measure the effect of clouds, the instruments provide a measurement of the incident solar irradiance, indicating the effect of intervening clouds along the solar beam path from the sun to the sensor, thus providing a time series of global irradiance variations due to clouds (Boers et al., 2000; Calbó et al., 2001), as will be explained in Section 4.1.7. The concept of using irradiance measurements to estimate cloud types is based on the fact that clouds with different

velocities and optical depth cross the slow changing path of the solar beam over different time durations (Duchon and O'Malley, 1999). However due to the earth's motion about the sun, relevant cloud velocity depends on zenith angle, high clouds seem to move slower than low clouds. This causes a problem, since when high clouds are located at large zenith angles, in some rare cases, the cloud speed is such that the cloud is always in the solar beam path between the sun and the sensor resulting to measurements indicating an overcast sky. The same wrong estimation can occur for every cloud moving at such a speed that it blocks constantly the solar beam from reaching the sensor (Duchon and O'Malley, 1999; Pagès et al., 2003).

A pyrometer is a passive instrument that measures emitted thermal radiation from the surface of an object. The working principle of the pyrometer is based on the Stefan–Boltzmann law that correlates the thermal radiation of an object to the object's temperature and emissivity. IR pyrometers detect the blackbody radiation of an object, which is a portion of the thermal emission of the object (Feister et al., 2010; Gillotay et al., 2001).

The sun photometer (or sun radiometer) is a photometer that is turned towards the sun measuring the intensity of direct sunlight. Photometers measure the light intensity of surfaces or fluids by measuring the incident light on their photo-sensitive detector. There are many variations of sun photometers that use different filters for measuring one or more spectral bands, stationary or portable, with tracker or without moving parts. As an example regarding cloud detection, a sun photometer in the IR 940 nm band (IR/WV) measures the amount of Water Vapor (WV) contained in a column over a given area that is often defined as the "Column water vapor amount". The IR 940 nm band corresponds to a strong WV absorption band; consequently, the amount of WV within the measurement path can be derived from the instrument's observations (Calbó et al., 2008; Cazorla et al., 2008a; Halthore et al., 1997; Michalsky et al., 2001).

The final instrument in the "radiation sensors" category is the UV radiometer that measures the incident UV radiation on earth (Mayer et al., 1998; Parisi and Downs, 2004; Sabburg and Calbó, 2009). Solar radiation is part of the electromagnetic spectrum emitted by the sun, and thus, using the same principle as with the irradiance meters, any differences in UV irradiance compared to clear sky conditions are considered to occur due to the presence of clouds (Mckenzie et al., 1998; Villán et al., 2010). There are several commercial UV radiometer models, either measuring UV total irradiance (280–400 nm) or only parts of it: UV-A (320-400 nm) or UV-B by producing an electrical signal proportional to solar irradiance. Finally, the dosimeter is a device that responds directly when exposed to UV radiation, usually based on chemical reactions (Wauben, 2006).

3.1.1.1. Commercial irradiance meters. The Infrared Pyrometer CIR-7 (known as Nephelo) is a ground-based instrument designed and assembled by ATMOS Sarl in France for day and night cloud cover imaging. It comprises of 7 IR pyrometers in the spectral range of 9000–14,000 nm, each with a 12° field of view. The sensors are mounted at zenithal angles 0, 12, 24, 36, 48, 60 and 72 on a semicircular azimuthally tracker. To obtain an all-sky view, the turret will have to make 30 rotational steps by 12° each. The total time of each scan is 203 s which is a very long period compared to other methods but it guarantees a good mechanical stabilization of the instrument and that the measurements are performed in the right direction. Moreover, if clouds are moving quickly, then a line often appears in the middle of the scan due to the rotation of the instrument. In the case of even faster clouds, some circular shape may be observed in one or more frames (Berger et al., 2005; Gillotay et al., 2001). CIR-4 and CIR-13 are different versions of CIR-7, based on the same principles, consisting of 4 and 13 IR sensors respectively (Collet et al., 2009).

The Nubiscope is an instrument that consists of an IR pyrometer that receives IR radiation emitted from the atmosphere in the spectral region of 8000–14,000 nm with a full viewing angle of 3°. A tracker directs the tube containing the pyrometer at 30 different zenith angles in steps of 3° between the zenith and the horizon, and at 36 azimuth steps of 10° each (Boers et al., 2010). It takes about 6 min to perform one spatial sky scan that consists of 1080 individual spot measurements. The instrument is integrated with a computer algorithm that processes the data. The said algorithm provides the cloud fraction of the sky for three different levels of the sky in order to classify low, medium and high clouds. Moreover the algorithm calculates the Cloud Base Height (CBH) and a rough cloud description such as clear sky, overcast, broken clouds, cirrus and fog. A further development of the instrument provides even more types of clouds such as transparent clouds, low transparent clouds and heavy precipitation (Feister et al., 2010; Wauben, 2006) as will be presented in Section 4.

The Multi-Filter-Rotating Shadowband Radiometer (MFRSR) is a sun photometer that collects sky radiation through a horizontal diffuser and uses a rotating shadow band to separately measure the global and diffuse components of the radiative field; the direct component is derived as the difference between the two measurements (Harrison et al., 1994; Michalsky et al., 2001). The commercial model MFR-7 has a channel for the total shortwave radiation (300–3000 nm), and six more spectral channels. It uses the IR/WV – 940 nm band to detect the column water vapor amount (Kassianov et al., 2011a, 2011b). The same principles with the MFRSR apply to the Rotating Shadowband Spectroradiometer (RSS) but in the spectral range of 360–1050 nm (Kiedron et al., 2006). Min et al. (2008) proposed a simple method for narrow multispectral measurements from instruments like MFRSR or RSS, for monitoring fractional sky cover in large geographic distribution. Their method is based on the transmittance ratio

of clouds at selected wavelengths and has an accuracy of more than 90%.

3.1.2. Sky spectrum cameras

Another category of equipment is the sky spectrum cameras, that photograph the state of the sky in the Visible, IR or UV spectrum. Visible spectrum cameras detect and classify clouds based on the differences in the color and intensity between the different cloud types and sky (or land). IR cameras' classification scheme is based on the difference in the reflected and thermal IR radiation from the different types of clouds and sky (or land), subject to the measured Brightness Temperature (T_b). Brightness temperature is a descriptive measure of radiation in terms of the temperature of a hypothetical blackbody emitting an identical amount of radiation at the same wavelength. The brightness temperature is obtained by applying the inverse of the Planck function to the measured radiation (Glickman, 2000). Finally, UV cameras' classification scheme is based on the different absorption of the UV radiation of the different classes of clouds and by correlating the reduction or enhancement of measured UV irradiance due to the presence of clouds. A thorough analysis of the cloud detection and classification schemes/algorithms will be analyzed in Section 4.

A ground based camera/all sky camera is a ground based camera, which captures pictures of the whole sky (Chow et al., 2011; Kassianov et al., 2005; Martínez-Chico et al., 2011), or part of the sky (Janeiro et al., 2010; Richards and Sullivan, 1992; Singh and Glennen, 2005; Souza-Echer et al., 2006) at scheduled time intervals. An all sky camera is an automated color imaging system for sky observations and estimation of the cloud coverage that covers a 180° view (Bajwa and Hyder, 2005; Chow et al., 2011). A typical all sky camera has two major components. The first component is a weather proof box with the optical assembly and the second is the computer control assembly (Pfister et al., 2003). At the heart of the optical assembly is a color charge-coupled device (CCD) or Complementary Metal Oxide Semiconductor (CMOS) camera, pointing upwards to mirror the whole sky (Partamies, 2004; Syrjäsuo, 1996), although some versions of all sky camera use monochromatic sensors (Kegelmeyer, 1994). A typical arrangement of an all-sky camera consists of the camera, a fisheye lens positioned on top the camera and a hemispherical glass optical dome for environmental protection and neutral density or spectral filters can be used to block the sun's intense direct-normal radiation. An alternative arrangement of the all sky camera consists of the camera pointing downwards to a hemispherical mirror that images the sky image into the lens. Additional features include a heated glass and an optional solar tracking occulator used to hide the sun spot, to prevent camera blooming and the production of artifacts in the image (Berger et al., 2005; Long et al., 2006; Slater et al., 2001). Furthermore, some commercial models include an image processing algorithm running on a computer workstation that captures images at user-defined intervals and saves them for analysis. Most of the algorithms processing data from sky cameras use a "color ratio threshold" to distinguish whether a pixel represents a clear or cloudy portion of the sky image (Calbó and Sabburg, 2008; Cazorla et al., 2008a, 2008b), as it will be explained in Section 4.1.1. The major disadvantage of ground-based sky cameras is that they have systematic detection errors such as misdetection of thin clouds and limitations in distinguishing cloud types (Calbó et al., 2008). Fig. 2 presents the image acquired from an all sky camera for four different conditions of the sky (Martínez-Chico et al., 2011).

A UV camera measures the near UV spectrum of solar irradiance (380–200 nm). A UV camera consists of more or less similar equipment as the Ground based camera but with a UV pass filter in front of the digital camera. Thus the image acquired is only due to the light in the UV spectrum (Calbó et al., 2008; Long et al., 2006; Sabburg and Wong, 1999).

Similarly, an Infrared (IR) camera has an IR pass filter (7500–14,000 nm) blocking the visible spectrum from the image and a microbolometer sensor that detects IR radiation at 7500–14,000 nm (Anzalone et al., 2009; Brocard et al., 2009, 2011; Smith and Toumi, 2008).

3.1.2.1. Commercial sky spectrum cameras. The Infrared Cloud Imager (ICI) is comprised by an IR camera, one or two blackbody calibration sources, a gold-plated beam-steering mirror, and control electronics. The ICI system records radiometrically calibrated images of the sky in the thermal IR window band of 8000–14,000 nm at a field of view of approximately 18° × 13.5° (Smith and Toumi, 2008). The display of the camera on the screen is color coded according to the brightness temperature of the black body. Within the ICI optical bandwidth, the most highly variable emission source other than clouds is WV, that has to be removed from the ICI images in order to obtain the residual radiance that is used to identify clouds (Rogalski and Chrzanowski, 2002; Shaw et al., 2002; Shaw and Thurairajah, 2005).

A similar instrument to the ICI was developed by Maghrabi et al. (2009), specifically designed for cloud detection. The detector has a 3° or 90° field of view, depending on the application and spectral range.

The VIS/IR Whole Sky Imager (WSI) is a passive automated digital imaging system distribution manufactured at the University of California San Diego, that obtains both visual and Near IR (NIR) images of the sky at a 180° view under both day and night conditions, in order to assess cloud fraction, cloud morphology, and radiance (Feister et al., 2010; Slater et al., 2001). It is a modification of the all sky camera, consisting of additional spectrum and neutral density filters on a mechanical filter changer. It has seven different spectral bands in the visible and NIR region providing many variations in the spectral range of the camera using different spectral filters (Allmen and Kegelmeyer, 1996; Johnson et al., 1989; Shields et al., 1998). Similar to

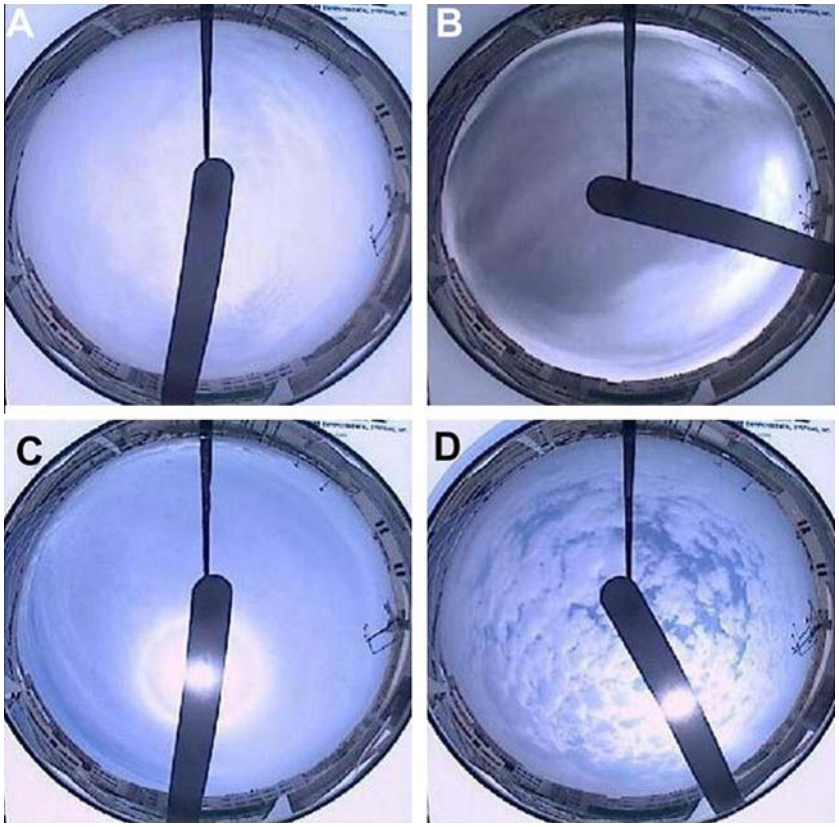

Fig. 2. The image acquired from an all sky camera for four different conditions of the sky based on beam transmittance index k_b of the sky, calculated as the ratio of DNI to the extraterrestrial radiation (computed from the earth–sun distance). Fig. 3A: $k_b < 0.2$, As with a uniform and homogenous base, Fig. 3B: $k_b < 0.2$, Ns, characterized by a dark gray base, Fig. 3C: $0.2 < k_b < 0.4$, Cs that covers large areas, Fig. 3D: $0.2 < k_b < 0.4$, Ac with a cottony appearance. (Martínez-Chico et al., 2011).

the all sky camera, WSI consists of a weather proof box covering the optical assembly and the computer control assembly. The core of the optical assembly consists of the camera sensor whose focal plane is cooled to reduce electronic noise. On top of the camera sensor is an optical stack that consists of spectral and neutral density filters, a mechanical shutter, a fisheye lens, and a glass dome protection from environmental conditions (Black and Tooman, 2005; Tooman, 2003). An occulator is positioned between the dome and the sun (or the moon) to prevent direct sunlight/moonlight from producing artifacts in the image (Buch et al., 1995; Seiz et al., 2007). The incorporated algorithm compares, pixel-by-pixel, each acquired image to a matching clear sky image (Calbó and Sabburg, 2008), acquired from a library of background images that cover the full range of solar zenith angles. If the image pixel varies from the matching clear sky pixel, then the pixel is identified as a cloud (Rodriguez, 1998).

The Solmirus All Sky Infrared Visible Analyzer (ASIVA) is another hybrid camera used for cloud detection and classification that provides measurements from two cameras, one in the VIS and the other in the IR (8000–1300 nm). The VIS camera consists of a CCD or CMOS sensor and a 180° fish eye lens. The IR camera consists of a microbolometer IR sensor, a filter wheel, a blackbody calibration source and a 180° fish eye diamond coated lens (Morris and Klebe, 2010; Sebag et al., 2008).

Finally, the Whole-sky Infra Red Cloud-Measuring System (WSIRCMS) which was proposed by Liu et al. (2011) is an IR camera in the range of 8000–1400 nm that uses an azimuthal tracker to obtain IR images of the sky at nine different positions in order to achieve a whole sky image.

3.1.3. Active remote sensing instruments

Active remote sensor instruments have active sensors that transmit energy in a specific short wavelength and compare the characteristics of the transmitted and the received back energy and based on the timing of the two pulses, the angle and the wavelength, results can be deduced depending on the application (Campbell and Wynne, 2011).

Cloud detection radars are radiometers that emit an electromagnetic signal toward the sky and detect the backscattered signal. The time difference between emission and reception of the signal and the reduction in strength of the signal determines the location of the clouds, the CBH and the vertical height of the clouds (Kato et al., 2001; Feister et al., 2010). Most radars used for cloud detection use the MW band, so they are called MilliMeter Wave Radars (MMWRs) or MilliMeter wave Cloud Radars (MMCRs).

MMWRs provide radar reflectivity and mean Doppler velocity profiles for most of the cloud types in the troposphere. Most MMWRs use the 35 GHz (Ka band) or 94 GHz (W band) wavelengths in order to detect clouds in the sky and determine cloud's top and base height. Furthermore, they detect snowfall drizzle, and very light rain. The height coverage is up to 20 km with a spatial resolution lower than 45 m, although, since they detect cloud particles in the millimeter range, during precipitation conditions, the height coverage is decreased (Kollias et al., 2007; Wang and Sassen, 2001).

An example of an MMWR in the ka band is the MIRA-35 model that measures atmospheric backscattered signals of electromagnetic waves sent out by the instrument in the 35.5 GHz (8 mm) band. The height range that can be measured by the instrument is 0.25–14 km with a resolution of 30 m. MIRA-35 measures reflectivity, Doppler velocity and its variation, and linear depolarization ratios. The main cloud's parameters that may be derived from the method in combination with measurements from other instruments are: CBH, cloud-top heights, droplet size distribution and the ice/water content of the clouds (Feister et al., 2010; Martner et al., 2002). Respectively, an example of an MMWR in the W band is the MRL-5. MRL-5 has two channels in the 3 cm and 10 cm wavelength band (Clothiaux et al., 1995; Randriamampianina et al., 2000).

Light Detection And Ranging (LIDAR) is based on the application of lasers that are composed of monochromatic light. In contrast to other colored light sources that emit over a broad spectrum of wavelengths, laser light is composed of a narrow range of wavelengths (monochromatic) and can be considered very pure light source. The advantage of the monochromatic light is that it can be transmitted over large distances with very small diversion, providing very accurate measurements. Depending on the application, LIDARs can transmit up to 300,000 pulses per second mostly using wavelengths within the visible spectrum depending from the application. As an example the 0.532 μm green is used for penetration of water bodies (Campbell and Wynne, 2011). The backscattered light consists of the elastic components where the wavelength and frequency is the same to the emitted light (Rayleigh scattering) and the inelastic components where a difference in frequency takes place (Raman scattering). Based on the working principle of the instrument, the elastic or inelastic components of the backscattered signal is measured and analyzed.

The Micropulse (MPL) LIDAR is a zenith-pointing optical remote sensing system, designed primarily to detect clouds in the sky and calculate their altitude (Clothiaux et al., 1998; Poyer, 2008). The operating principle is based on the transmission of laser pulses (523.5 nm or 532 nm) and the measurement of the elastic backscattered signal of a vertical resolution of 30–300 m, up to about 20 km. The backscatter profile provides information on the amount of particles that cause the backscatter, as a function of height (Dupont et al., 2008). Due to the high sensibility of the system and the very narrow field of view (0.006°), it can detect even the slightest amount of clouds in the sky. Cloud detection is based on the average value of the backscatter profile over a period of 1 min to estimate the lowest height of the clouds (Mendoza and Flynn, 2006; Rodriguez, 1998).

Raman LIDAR isolates and measures the inelastic components of the backscattered light. The working principle is based on the Raman scattering of the WV, nitrogen and oxygen which have unique energy shifts so they can be detected by separate channels of the instrument, using narrowband interference filters. Raman LIDARs provide water vapor profile, temperature profile, cloud properties including backscattering coefficients and LIDAR linear depolarization ratio temperature (Newson, 2009; Turner and Goldsmith, 1999).

Ceilometers are active instruments that are used to indicate the base height of one (or more) layer of clouds (Emeis et al., 2004). Laser Ceilometers are ground-based instruments that make use of the elastic LIDAR principle by emitting signals vertically in the atmosphere up to 15 km and measuring the backscatter profile of these emissions from clouds and precipitation with a receiver telescope (Ahrens, 2009; Boers et al., 2010; de Haij et al., 2006; Martucci et al., 2010; Rodriguez, 1998; Poyer, 2008). Optical ceilometers use triangulation to determine the CBH (Feister et al., 2010) and they can locate the CBH of the lower three clouds in one pulse (Nowak et al., 2008).

Rotating beam ceilometers consist of a transmitter that transmits light beams upwards and a rotating receiver positioned at a known distance from the transmitter. The receiver is rotating at multiple angles (typically from 8° to 85°) and detects the backscatter light from the base of the cloud. The receiver consist of a photoelectric cell positioned at a controlled angle of view, vertically to the emitted signal to ensure that only light that is scattered from the cloud is detected by the receiver. The angle of the detected cloud and the distance between the receiver and transmitter defines the height of the cloud (WMO, 2008).

3.1.4. Integration of multiple ground based instruments

The Southern Great Plains (SGP) Cloud And Radiation Testbed (CART) site in Oklahoma USA provides ground-based integrated observations of the sky consisting of several different instruments such as multispectral Radars, Raman LIDAR, MPL LIDAR, multifilter radiometers and radiometers at specific spectral bands, a RSS, all sky camera and thermometers among others. The cloud classification is achieved by using vertical and horizontal cloud properties, the presence, or absence of precipitation, liquid water path, and downward IR Brightness Temperature (T_b) (Wang and Sassen, 2001, 2004).

Cloudnet is a European research project of three collaborating countries (UK, France and Netherlands) aiming to optimize the existing data sets from three weather stations and develop cloud remote sensing algorithms. The main instruments used by Cloudnet are Doppler cloud radar,

LIDAR ceilometers, multispectral radiometers, and multispectral Radars (Illingworth et al., 2007).

3.1.5. Radiosondes

The last type of equipment used for cloud monitoring/detection is the radiosonde, a device of various electronic instruments integrated under a weather balloon. A weather balloon is filled with hydrogen or helium in order to rise at an altitude of more than 30 km at a speed of approximately 5 m/s. The radiosonde package comprises of various sensors which measure temperature, air pressure and relative humidity with respect to height. During the upwards elevation of the balloon, radiosonde detects clouds giving information about the cloud base height, thickness and top height of the clouds. A major advantage of radiosondes is that they can detect multilayer clouds at every level of the atmosphere (Chernykh and Eskridge, 1996; Clarke and Korff, 1941; Zhang et al., 2010). The measurements are transmitted instantaneous to a fixed receiver. Furthermore, the horizontal displacement of the balloon is an indication of the wind speed and direction at any given layers of the atmosphere. During the last few years, a Global Positioning System (GPS) was also integrated in the radiosonde package in order to track the exact displacement of the balloon (Ahrens, 2009).

3.2. Satellite equipment

There are numerous satellites orbiting earth which serve different purposes and in this chapter we present the satellites used for meteorological purposes. Some are geostationary, circle the earth in a geosynchronous orbit, scanning always the same area, while others are polar orbiting, passing over both poles of the earth during each orbit, or have a sun synchronous orbit, passing over the same location at the same time every day. Apart from these orbits that can be used for meteorological reasons, there are many other different orbits, serving different purposes, such as non-sun-synchronous orbits where the satellite does maintain a polar orbit, but does not synchronize latitude passes with a specific time.

Weather satellites are satellites that have as primary function the observation of the weather on earth. They have on-board a "multi-radiometer" instrument, called "an imager", that incorporates all necessary equipment for measuring passive or active VIS, reflected IR, thermal IR, UV and MW, among other measurements. For obtaining these measurements, imagers have several radiometric channels, using a different sensor for each channel in order to measure data at a specific wavelength range (Weng, 2011). The improvements in remote sensing technology leads to the development of better imagers, with more spectral channels and higher resolution and sensitivity, thus, newer versions of satellites consisting of new generation imagers enables the handling of a greater range of data, acquired from more types of satellite images. A comparison of the different imagers was presented by Tsuchiya and Tokuno (1992) and by Li et al. (2007). Data from the VIS band is basically a photograph of a specific area of the earth, that captures the reflected sunlight from the upper surface of the clouds. Thick clouds appear brighter in the photographs because they have higher reflectivity than thin clouds. On the other hand, IR and UV channels are used to measure the emitted and absorbed IR or UV radiation from the same area of the earth. The VIS channel data is normalized by the cosine of the solar zenith angle in order to eliminate the seasonal variability of the pixels of the picture due to the time, location and the relevant position of the sun and the pixels of the image (Loyola et al., 2010). A detailed analysis of the satellite imagers' channels and how they are used in cloud classification will follow in the next chapters.

3.2.1. Geostationary satellites

The Geostationary Operational Environmental Satellite (GOES-#) series, where # denotes the series number (NOAA – Office of satellite operations, website, 2011), circle the earth in a geosynchronous orbit, which means that they orbit the equatorial plane of the earth at a speed matching the earth's rotation and at such height to allow for a full-disc view of the earth (Jedlovec and Haines, 2008). Synchronous Meteorological Satellites (SMSs) is the name for the first three GOES satellites (Parikh, 1978; Parikh and Ball, 1980). Since they are located always over the same area, they provide a constant view of that area, so the landmark's spectral signature is unchangeable and is used as a background for the calculations (Azimi-Sadjadi and Zekavat, 2000; Bankert and Wade, 2007). The GOES # satellites have on board the GOES I-M Imager, a five channel (one visible, four IR) imaging radiometer measuring at a wavelength range from 650 nm to 12,000 nm (Bankert and Wade, 2007; Tian et al., 1999), while a two axis servo motor driving the scanning mirror of the imager scans an area of 3000 km by 3000 km in just 41 s. The sensor unit containing the telescope, scan assembly and the imaging radiometers is mounted outside the main structure of the spacecraft (NOAA – Office of satellite operations, website, 2011), Tian et al., 2000; Saitwal, 2006).

The Meteosat series of satellites are geostationary meteorological satellites (Ambroise et al., 2000; Christodoulou et al., 2001; Ghosh et al., 2006), operated by the European Organisation for the Exploitation of Meteorological Satellites (EUMETSAT) under the Meteosat Transition Programme (MTP) (Ameur et al., 2004; Campbell and Holmlund, 2004) and the Meteosat Second Generation (MSG) program (Bonomo and Brignoli, 1998; Casanova et al., 2010; Ricciardelli et al., 2010). The imager of the Meteosat satellite series is the Spinning Enhanced Visible and Infrared Imager (SEVIRI) instrument. SEVIRI is a line-by-line scanning radiometer, which provides image data in four Visible and Near-Infrared (NIR) channels and eight IR channels (Aminou, 2002; Schmid, 2000). A key feature of this imaging instrument is its continuous imaging of the earth with a baseline repeat cycle of

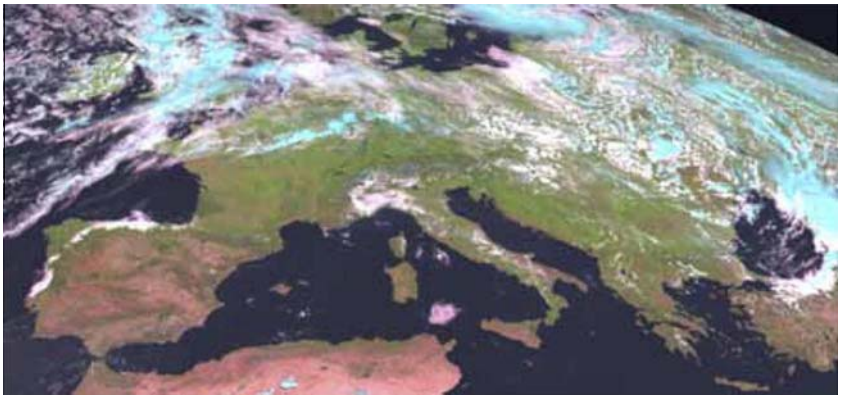

Fig. 3. An RGB image of European area, taken by SEVIRI channels at 0.635 μm, 0.81 μm and 1.64 μm, on June 2004 (Amato et al., 2008).

15 min (Amato et al., 2008; Christodoulou et al., 2003). Fig. 3 presents an RGB image of European area, taken by SEVIRI channels at 0.635 μm, 0.81 μm and 1.64 μm, on June 2004 (Amato et al., 2008).

Fengyun (FY-##) are China's weather satellites, where the satellites in the FY-1 and FY-3 series are in sun-synchronous orbits, while the satellites in the FY-2 series are in geosynchronous orbit (Jian and Jianmin, 2008; Li et al., 2008). The FY-2C which was launched in 2004 carries the Visible and Infrared Spin Scan Radiometer (VISSR) that was used in the SMS satellites, which has five channels in five different spectral bands measuring from 550 nm to 12,500 nm. VISSR consists of an optical telescope with a scan mirror, reflectors and lenses, together with the Visible and IR detectors and the radiation cooler. The VIS sensors are calibrated by viewing the sun from a reduced size side-looking prism system and the IR sensors are calibrated by detecting the black body radiation of the black body installed on the satellite. The cloud detection of the FY-2B satellite is based on a dynamic IR/VIS threshold. Brightness temperature difference between IR and IR/WV channel can be used to detect high cloud, while a spatial uniformity test can be used to detect broken cloud over the ocean. Furthermore, multi-day clear composite maps can be used to distinguish clouds from snow (Liu et al., 2009; Zhang et al., 2011). The cloud classification accuracy for the data taken from the FYs ranged from 81.4% (Zhang et al., 2011) to 94.26% (Li et al., 2008).

Kaplana-1 known as MetSat-1 is a geostationary meteorological satellite launched by Indian Space Research Organization on 2002. Kaplana's imager is the Very High Resolution Radiometer (VHRR) which has three channels: the VIS channel (550–750 nm), the IR channel (10,500–12,500 nm) and the IR/WV channel (5700–7100 nm) (Giri and Sharma, 2011).

Geostationary Meteorological Satellite (GMS-#) series, better known as Himawari, were geostationary weather satellites, operated by the Japan Meteorological Agency (Hamada et al., 2004; Liu et al., 1995; Shi et al., 2005). The successor series is called Multifunctional Transport Satellites (MTSAT-#) and consists of MTSAT-1 and MTSAT-2. MTSAT-2, known as Himawari-7, carries an imaging telescope of five channels: one visible (550–880 nm), 2 IR (10,300–12,500 nm), one IR/WV (6500–7000 nm) and one NIR (3500–4000 nm) (JAXA, website).

3.2.2. Sun-synchronous/polar orbiting/non-sun-synchronous satellites

The European Remote Sensing (ERS-#) satellite series, where # indicates the series number, consists of the identical European sun-synchronous satellites ERS-1 and ERS-2. ERS-1 stopped functioning in 2000 while ERS-2 was operational until September 2011. Among other instruments, ERS-2 had on-board the Active Microwave Instrument (AMI), the Along-Track Scanning Radiometer (ATSR) and Global Ozone Monitoring Experiment (GOME) spectrometer. ATSR-2 consisted of the IR Radiometer (IRR) and the Microwave Sounder (MS), providing four IR channels, three VIS channels and two passive MW channels for measuring Sea-Surface Temperature (SST) and cloud-top temperatures, among other (Merchant et al., 2005). GOME is a VIS/UV spectrometer at the range of 240–790 nm consisting of three UV and two VIS channels (Loyola et al., 2010; Tuinder et al., 2002). The successor of ERS-2 is Envisat which is operational since 2002 and has the improved versions of the imagers of the ERS series such as the Advanced Along Track Scanning Radiometer (AATSR) and Global Ozone Monitoring by Occultation of Stars (GOMOS) spectrometer, instead of ATSR and GOME, and the MEdium Resolution Imaging Spectrometer (MERIS) (Gómez-Chova et al., 2007) consisting of 15 channels across the 390 nm to 1040 nm spectral range (European Space Agency, website), Gómez-Chova et al., 2010).

The NOAA-# (where # indicates the series number) is the Polar Operational Environmental Satellite (POES) series of satellites for weather purposes launched by the United States National Oceanic and Atmospheric Administration (NOAA) (Parikh, 1977; Uddstrom and Warreb, 1996). The last of them, NOAA-19 was launched on 6 February 2009. The former versions of the NOAA-# series was the Television Infrared Observation Satellite (TIROS-#) series (Cayula and Cornillon, 1996). The major

imagers of the NOAA-# satellites are the Advanced Very High Resolution Radiometer (AVHRR) (Bankert, 1994; Baum et al., 1997; Stowe et al., 1999) that has as primary purpose of providing global cloud imagery and measurements of sea/land temperature and the Advanced Microwave Sounding Unit (AMSU) which is a 20-channel microwave radiometer that measures brightness temperatures, water vapor profiles and cloud properties. The AVHRR collects radiance measurements of reflected solar radiation and emitted thermal IR in five spectral window regions. AVHRR's infrared channels are used to measure Sea Surface Temperature (SST) that represents the variation of the temperature of the surface (Bankert, 1994; Dybbroe et al., 2005a; Key et al., 1989; Parikh, 1978). The cloud classification accuracy for data taken from the NOAAs satellites ranged from 68.32% (Uddstrom and Warreb, 1996) to 96.3% (Parikh, 1978).

The corresponding polar orbiting European satellite series is called MetOp, the first of which was launched in 2006. Like the NOAAs, MetOp has on board the AVHRR and AMSU imagers. Furthermore, it has the Infrared Atmospheric Sounding Interferometer (IASI) that is used for temperature and humidity measurements and GOME-2 spectrometer that is the successor of the GOME spectrometer on the ERS satellite series (Lavanant et al., 2011; Schmetz et al., 2007).

Terra, also known as EOS AM-1 is a multi-national, multi-disciplinary sun-synchronous satellite launched in 1999. It has onboard the Moderate Resolution Imaging Spectroradiometer (MODIS imager) and the Multi-angle Imaging SpectroRadiometer (MISR) (NOAA – MODIS web (website)). MODIS collects data from 36 spectral bands, ranging in wavelengths from 405 nm to 14,385 nm, providing high radiometric sensitivity (Li et al., 2003). A Scan Mirror Assembly is using a continuously rotating double-sided scan mirror to scan the atmosphere over a ±55° range. The optical system consists of a two-mirror off-axis afocal telescope, which directs energy to four refractive objective assemblies; one for each of the VIS, NIR, short-wavelength IR/mid-wavelength IR and long-wavelength IR spectral regions to cover a total spectral range from 400 nm to 14,385 nm (Casanova et al., 2010; Cho et al., 2008; Houborg et al., 2007; Jedlovec and Haines, 2008; Lee et al., 2004; Li et al., 2003, NASA – MODIS web (website), Wind et al., 2010). The MISR observes earth at nine different angles (±70.5°, ±60.0°, ±45.6°, ±26.1°, and 0°), in four spectral bands (three VIS and one NIR) simultaneously (36 readings in total) and is used specifically for cloud and aerosols detection. The different observation angles of the imager obtain an alteration in the reflectance of aerosols, clouds land surface covers and through stereoscopic methods, the data are used to detect clouds and construct their 3D shape (Mazzoni et al., 2005, 2007; Shi et al., 2007). The cloud classification accuracy for the data taken from the MODIS imager ranged from 78% (Mazzoni et al., 2005) to 94.5% (Shi et al., 2007) and, Fig. 4 presents a schematic arrangement of the MODIS instrument (Xiong et al., 2008).

The Cloud-Aerosol LIDAR and Infrared Pathfinder Satellite Observation (CALIPSO) satellite is a sun synchronous satellite which was launched in 2006 to study the impact of clouds and aerosols on the earth's radiation budget and climate. The CALIPSO satellite has three instruments, the Cloud-Aerosol LIDAR with Orthogonal Polarization (CALIOP), the Imaging Infrared Radiometer (IIR) and the Wide Field Camera (WFC). CALIOP is an active LIDAR instrument with passive IR and VIS imagers to probe the vertical structure and properties of thin clouds and aerosols over earth (Cho et al., 2008; Hakn et al., 2008). The IIR is an imaging radiometer with three IR channels at 8,650 nm, 10,600 nm and 12,050 nm that provides measurements during night. The WFC is a 512 × 512 pixel CCD array that provides the data taken from CALIOP during daytime. The FOV (64 × 64 km) is centered at the CALIOP's spot at the ground.

CloudSat is a satellite that provides observations about cloud amount, distribution, structure, and radiative properties. CloudSat was the first satellite that integrated the

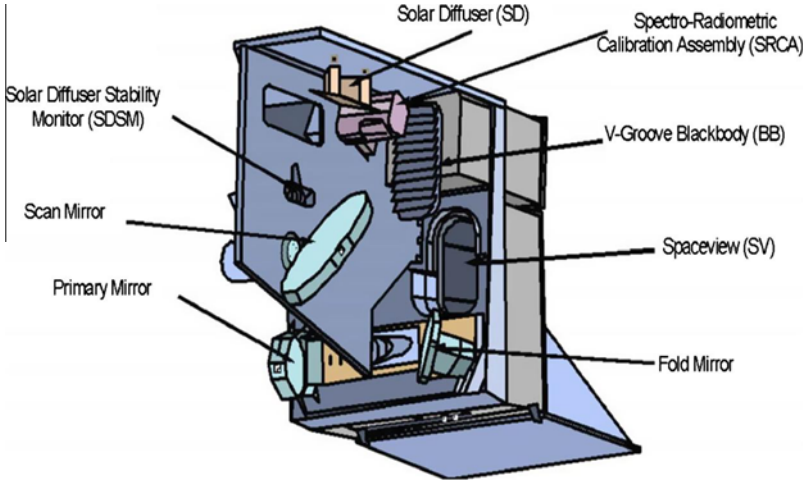

Fig. 4. A schematic arrangement of the MODIS instrument (Xiong et al., 2008).

very sensitive millimeter-wavelength Cloud Profiling Radar (CPR) that allows the detection of small particles of liquid water and ice, within large cloud masses (Hakn et al., 2008; Stephens et al., 2002). The combination of the measurements from these two satellites, CALIPSO and CloudSat, provides a 3-D perspective of how clouds and aerosols form, evolve, and affect weather and climate. CloudSat was manufactured concurrently with the CALIPSO to join three satellites already in orbit (Aqua, PARASOL, and Aura) and form a constellation of sun-synchronous satellites known as the A-Train to enable a comprehensive understanding of our climate system from the broad array of sensors on board the five spacecrafts (Joiner et al., 2010; Stephens et al., 2002). Fig. 5 presents the paths for 12 daytime A-Train orbits from August 2006 to June 2008 (Mecikalski et al., 2011). Aqua has onboard the MODIS imager (Minnis et al., 2008) and the Atmospheric Infrared Sounder (AIRS), designed to provide atmospheric temperature, water vapor profiles and cloud properties (Stubenrauch et al., 2008). Parasol has onboard the POLDER instrument that studies the microphysical properties of clouds. POLDER has 9 spectral bands that cover a spectral range from 443 nm to 910 nm (CNES, website), Waquet et al., 2009). The primary cloud monitoring instrument on Aura is the Ozone Monitoring Instrument (OMI). OMI is an UV/VIS nadir solar backscatter spectrometer, covering a total spectral range from 270 nm to 500 nm measures cloud pressure and coverage and distinguishes different aerosols in the atmosphere in order to derive the ozone in the troposphere (Joiner et al., 2010; Levelt et al., 2006).

The Defense Meteorological Satellite Program (DMSP) satellites, named DMSP-BB-F# (where BB is the block name and # indicated the series number) consists of sun-synchronous satellites that provide global VIS and IR meteorological, oceanographic and solar-geophysical data, used for defense operations (National Snow and Ice Data Center, website). Among other imagers, the satellites (F8, F10, F11, F12, F13, F15) have on-board the Special Sensor Microwave Imager (SSM/I) (Col and Mouchot, 1995; Mazzetti et al., 2001), which is a seven-channel passive MW radiometric system that measures brightness temperatures at 19.35, 22.2, 37.0, and 85.5 GHz.

The Tropical Rainfall Measuring Mission (TRMM) satellite was launched in 1997 in a non-sun-synchronous orbit at a low altitude height of 350 km, with an ultimate objective to measure rainfall over earth (Miller and Emery, 1997). Among other imagers, it has onboard the Precipitation Radar (PR), the TRMM Microwave Imager (TMI), the Visible InfraRed Scanner (VIRS), and the Clouds and Earth's Radiant Energy System (CERES) (Ho et al., 2003; Liu et al., 2008). TMI which is the evolution of SSM/I measures the intensity of MW radiation at five separate frequencies: 10.7, 19.4, 21.3, 37, 85.5 GHz and has the ability to quantify column water vapor for cloud and precipitation detection. Additionally, the VIRS has five spectral regions, ranging from VIS to IR in the range of 630–12,000 nm (Brown, 2006; Kubota et al., 2010; Minnis et al., 2008).

The Landsat-# program which started in 1972 with Landsat-1 (Clark, 1983) at first under NASA and then under NOAA responsibility consists of seven sun-synchronous satellites. Landsat-5 and Landsat-7 which are the last Landsat Satellite launched in 1999, are still functioning. They are near polar satellites, having as major activity

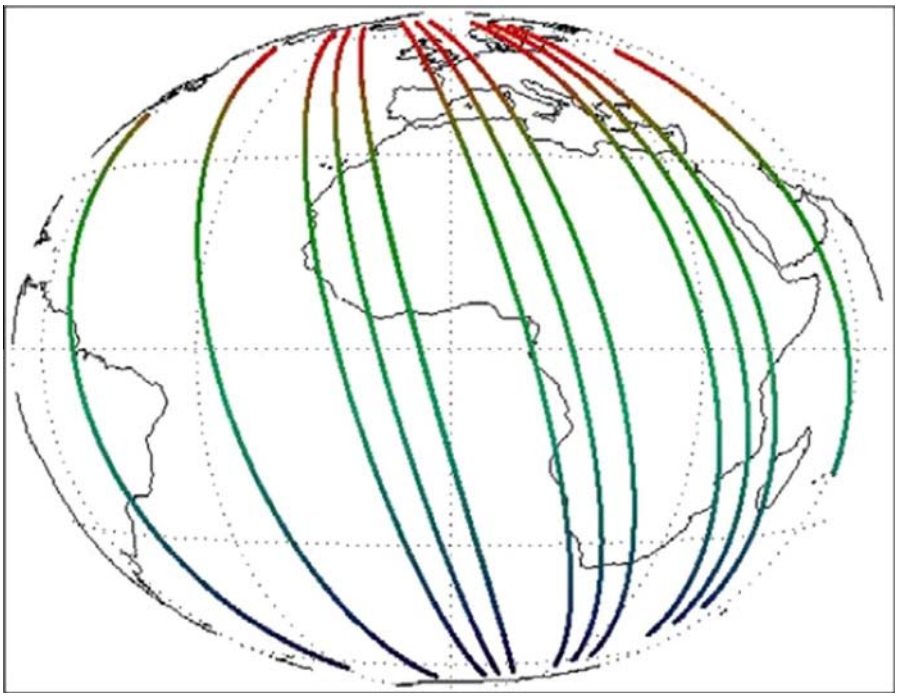

Fig. 5. Paths for 12 daytime A-Train orbits from August 2006 to June 2008 (Mecikalski et al., 2011).

the acquisition of information about earth from space (Marais et al., 2011). The imagers on-board LandSat-7 are the Enhanced Thematic Mapper plus (ETM+), that has eight channels (three VIS, four IR and one panchromatic), and the Multispectral Scanner with five channels in the range of 500–1100 nm (Cahalan et al., 2001; Irish et al., 2006; Sedano et al., 2011).

The Marine Observation Satellite 1 (MOS-1) also called Momo-1 and the Advanced Land Observation Satellite (ALOS), also called Daichi, are Japanese satellites. MOS-1 is a polar orbiting satellite and ALOS is a low earth orbiting satellite (Schneider et al., 1994; Tokuno and Tsuchiya, 1994). Both of them have three different operational sensors. ALOS has the most advanced imager from Japan's satellites: the Advanced Visible and Near Infrared Radiometer type 2 (AVNIR-2) comprised of four channels from 420 nm to 890 nm. MOS-1 has the older Visible and Thermal Infrared Radiometer (VTIR) (Tsuchiya and Tokuno, 1992), which is based on the research of Schneider et al. (1994), but cannot provide enough information to distinguish clouds from ice over land or sea.

Finally, Fengyun (FY-##) are China's weather satellites. As mentioned before, the satellites in the FY-1 and FY-3 series are in sun-synchronous orbits (Jian and Jianmin, 2008; Li et al., 2008). FY-3A is the successor of the FY-1 series and was launched in 2008 in order to make global observations of the earth's land, oceans, atmosphere and other parameters in real time. It has on board the Visible and InfraRed Radiometer (VIRR) which has 10 channels in the wavelengths 430–12,500 nm, the InfRAred Spectrometer (IRAS) which has 26 channels in the spectral range of 690–15,000 nm, MW imagers, UV imagers (19 channels in total) and solar radiation imagers (Dong et al., 2009; He, 2011).

3.3. Overall advantages/disadvantages of measuring equipment

The most important advantage of ground based equipment is that they provide on-site, real-time measurements continually. Once the instrument is installed, there is a continuity of measurements at user defined intervals at very high temporal resolutions up to 1 s. Most ground based instruments have a very low purchase cost, enabling researchers of long term, low cost measurements. The major disadvantage of ground based radiometers is that they have limited FOV (excluding pyranometers that have 180° FOV), although the installation of a tracker, or more than one instrument overcomes this problem, such as in the case of the CIR-7 or the Nubiscope. On the other hand, spectrum cameras provide high resolution images, yet their FOV is limited to the extents of the lens used; even all-sky cameras have limits to the photograph distance. Furthermore, the resolution of the all sky cameras becomes poorer and perspective issues arise towards the horizon. Irradiance meters are very simple to operate, although in order to be used for cloud detections they require great accuracy and appropriate maintenance especially in dusty areas. However, they only provide their measurements of integrated atmospheric effects such as cloud detections and estimation of cloud coverage, but cannot be used for cloud classification or for cloud height. Finally, Radars have very high resolution and accuracy in detecting clouds and distinguishing them from sky, but they cannot be used independently for cloud classification since they do not provide multi-spectral measurements for the acquisition of the necessary cloud properties. The integration of all the ground based equipment in one location, such in SGP CART site, or by Cloudnet network provides all the cloud information needed for classification, yet the high cost of the equipment and the specialization needed for the operation of the different instruments impedes their installation at solar RES sites.

The major advantage of the satellites is that they have a large FOV, which enables them to provide large scale cloud information. The multiple imagers onboard of the different satellites measure data at different spectral bands, enabling multi-measurement for specific areas and the collaboration of different satellites provides integrated measurements, such as the 3D perspectives of clouds. Furthermore, satellites' aerial view does not include the sun, overcoming a major disadvantage of ground-based cameras that is presented in Section 4.1.6. Moreover, due to their constant orbit (or geostationary position) they have the ability to collect data and develop a database of the landmark over time to be used for comparison with future views and detect clouds, as it will described in Section 4. The first major disadvantage of satellites results from their constant orbit. Non-geostationary satellites are not constantly over the same area, so they cannot provide continuous measurements, while geostationary satellites have a specific FOV over an area and cannot provide measurements for a different area. The second major disadvantage is their low spatial and temporal resolution compared to most of the ground based instruments. Non-geostationary satellites record one set of measurements per orbit, while geostationary satellites have at least 30 min intervals between the measurements. Moreover, due to their extremely large FOV, their spatial resolution is very low, so their cloud detection capability is limited to large clouds. Of course, this disadvantage will be solved by the development of better imagers with higher resolution. Another disadvantage is the high cost of acquisition of measurements from the satellite operator, especially for small to medium scale solar RES sites.

Radiosondes have the advantage of providing real-time, reliable measurements for cloud properties over multiple atmosphere layers, at every desirable location. Nevertheless, since the balloon is constantly moving upwards, the measurements are allocated to every height for the precise time when they were recorded. Thus, radiosondes cannot be used for continuous, sequential measurements over a desired site. Furthermore, the preparation of the release of the meteorological balloon has to be prepared manually, limiting the automation of the method.

These advantages and disadvantages of the different measuring instruments prompted researchers to develop different approaches for distinction and classification of clouds based on the limitations of the instruments. In the following chapter we present in detail the different techniques used for cloud distinction and classification.

4. Methodologies/algorithms/modeling for cloud classification

Automated cloud classification algorithms are being developed in order to eliminate the need for human observers. The different techniques that are presented in this chapter were developed due to the different hardware used to estimate the state of the sky, and thus the presence of clouds. Some of these techniques are universal and could be used regardless of the technology used, whereas other techniques can only be used exclusively for a particular methodology.

The simplest method used is the linear threshold distinction where, depending on the measurements of the instrument, the "object" is classified as cloud or not cloud. The distinction may be achieved directly using the measurements or indirectly, by digitalizing the measurements and then using image processing techniques on the data acquired (Biday and Bhosle, 2010; Kegelmeyer, 1994; Mukherjee and Acton, 2002).

Some methodologies classify clouds by type directly (Calbó and Sabburg, 2008; Duchon and O'Malley, 1999; Orsini et al., 2002) whereas some involve a two-step process; a preprocessing to distinguish clouds from sky/land, followed by the type classification step (Bankert and Wade, 2007; Christodoulou et al., 2003). It should be mentioned that throughout this chapter, the term "distinction" is used for distinguishing clouds from sky/land whereas the term "classification" means the categorization of clouds by type.

This chapter is divided in four parts. In the first part we present the different methods available for distinguishing clouds from sky/land. In the second part, several different classifiers used by researchers to classify the clouds by type are presented and in the third part, a small review on CBH calculation methodologies is presented, as this parameter is of great importance for the various detection algorithms and classifiers. Finally, in the fourth part, a list of the published research on cloud classification is presented in tabular form. Some of the researchers have developed and use algorithms that simultaneously distinguish clouds from sky/land and classify them by type. Thus, their methodology is presented in both the first and the second part of the chapter.

Relevant reviews on cloud classification techniques were published more than 20 years ago by Goodman and Henderson-Sellers (1988) and by Ruprecht (1985). A more recent review was presented by Jedlovec (2009) that focused on the automated detection of clouds in satellite imagery. However, the scope of the reviews is limited (i.e. only the spectral range of the imager used and the comparison of the Bispectral Composite Threshold (BCT method and the MODIS algorithm are analyzed by Jedlovec (2009)), while the aim of the current chapter of the review is to present all equipment and algorithms available for cloud classification purposes, with an indirect aim of being able to calculate solar energy reduction due to the presence of clouds.

4.1. Distinguishing clouds from sky/land

The first step in cloud classification algorithms is to detect clouds from sky/land. If the imager is ground based, then the algorithm distinguishes the sky from the clouds and from the sun. If the imager is on a satellite, then the algorithm distinguishes the clouds from land, sea, snow and buildings. The selection of the technique to be used for the distinction of clouds from sky/land is interrelated to the measuring equipment used. Independently of the equipment used for the measurements, the raw data is presented as an order 3 tensor. The tensor is the equivalent of a stack of 2D images, where each layer represents the measurements from a different instrument for the same scene. The value of each entry of the matrix indicates the measurement of the instrument for the specific place of the FOV. For example the input from the MODIS imager will be in the form of a seven layer 2D matrix: four layers for the IR channels and three layers for the red, green and blue compounds of the VIS channel. When the matrix is processed, regardless of the methodology, a white and black color value is assigned to the 2D matrix where the first color (ex. white) represents the clouds and the other (ex. black) represents the rest of the image. In some of the techniques presented in the following chapter, the classification of the clouds is computed simultaneously with the distinguishing of the clouds from sky/land. If more than one measuring instrument is used, then, before the evaluation of the measurements, the raw data must be preprocessed and integrated to the same scheme and resolution (Col and Mouchot, 1995). This preprocessing is applied to data taken from different satellite imagers or data taken from different ground based instruments. An example of the combination of data from different imagers of the TRMM satellite was presented by Liu et al. (2008).

In the following subsections, we present the distinction of clouds from sky/land based on spectrum and broadband irradiance analysis. The distinction using spectrum analysis is an image processing technique based on the differences in the intensity (or color) of each pixel of the image captured by the imager. The color/intensity of an image from a common camera represents colors in the same way as the human eye perceives them. In contrast, the colors of an image from an IR camera represent the differences in temperature between the objects in the picture and the colors of a UV camera represent the intensity of the UV radiation. These methods can be used for processing data from all ground based spectrum cameras (Heinle et al., 2010; Roy et al., 2001), radiometers (Estupiñán et al., 1996; Gillotay

et al., 2001; Orsini et al., 2002) and satellite imagers (Cho et al., 2008; Stowe et al., 1999). Distinction based on broadband irradiance analysis is based on the fact that solar irradiance (direct, diffuse and global) is attenuated or enhanced due to the presence of clouds or that irradiance of specific wavelength is absorbed by cloud particles. Finally, active remote sensing instruments compare the characteristics of the transmitted and backscattered signal to detect clouds at multiple layers of the atmosphere (Clothiaux et al., 1995; Zhang et al., 2010).

4.1.1. Visible spectrum analysis

Analysis of the visible spectrum is usually used for processing data from all ground based spectrum cameras and satellite imagers.

4.1.1.1. Simple intensity threshold analysis. The simplest method of distinguishing the clouds from sky/land is using the pixels' intensity (Biday and Bhosle, 2010; Mukherjee and Acton, 2002). The technique is based on the difference in the intensities of different objects in the picture. The input data is captured from a gray-color (or color) camera and then, an algorithm distinguishes the objects based on the gray value level of the pixels by setting a threshold range. For color cameras, the classifier uses the average intensity of the three basic colors (red–green–blue, RGB) of the image. This technique can also be used for the direct classification of the clouds, although the accuracy is very low. The threshold range proposed by Kegelmeyer (1994) for an 8-bit gray image is as follows:

- 0: pixels outside of the camera's field of view, or hidden by occulator.
- 1–99: Clear sky pixels.
- 100–139: Thin cloud.
- 140–200: Opaque cloud.
- 201–255: Off scale, unclassified

4.1.1.2. Ratio Red/Blue (R/B) threshold technique. The Ratio Red/Blue (R/B) threshold technique is used mainly for images using ground cameras. The method is based on the red-to-blue ratio (the ratio of red to blue spectrum) for every pixel of the image captured from the camera (Johnson et al., 1989; Shields et al., 1998). In a cloud-free atmosphere, which appears blue to our eyes, more light within the blue spectrum is scattered by gas molecules. On the other hand, clouds consisting of water and ice particles, scatter the same amount of blue and red spectrum, and appear colorless (ranging from white to dark gray) to our eyes (Chow et al., 2011; Petty, 2006; Roy et al., 2001). Thus, clear sky sections of an image have relatively lower red pixel values compared to cloud sections, and thus they can be distinguished using a red-to-blue threshold. The exact value of the separating threshold depends on the camera and the atmospheric conditions, so it has to be determined empirically. Furthermore, the threshold limit is not the same across the entire image but is determined by the clear sky library function, determined by the relative position of the image pixel and the sun (Shields et al., 2009). This is necessary because of the angular dependence of the light scattering processes, and also due to the effects of the increased light pathlength with increased solar zenith angle (Chow et al., 2011; Long et al., 2006; Pfister et al., 2003). The R/B threshold criterion has some complications in detecting thick clouds and classifying clouds in the circumsolar region at the same time or in detecting very thin cirrus clouds since same pixels might have an R/B ratio below the threshold used. Heinle et al. (2010) modified this criterion and considered the R–B difference instead of the R/B ratio. Comparisons showed that segmentation using the difference threshold method still results in minor errors, but outperforms the ratio threshold method.

4.1.1.3. IHS threshold technique. The Intensity, Hue, and Saturation space (IHS) threshold technique uses the intensity, hue, and saturation components of an image to obtain the distinction between clouds and sky. In the IHS system, the intensity (I) represents the brightness sensation felt by the eye/camera and is defined as the total energy in all wavelengths that reaches the eye/camera. Hue (H) is the expression of the degree of similarity of a color compared to the unique spectrum colors (red, blue, green and yellow) and is calculated by measuring the reflected or emitted spectral light. Saturation (S) is the colorfulness of a color relative to its own brightness, expressing the color purity. The principle behind this methodology is based on the optical characteristics of clouds in the visible range of the solar spectrum taking into account the different wavelengths captured by the camera (Davis et al., 1992). The RGB color space image of the sky is transformed to the IHS space. The IHS color attribute space does not work directly with the three colors like the RGB space, but it represents the way the humans can identify the source of color attributes (Souza-Echer et al., 2006). Clouds have high reflectance, and thus a predominantly white color (caused by multiple scattering while clear skies, during daytime show mainly blue light tones, with color shades ranging from green to red, which typically result in high saturation values. Following this scheme, clouds show lower saturation values, and clear skies show high saturation values. Thus, saturation is selected as the component from the IHS space to be used in the development of every cloud/sky distinction algorithm. Similarly to the RGB method, the exact value of the saturation threshold range to separate clouds from sky depends on the camera and the atmospheric conditions, so it has to be determined empirically (Roy et al., 2001).

4.1.2. Infrared (IR) analysis

The IR cloud detection/distinction and classification algorithms are based either on statistical methods through the comparison of the cloud's emitted IR radiance with a

black body calibration source or directly by using a threshold value to classify the clouds within a preselected range. The fundamental principle used in the IR method is that clouds have different emissivity at thermal and infrared bands from that of land or sea and this difference can be detected by the IR camera based on their Brightness Temperature (T_b) differences. For example, cloud emissivity is lower in the shortwave (SW) than in the longwave (LW) IR wavelengths and depends on cloud type. The computation of clouds' emitted blackbody radiation is based on Wien's law that states that the shape of the wavelength distribution emitted by a blackbody is temperature independent; the variation of the blackbody's temperature causes only a displacement of the distribution. The energy emitted by a blackbody as specified by the Stefan–Boltzmann law varies as the fourth power of the object's temperature (Gillotay et al., 2001).

4.1.2.1. Satellite IR imagers. Clouds at a particular height appear warmer compared to cold background clear sky (Anzalone et al., 2009). The contrast level between the temperature of clear and cloudy sky depends on the wavelength band selected, the emissivity of the cloud and the emission intensity of clear sky. IR measurements of sky at wavelengths between 8,000 nm and 14,000 nm are sensitive to the presence of clouds (Maghrabi et al., 2009), and an imager for the acquisition of the necessary data may be ground-based or positioned on a satellite (Feister et al., 2010). Since the cloud emission signature is the same both during day and night, the IR method provides a significant advantage over visible wavelength imagers in being able to produce a continuous day-night data stream with no change in sensitivity or in the cloud-detection algorithm (Brocard et al., 2011; Shaw and Thurairajah, 2005). For gray-scale satellite IR images, cold high level clouds with low IR radiance appear white, warmer low-level clouds appear gray, while sea/land with higher near surface temperature looks relatively dark in the IR data. In contrast to ground based IR measurements, clouds appear darker than the colder background sky which appears white (Christodoulou et al., 2003). Most of the IR cameras use a pseudo-color correspondence of the measurements using the colors of the optical spectrum for easiest and faster visual perception of the measurements for the user. In most images blue represents the colder areas of the image, whereas red represents the hotter areas and the other colors are used as intermediate gradations (Brocard et al., 2011). Complementing measurements from two IR sensors at different wavelengths can provide greater accuracy in distinguishing clouds from sky, since they can provide different reflectance (Chiu et al., 2006).

4.1.2.2. Analysis using IR images for landmark signature. A different technique, applied only to satellite measurements, is to store the landmark signature of the IR backscattering radiation and to compare it to the data from the imager (Parikh and Ball, 1980). Cayula and Cornillon (1996) used a multi-image stack of the landmarks; every image was compared to the same landmark within 50 h before and after the image under investigation was taken, since longer periods may affect the landmark's signature. The temporary difference in the radiation of two adjacent pixels indicates the presence of a moving cloud, that can then be classified, while a permanent difference indicates the presence of different objects in the picture such as water masses next to land. One advantage of this IR emission signature algorithm is that detection of clouds in the Arctic environment is possible, since clouds stand out against the cold, clear background. This method is especially useful for the detection of thin clouds that would not at all be obvious to a visible-wavelength camera. The extremely low water vapor content of the wintertime Arctic atmosphere allows IR cameras to detect an extraordinarily high radiometric contrast between clear sky and thin clouds. In other locations with higher water vapor content, thin clouds will be more difficult to be detected using this technique (Shaw et al., 2002).

4.1.2.3. Ground based IR images. In the case of ground based measurements, the measurements must be preprocessed and calibrated to produce radiometric images with units of band-averaged radiance (watts per square meter steradian). For the measurements from the ICI for example, two subsequent IR images of the sky and blackbody being used are averaged (a larger number of images can be averaged to reduce noise), and then are calibrated using a linear calibration equation. Then, the near-surface air temperature is used to choose which atmospheric model is closest to the actual conditions for the data acquired by the instrument. Clouds are identified and classified from the radiance value in each pixel of the image (Shaw and Thurairajah, 2005).

4.1.2.4. Analysis using specific IR wavelengths. Analysis of measurements in the NIR band at 940 nm can be used for the detection of water vapor columns from several instruments, as described in the previous section (Halthore et al., 1997; Harrison et al., 1994; Kassianov et al., 2011a, 2011b; Kiedron et al., 2006; Michalsky et al., 2001). The water vapor column of clear sky is considerably lower than that of cloudy skies. This difference is not constant, but depends on the tropic region of the measurements, the type of cloud, the optical depth, etc. (Gaffen and Elliot, 1993; Wind et al., 2010).

Another technique used, especially for the detection of cirrus clouds is the CO2-slicing technique, that uses four or more IR spectral bands in the range of 13,300–15,000 nm (Mahesh et al., 2001; Menzel et al., 2008; Wind et al., 2010). The absorption of the radiance from CO_2 is more intense in this range and varies for each particular band at the different layers of the atmosphere. From the processing of the absorption data (low clouds do not appear in the "high level" bands while high clouds appear in every band), and other weighted cloud parameters

obtained from the imager, the cloud top pressure is assigned to a cloud element and thus the CBH can be estimated (Hendricks et al., 2010; Wylie and Menzel, 1989, 1999).

Gao et al. (2011) presented a technique similar to the CO_2-slicing technique to be used from imagers that do not have longwave IR channels. Their proposed method utilizes the three midwave IR channels (4,390–4,550 nm) of MODIS and is based on the combined CO_2 and N_2O absorption effects in the spectral region near 4,500 nm which have similar properties to the longwave IR CO_2 slicing channels.

4.1.3. UV distinction analysis

The ultraviolet distinction method is based on the UV radiation and more specifically of UV-B (280–320 nm) differences due to clouds (Mckenzie et al., 1998; Parisi et al., 2008; Sabburg and Calbó, 2009; Villán et al., 2010).

The presence of clouds in the atmosphere affects UV radiation at ground level by either reducing it or in sometimes by enhancing it, depending on cloud optical thickness, cloud type and height, cloud structure and location of cloud between the sun and the measuring instrument (Anthis and Cracknell, 2004; Vasaras et al., 2001).

Reduction occurs due to absorption of UV irradiance from clouds whereas enhancement takes place due to the scattering of radiation on clouds surface that leads to its amplification, especially for partial cloudy skies. The influence of clouds on UV radiation has been thoroughly studied (Alados-Arboledas et al., 2003; Foyo-Moreno et al., 2003; Mayer et al., 1998; Parisi and Downs, 2004), so using a reverse perspective, cloud distinction and cloud type can be estimated from UV measurements (Calbó et al., 2008; Estupiñán et al., 1996). In contrast to passive ground based UV measurements, satellite imagers consist of active UV channels that measure backscatter UV radiation using the same principle as LIDAR. The equipment used for the measurements is a UV sensor or camera that measure the incident radiation only in the UV spectrum (Long et al., 2006; Sabburg and Wong, 1999; Winiecki and Frederick, 2005). An empirical study of cloud effect on UV radiation was presented by Calbó et al. (2008) and by Villán et al. (2010).

4.1.4. Visible/IR–visible/UV analysis

A hybrid technique is the VIS/IR or VIS/UV analysis which comprises of both the visible and IR/UV threshold techniques. For the implementation of these techniques the inputs from two different sensors, one in the visible band and one in the IR band or UV band are used.

One of the VIS/IR techniques being used, the direct sequential clustering method, is being used both for the distinction of clouds from sea/land and for the classification of clouds based on a threshold value of the albedo and the observed temperature. Albedo is the reflection coefficient of a surface (land) and is defined as the ratio of the reflected radiation from one surface to the incident radiation on the same surface. The method is based on the simultaneous analysis of two images of the same scene, one acquired in the visible band (corresponding to the albedo) and the other in the IR band (corresponding to the temperature). Each pixel is associated to a couple of radiometric values based on its spectral signature (albedo level $\times$ band of thermal emission) and thus it can be defined as a point on the radiometric VISxIRplane. The different types of objects existing in the image (i.e. sea, ground and types of clouds) have a different albedo and temperature signature, thus corresponding to a different location of the radiometric VISxIR plane (Bonomo and Brignoli, 1998; Ruprecht, 1985; Saitwal, 2006).

A similar approach is the Bispectral Composite Threshold (BCT). BCT is a threshold comparison method proposed by Jedlovec and Haines (2008) applied for data taken from any kind of VIS/IR imager on board of a satellite with very few modifications. Because of the different cloud and surface properties, the spatial transition from a clear region to a cloudy region, as recorded by a satellite imager, is apparent as a discontinuity in the LW minus SW brightness temperature difference image. Since different types of clouds have different properties, the successful detection of clouds lies in the selection of an appropriate threshold value for the distinction between clouds and land. The technique uses a database of the properties of the landmark in order to use a different threshold value from one pixel to the next and therefore location, terrain, sun angle and snow cover are taken into consideration as background data (Jedlovec and Haines, 2008; Jedlovec, 2009).

Similar to the VIS/IR technique, VIS/UV integrates Visible and UV thresholds to detect clouds (Loyola et al. (2010)). This hybrid technique is very useful for detecting clouds located near the sun's circle in the image, as will be thoroughly analyzed in Section 4.1.6 (Parisi et al., 2008; Sabburg and Wong, 1999).

4.1.5. Microwave analysis

The microwave distinction technique employs MW radiation for cloud detection utilizing the strong attenuation of MW radiation by clouds in the atmosphere (Pujol et al., 2007). Microwave sensors can be passive or active (Mazzetti et al., 2001), where passive sensors (radiometers or satellite imagers) record the MW radiation emitted by the atmosphere, or emitted/reflected from the surface and active systems, such as Radars, transmit MW signal and detect the time delay (height estimation) and reduced strength (cloud classification) of the backscattering signal (Randriamampianina et al., 2000; Weng, 2011). Due to the long wavelengths (1–10 cm) of MW, the field of view of the instruments must be very large in order to record the signal. Thus, the "microwave index" is an empirical threshold, related to the MW channels of the instrument, which represents the strength of the MW signals due to the presence of the clouds (Liu et al., 1995).

Finally, an integration of the measurements from IR and MW satellite imagers is used primarily for the estima-

tion of water clouds and precipitation. The IR/MW technique is used to overcome the limitations of VIS/IR in estimating the properties of deep thick clouds because of the saturation of both VIS and IR radiation in them and the limitations of the exclusive use of satellite MW imagers which cannot obtain the cloud height (Brown, 2006). The major disadvantage of this technique is that apart from the TRMM satellite, the other satellites are not equipped with an IR and MW imager, so the data are taken from two different satellites (Liu et al., 1995; Prakash et al., 2009). The distinction of clouds from land/sea is obtained from their emitted IR radiance as described previously in this section. The computation of the inputs from the two imagers provides the information for the distinction of clouds from sea/land and their further classification.

4.1.6. Cloud detection within the sun circle

In cloudless sky conditions, the pixels of an acquired image in the VIS spectrum, forming a circle at an approximate 20° field of view centered over the sun's position, often seem whiter and brighter than the rest of the hemisphere. Thus, the sky around the sun can appear to be cloudy, even if it is not. This may occur because of forward scattering from thin cirrus clouds or boundary layer haze, which is subvisible elsewhere in the image or because the camera sensor is overloaded and blooming. Even a slight haze or moderate aerosol loading will make a large angular area of the horizon whiter and brighter when the sun is low on the horizon (Chow et al., 2011; Long et al., 2006; Pfister et al., 2003). Consequently, various researchers have attempted to remove this sun interference from the images.

The use of filters before the lens of the camera is a very effective way of protecting the sensor of the imager used, but is not suitable for removing the brightness due to the scattering of light. A preliminary solution to this problem is to use a sun tracking occulator (shadow band) (Martínez-Chico et al., 2011; Pfister et al., 2003) to block the sun and thus remove direct sunlight from the image, although since the sun is always covered from the occulator, it is impossible to detect cloud presence coverage at the sun's location (Calbó and Sabburg, 2008; Long et al., 2006; Slater et al., 2001). Using the same principle, (Cazorla et al., 2008a, 2008b) developed a custom made occulator by modifying a sun tracker used for DNI measurements and used it for shadowing an all sky camera as shown in Fig. 6 (Cazorla et al., 2008a). Feister et al. (2000) however, used an occulator with a neutral density filter and the sun could be seen in the image only as a small spot that cannot be confused with clouds.

Other methods have also been proposed by other researchers. Heinle et al. (2010) assumed that at the location of the sun circle, all the pixels are completely white if there are no clouds, so they applied a mask and set all corresponding pixel values to zero. Pfister et al. (2003) proposed the term "sunshine parameter" as an indicator of whether the sun is obscured by clouds. The sunshine parameter was determined by applying a statistical quality control procedure that used the mean and standard deviation of the cloud coverage centered about the image of interest, using twelve sequential all-sky images, taken at 1 min intervals. If both the cloud coverage of the image and its variance over the sun circle during the 11 min period are small, then it was most likely that there were no clouds around the sun. Conversely, if there was a large inconsistency in the cloud fraction within the sun circle and significant cloudiness in the rest of the sky over the short period, then at least a part of the sun circle was covered by clouds at the time of interest. A similar statistical

Fig. 6. A custom made occulator protecting an all-sky camera (Cazorla et al., 2008a).

approach for an all sky camera was proposed by Long (2010). From consequent images taken from the camera, the area of the sun circle in the pictures and along an imaginary horizon centered at the solar azimuth angle were processed using a statistical analysis. The standard deviation of the sky cover for the circle/horizon, the horizon area sky cover amount and the sky cover amount for the rest of the picture were calculated and using empirical thresholds, the cloud cover over the sun circle were estimated.

Sabburg and Wong (1999) at first and then Parisi et al. (2008) proposed a VIS/UV threshold technique to distinguish clouds from sky in the area around the sun. The method employs three solar detectors for monitoring the UV-B (280–320 nm), UV-A (320–400 nm) and total sunlight (400–950 nm) bands. The procedure behind this method is to store three different types of pictures for every capture. The first is a red-filtered RGB picture (processed to have 0% hue and 100% saturation); the second is a gray-color picture filtered using a neutral density (ND4) filter, and the third is a RGB picture. The green component of the first picture is used to identify the sun's location in relatively cloudy conditions, since the sun's disk is of maximum contrast. The analysis of the three images provides optimum contrast between clouds and sky. The red component of the third picture together with the second picture is used in identifying clouds in relatively cloudy conditions. The second picture is used for locating the sun and identifying cloud in all other sky conditions, while the identification of clouds is based on a variable threshold value that depends on several features, and the selection of the proper image among the three is based on the information taken from the UV sensors in correlation to a selected clear-sky image or reference image (Long et al., 2006; Sabburg and Wong, 1999).

4.1.7. Distinction using broadband irradiance analysis

The simplest irradiance technique utilizes the data from any of the irradiance measuring instruments to determine the presence of clouds occurring at the measurement site during daylight hours. In order to analyze the results from these instruments, various algorithms can be used. Simple statistics (mean and variance) can be derived from the time series of the irradiance, as measured by the instrument and further analyzed (Duchon and O'Malley, 1999; Orsini et al., 2002). The time series of irradiance captures the character of the cloudiness weighted towards the portion of the sky where the sun is located and provides the basis for estimating cloud type.

During clear sky conditions the irradiance signal is dominated by the solar beam and diffuse irradiance which occurs due to scattering of solar irradiance by atmospheric molecules is a small part of the global irradiance. During partial cloudy conditions, more irradiance is scattered or reflected due to clouds resulting to an increase of diffuse irradiance. In general, during cloudy conditions, if clouds do not cross the sun-path, DNI remains the same but diffuse irradiance is increased. On the other hand, if clouds cross the sun-path, DNI is reduced according to the type and opacity of the clouds and diffuse irradiance is increased. Therefore, the signal varies principally in response to whether clouds cross the sun-path or not and secondary to cloud coverage resulting to variations of the Diffuse to Global irradiance Ratio (DGR). Finally, at a mostly overcast day, DNI is approximately zero and global irradiance depends primarily to diffuse irradiance so the ratio of DGR becomes nearly one (Duchon and O'Malley, 1999; Kaskaoutis et al., 2008; Orsini et al., 2002). Fig. 7 shows the variation of the measured 10 min average short wave (300–3000 nm) radiation for a partly cloudy day and is compared to the calculated irradiance for the same day (Orsini et al., 2002) for clear sky conditions, while Fig. 8 shows the variation of global and diffuse 10 min average irradiances at different wavelengths (Kaskaoutis

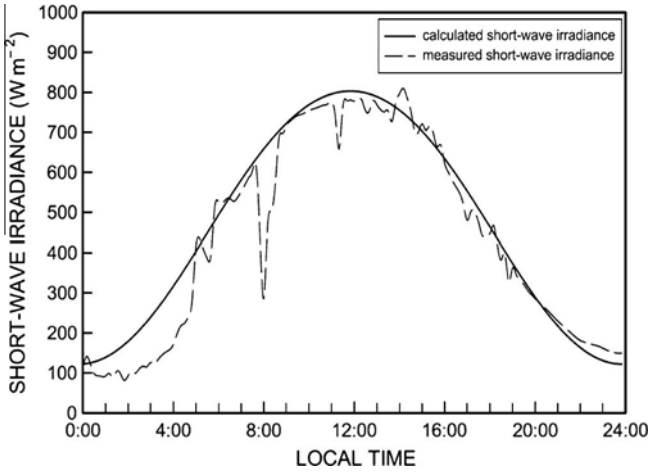

Fig. 7. Comparison between the time-patterns of the incoming 10 min average short-wave (300–3000 nm) radiation flux (dashed line) for partly cloudy conditions, and those of the short-wave irradiance (solid line) calculated for the same day in December 1994 (Orsini et al., 2002).

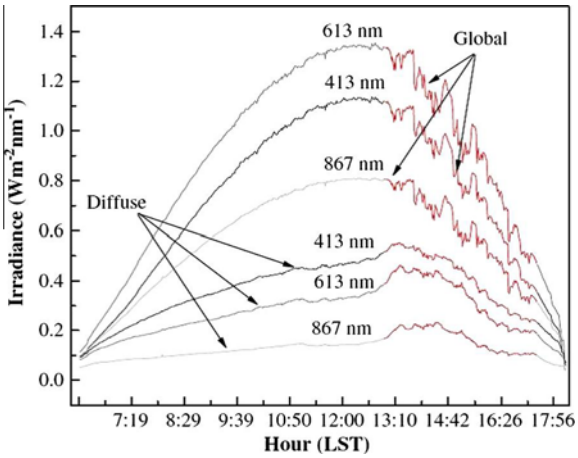

Fig. 8. Diurnal variation of global and diffuse irradiances at different wavelengths in Athens in May 2005. The perturbed data after midday was probably attributed to cirrus clouds undetected by naked eye (Kaskaoutis et al., 2008).

et al., 2008). Furthermore, as shown in Fig. 7, in some cases the measured value of global irradiance is greater than the calculated value from the clear sky model which is due to the particularly enhanced irradiance from reflection effects by clouds, when clouds do not cross the sun-path. The dips in the measured irradiance in Fig. 7 are the result of the reduction of global shortwave irradiance, indicating the presence of clouds in "front" of the sun (Orsini et al., 2002).

Duchon and O'Malley (1999) at first and then Orsini et al. (2002) estimated that for a clear day, approximately 15% of the global horizontal irradiance is diffuse, during an overcast day the DGR is approximately equal to one and during a partly cloudy day the DGR is variable but always greater than 0.15. Moreover they proposed a threshold technique based on the parallelepiped classifier (as it will be discussed in Section 4.2.1) for cloud classification. The parameters they used for the classification are the standard deviation of the scaled observed irradiance and the ratio of scaled observed irradiance to scaled clear sky irradiance. They used scaled values of irradiance in order to smooth the non-stationary daily time series. Orsini et al. (2002) used the same technique but using different decision criteria. Kim et al. (2006) proposed a cloudy sky threshold equal to 0.03 as the ratio of the standard deviation to the 3-min averaged measured irradiance from a broadband MFRSR (300–1,100 nm). Martínez-Chico et al. (2011) used similar principles but introduced an additional parameter: the cloud coverage as computed from the R/B ratio from an all sky camera. Pagès et al. (2003) combined the measurements of total irradiance, temperature and relative humidity to provide real time, cheap and easy to use technique for the detection and classification of clouds.

4.1.7.1. Hybrid broadband irradiance analysis. Feister and Gericke (1998) and Vasaras et al. (2001) proposed a hybrid technique, employing measurements from at least two UV spectroradiometers and one pyranometer for distinguishing clouds from sky and preliminary classification for bright/dim sky conditions and whether the sun is obscured by clouds. Their proposed techniques utilize the benefits of the UV distinction method and distinction using irradiance as described in the previous paragraphs. The disadvantage of their method is the long time intervals (8-min (Vasaras et al., 2001)) or longer (Feister and Gericke, 1998) of the measurements due to the multiple scanning of the spectroradiometer, thus limiting measurements for fast moving clouds or clouds with variable optical depth.

4.2. Classifying clouds by type

Classifiers are used to differentiate clouds by class, based upon the designated cloud characteristics (i.e. features). The classifier may use just one feature for the classification, or numerous features, which in most cases overlap within different classes (Christodoulou et al., 2003). The features of the clouds are defined after the distinction of clouds from sky/land, when the input data are modified to include only the input parameters regarding clouds. The rest of the image that may contain the sky, the occulator or the sun for ground based measurements and the sea, land, ice, buildings, etc. for satellite based measurements is ignored and thus not processed. This processing step does not take place in the cases where the classifiers distinguish clouds from sky/land and classify clouds simultaneously. In these cases, the features of the clouds are processed along with the features of every other object in the image. In fact, several researchers classify in addition to clouds, land, sea or ice (Azimi-Sadjadi and Zekavat, 2000; Dybbroe et al., 2005a, 2005b; Liu et al., 2009; Mazzoni et al., 2005; Ricciardelli et al., 2010; Shi et al., 2007; Tian et al., 1999, 2000).

The features are divided in spectral, textural, contextual and physical. Spectral features describe the average color and tonal variation of a cloud image. In cloud classification they are useful to distinguish between thick dark clouds, such as cumulonimbus, and brighter clouds, such as high cumuliform clouds, and to separate high and transparent cirrus clouds from others. Spectral features support a division of cloud classes, but considering only these features is not sufficient. They do not provide information about the spatial distribution of color in an image which is significant for cloud type recognition since in some cloud types (i.e. cumulus, altocumulus and stratocumulus) mean color values are similar but the spatial distribution is different (Heinle et al., 2010). Textural features refer to the spatial (statistical) distribution of tonal variations within an image, i.e. the homogeneity, randomness and contrast of the gray level differences of the pixels. The human eye can perceive this spatial distribution as variations in the intensity patterns or gray tones (the varying shades of gray) of an image. Since textural feature are applied to gray-scale variations, they can be derived from measurements from all instrument types. The value of the measurement specifies the gray tone intensity of the corresponding pixel as proposed by Haralick et al. (1973). The Gray-Level Co-occurrence Matrices (GLCMs) (or gray level difference vector) are used to classify textural features. The matrix may be an array, focusing on the difference between the gray level value of two pixels or a square matrix where the co-occurrence of the specific pixel pairs is computed. The second order GLCM is a square matrix for which the number of rows equals the number of gray levels in the considered image. Every matrix element represents the relative frequency that two pixels occur, separated in a defined direction by a pixel distance (Baum et al., 1997; Heinle et al., 2010; Uddstrom and Warreb, 1996). Contextual features refer to the geographical location of an object (i.e. pixel) in an image, the observation angle of the instrument, the time and day of year and specific local information (Mazzoni et al., 2007; Haralick et al., 1973). Physical features concern the physical properties of a cloud such as brightness, temperature and whiteness. These features are always present in an image, although many times one property

dominates over the others (Wang and Sassen, 2004). Furthermore, an overall feature category is the cloud coverage which is a measure of the average cloudiness. It is the most useful feature used for estimating either spatial or time-averaged irradiance based on very simple models but not for solar irradiance estimations over a site at a specific time where more cloud parameters are required.

In the following section, we have grouped the classification methods in three groups: Simple, statistical and artificial intelligence classifiers. The simple group consists of the simplest algorithms that demand low computational power and classify directly the clouds into the predefined classes using linear equations that may be based on empirical parameters and they do not have restrictions on the number of features used (Calbó and Sabburg, 2008; Tag et al., 2000). Due to their simplicity, classification mismatches may occur reducing the algorithm's accuracy. The statistical group consists of more complex algorithms, where a statistical model is used to classify the clouds and may involve a training sample. They are used for multi-spectral or multi-feature inputs and demand longer processing power and time (Cheruy and Aires, 2009; Paliwal and Kumar, 2009). Finally, the artificial intelligence group consists of the artificial neural networks classifiers, the fuzzy logic classifiers and support vector machine classifiers. Artificial intelligence algorithms are very flexible since they simulate the decisions of human brain so they can learn during the processing of new data. This advantage may lead to their major disadvantage since they depend to a large extent on the training sample (for supervised) or the "quality" of the data. Repeated input of low quality data may result to permanent wrong results, while even if the users are aware of the fault results, they cannot spot the error in the algorithm to correct it (Mellit and Kalogirou, 2008; Paliwal and Kumar, 2009).

For consistency, the following terms will be used in the remaining of the section, regardless of the terms used by the researchers. "Inputs" represents the data taken from the measuring instruments, "features" represents the clouds specific parameters, "data space" represents the matrix or matrices of the data that is used from the classifier, either raw or processed, "distinction" refers to the separation of clouds from sky/land, "classification" refers to the categorization of clouds by type, "Region Of Interest (ROI)" refers to the image part considered for cloud classification and "boundaries" refers to the features restrictions applied on a cloud in order to be classified under a specific type.

Furthermore, there are two major categories used for "classifier" classification: supervised and unsupervised classification (Ocelíková and Krištof, 2001; Vúrostková et al., 2008). Supervised classification is used when a training sample is used to train the classifier. Supervised classification is mostly used for data of landmarks of a specific area taken from satellite imagers that are then stored in a database. The statistical analysis of the spectral reflectance of each ROI of the landmark defines the spectral signature for the different regions of interest. Once a statistical characterization has been achieved for each feature, the cloud image is then classified by examining the reflectance for each pixel and making a decision about the cloud class of each pixel. The training areas should be fully representative of the variations of the regions of interest within an image. Numerous different factors such as soil type, vegetation, water or ice can affect the signature and the accuracy of the final map (Amato et al., 2008; Anthis and Cracknell, 2004; Calbó and Sabburg, 2008; Jedlovec, 2009). Unsupervised classification is an image processing technique that divides the pixels of a cloud image into a number of classes based on the features of the image. Since it does not require a training set, it is a very fast classifying technique. The basic idea is that each pixel is compared to each discrete cluster to see which one it is closest to. Values within a given cover type should be close together in the measurement space whereas data in different classes should be comparatively well separated (Heinle et al., 2010; Liu et al., 2011; Orsini et al., 2002). Unsupervised learning can be applied to artificial intelligence classifiers as well, not only simple and statistical classifiers (Becker, 1991; Christodoulou et al., 2003; Tian et al., 1999).

It has to be mentioned that depending on the architecture of the classifier and the measuring instruments, in some cases, especially for ground based VIS cameras, the feature boundaries between different cloud classes are not distinct and one class may infiltrate another class. In these occasions, the classifier has to classify nearby pixel/data in the same class even though one of them may have been originally classified within a different cloud class. For example, it is of no need to know that a single pixel may belong to class "A" when all the neighboring pixels certainly belong to class "B". Of course, a good classifier should be able to recognize the simultaneous occurrence of different cloud types at the same location of the image that due to their different height and to the angle of observation might appear as one cloud (Baum et al., 1997; Hahn et al., 1982; Wang and Dessler, 2006).

4.2.1. Simple classifiers

We have grouped as Simple Classifiers the algorithms that use linear mathematical relations to process cloud features and classify regions of interest into different classes. Their major advantage is that the equations are simple, resulting in simple algorithm architecture and demand low computational power, but this reflects to longer computational time and lower accuracy for multi-feature classification. The features for the classification are extracted after the distinction of clouds from sky/land (Heinle et al., 2010), although in some classifiers, the distinguishing and classifying steps are processed simultaneously (Duchon and O'Malley, 1999).

The minimum distance classifier is the simplest classification algorithm. For each class, the mean of the features is calculated and then, for each pixel in the image, the algorithm calculates the distance of the pixel's input from the class means. The pixel is assigned to the class with the min-

imum distance from its mean. It is a fast classifier, yet the accuracy is low (Richards and Jia, 1999).

The parallelepiped classification (or threshold-based classification) uses an upper and a lower threshold for different features for the classification process. It is a rule-based classification method (Wang and Sassen, 2001), where the decision parameters form an n-dimensional data space (where the limits of the n-dimensions data are confined by the standard deviation about the mean of the features for each selected class). Thus, in the case of a one-dimensional space of parameters, the partition associated with a certain class will be a line segment. In a two-dimensional space, the partition will be a rectangle (Orsini et al., 2002; Souza-Echer et al., 2006), in the three-dimensional space the partition will be a parallelepiped, and so on (Calbó and Sabburg, 2008; Liu et al., 2011). A single dimension parameter threshold may be used but the results will have low accuracy (Kegelmeyer, 1994). Each pixel is classified as belonging to a cloud class in a region whose attributes are within predefined ranges between the upper and lower boundaries of each attribute. It is not necessary for a pixel to rest within the boundaries of all n-dimension feature data of each cloud class, but that it rests within the boundaries of a greater number of features than when compared with the other cloud classes (Anthis and Cracknell, 2004; Duchon and O'Malley, 1999). Fig. 9 presents an illustration of a 2D classification, where A–E represent different cloud classes.

The k-nearest neighbor (k-nn) algorithm is a machine learning technique used for classifying regions of interest into a preselected set of classes. It is used mainly when there is little or no prior knowledge about the distribution of the data. Each ROI is classified based on the closest regions of interest to it, within a specific area defined by the user (Bankert and Aha, 1996; Bankert and Wade, 2007). It is different from the parallelepiped classification as the ROI to be classified does not have to lie between the n-dimension boundaries of a class, but has to be as close as possible to the cloud class attributes. Based on the preprocessed features, each ROI is classified to the most common class amongst its k nearest neighboring regions of interest (k is a positive integer, typically small) (Tag et al., 2000). The Euclidean distance is mostly used for the calculation of the distance of the ROI input data from the specific class attributes (Christodoulou et al., 2003). It is one of the simplest machine learning classifiers since the target function used is approximated locally (within a small region) and each ROI is classified by the majority vote of the neighbor regions of interest (Buch et al., 1995; Heinle et al., 2010). The significance of the neighboring regions of interest is weighted based on their distance from the ROI under consideration; i.e. in a 2-nn algorithm the adjacent regions of interest (distance = 1) are more significant than the regions of interest after the adjacent (distance = 2). The k-nn algorithm begins with an initial clustering of the data as a starting state; k randomly selected regions of interest (prototypes) are selected from the data space to be clustered. Each unclassified point is assigned to a class based on the k nearest point by using the data distance and the target function. In most classifiers, the influence of the neighboring regions of interest is weighted by linear interpolation so that the nearest regions of interest affect the ROI to a greater effect than the more distant ones (Gao et al., 2010; Mills, 2011).

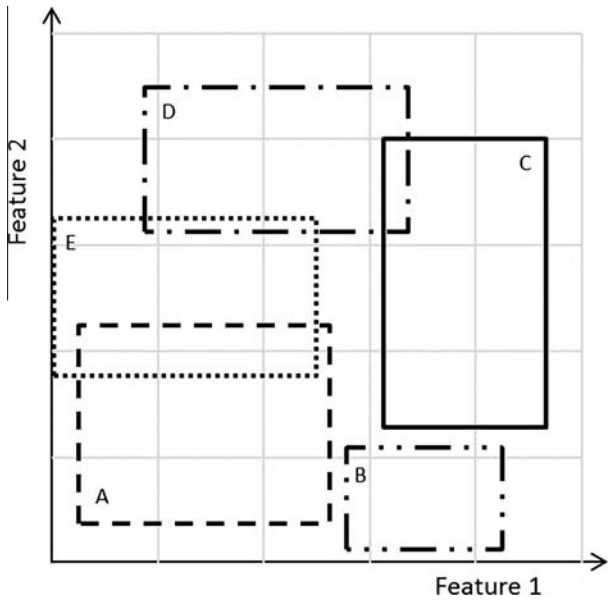

Fig. 9. An example of a 2D parallelepiped classification. A–E Represent different cloud classes based on Duchon and O'Malley (1999) and Calbó and Sabburg (2008).

4.2.2. Statistical classifiers

We have grouped as statistical classifiers the classifiers that are generally probabilistic models, which do not actually classify the regions of interest but provide the probability of a ROI to belong to a specific class. They use more complex equations than the simple classifiers that lead to more accurate results, yet, this results in more sophisticated algorithms that demand more computational power. The design and structure of the classifiers are based on statistical formulas providing the user the ability to interfere with the data collection and the features extraction (Fukunaga, 1999; Michie et al., 1994).

The k-means method is similar to the k-nn method, and is based on the analysis of the means of the neighboring regions of interest. It begins with an initial clustering of the data as a starting state; initially k regions of interest are selected from the data space to be clustered. The initially selected regions of interest are either randomly selected or determined by computing the local maxima of the data set, by considering that the initial clusters are centered at these maxima (Ameur et al., 2004; Massons et al., 1996). Each unclassified point is assigned to a class based on the minimum distance from the centroid by minimizing the sum of the squares of the distances between data and the corresponding cluster centroids. The means of the k ini-

tial clusters are computed and these cluster centers become the new prototypes. Each ROI of the dataset is reexamined and if it is closer to the mean of another cluster than to the mean of its current cluster, the ROI is transferred to the closest class and the cluster means are recalculated. This procedure continues until the process converges (Cheruy and Aires, 2009; Col and Mouchot, 1995).

The Bayesian (or Bayes) classifier is a probabilistic classifier based on the Naïve Bayes assumption that considers that all the input features are conditionally cloud class independent, even though this is usually false (since features are usually dependent) (Merchant et al., 2005; Murtagh et al., 2003). The target function is computed from the conditional probability that a ROI belongs to a cloud class given the probabilities of the selected (independent) features. The classification decision is made by selecting the maximum conditional probability (Yang, 2010). Bayes classifiers may be supervised or unsupervised, depending on the application and the features used (Wang et al., 2004). The major advantage of this classifier is the small amount of training data required for the estimation of the parameters of the classification and the simplicity of the algorithm. Furthermore, the independency of the features consumes less computational power. The main disadvantage is the naive assumption of the independence of the features, especially in cloud classification (Flach and Lachiche, 2004).

The Maximum Likelihood Classification is a probabilistic statistical classifier that classifies a ROI to the class that has the highest (maximum) probability (Li et al., 2003). This method assumes that the statistical distribution of the features for each class is normal or Gaussian, and calculates the probability that a given ROI belongs to a specific class (Pagès et al., 2003; Parikh and Ball, 1980). The features of the image may have a predefined weight in the probability function. Then, the pixels are assigned to the selected class. This method may be supervised or unsupervised, depending on the structure of the algorithm and the available data (Azimi-Sadjadi et al., 2001b; Tian et al., 2000).

Linear Discriminant Analysis (LDA) also known as Fisher Discriminant Analysis is a supervised statistical technique used to combine different cloud features into a linear combination for classification purposes. LDA simulates the differences between the cloud classes of data by distinguishing independent features from dependent features of the input data (Amato et al. (2008)). In cloud classification, the dependent feature is the cloud class and the independent features are the data space. In LDA a linear combination of the features define the function that separates the cloud classes; the number of the features used, define the dimensions of the separation hyper-plane boundary (Yang, 2010). Quadratic Discriminant Analysis (QDA) is an advanced implementation of LDA for classifying regions of interest in the quadric space (4D). It provides a more accurate threshold boundary than LDA and can be used for multi-feature input data for the classification (Amato et al., 2008; Shi et al., 2007). Heteroscedastic Discriminant Analysis (HAD) is a model based generalization of LDA technique, proposed by Marais et al. (2011) to be used for satellite imagers for the visual and near infrared bands. The method combines the three visual bands (RGB) and the NIR band into one gray-scale image which is used for the linear classification.

The Unit-Feature Spatial Classification Method (UFSCM) is a supervised Machine Learning technique that can be performed for multi-spectral input data, mainly from satellites. The input spectrum is divided into a genus matrix, which comprises the Unit Feature Spaces (UFSs), which ultimately represent the selected features. Each point in the multidimensional data space is classified into a corresponding UFS and once the cloud type of a single UFS has been determined, the corresponding pixels in any sample are also classified (Zhang et al., 2011).

Principal Component Analysis (PCA) is a preprocessing statistical technique that has the ability to identify the principal "features" or components, which implicitly represent all the features of a cloud class by developing a smaller number of artificial features (Bajwa et al., 2009; Liu et al., 2009). PCA identifies the principal features of the image under investigation, so as to simplify the calculations and the principal features are given different weights for the classification based on their estimated relevant importance. The algorithm extracts the attributes from the cloud images based on the selected features and compares the principal features of the acquired cloud image with the training set. Thus, the cloud type can then be classified. Since the selected features can principally differentiate among various input data, PCA can be supervised or unsupervised depending on the technique architecture (Amato et al., 2008; Ameur et al., 2004; Bajwa and Hyder, 2005).

4.2.3. Artificial intelligence classifiers

Artificial Intelligence (AI) classifiers is a term used for one type of machine based algorithms that can be used in cloud classification. These algorithms classify regions of interest using a methodology that performs similar functions as the human brain, such as understanding, learning, solving problems and taking decisions. AI consists of Artificial Neural Networks (ANNs), fuzzy logic, Expert Systems, etc. (Mellit and Kalogirou, 2008; Paliwal and Kumar, 2009). ANN is a collection of small individually units interconnected between them, that mimic the dendritic form of the biological neural network that receives signals from the neighboring neurons (receptors), process the signal to the main cell and transmit signals through the nerves. ANN architecture consists of three stages. The first layer is called the input layer and the number of its perceptrons is determined by the input parameters and their codification (pattern or prototype). The last layer is called the output layer, and the number of its perceptrons is given by the desired output. The second layer is the hidden layer that processes the data. The hidden layer can extend over multiple layers, depending on the structure of

the ANN. In general, depending on the application different possibilities should be investigated. In most ANN, hidden layers use non-linear functions for processing the data, while input/output layers use linear or non-linear functions (Lafont et al., 2006). The architecture of Neural Networks depends on the interconnections between the layers; recurrent neural networks (RNNs) are ANN where the connections between the neurons form are circled, and feed-forward neural networks are ANN where the connections between the neurons move only in the forward direction. The main advantage of AI classifiers over simple/statistical classifiers is that once the classifier is trained, they perform at very fast processing time, involving less computational effort. Furthermore, the knowledge of internal system parameters is not required and can be used for multi-feature classification since unlike simple/statistical classifiers, they can approximate any non-linear mathematical function. The disadvantages are that there is no filtering of the input data and they can be applied only at the location they are designed for, both resulting to unpredictable execution and unreliable results (Egmont-Petersen et al., 2002; Mellit and Kalogirou, 2008; Paliwal and Kumar, 2009).

ANN can be used in cloud classification for almost every instrument used by researchers for the detection of clouds. Using the appropriate technique depending on the equipment used, the classifier first extracts the features of the clouds and then these features are used as the input layer of the ANN. The weight of each feature is associated to the value of the feature before entering the next layer. Subsequently, for multilayer ANN, the output of one layer may be weighted before entering the next layer. The processing of the information, the number of layers and the architecture depend on the specific ANN used for the classification. In most ANN, the classification is supervised, i.e. depends on a training set. The dataset used for classification, is compared to the training set, based on the features of the cloud, and the algorithm decides the class of the cloud. Since there is a training set, the distinction of clouds from sky/land is processed simultaneously with the classification. There are numerous ANN models, but in this section we presented only the ANN that have been used for cloud classification.

Back Propagation Neural Network (BPNN) is a feed-forward multilayer perceptron neural network that can also be used to train other neural networks. It has two stages; the propagation and the weight update. The first step of the propagation is the forward pass which involves presenting a sample input to the network and letting activations flow until they generate the propagation's output activations. The second step is the backward pass where the neural network's output activations are compared with the target output and compute the error estimates for the output units. BPNN is based upon empirical risk minimization i.e. during the weight update stage, the weights connected to the output units are adjusted, in order to reduce the errors of stage one and consequently, estimate errors for the units in the hidden layers. Finally, errors are propagated back to the connections stemming from the input units (Cazorla et al., 2008a; Liu et al., 2009; Richards and Sullivan, 1992).

The Multi Layer Perceptron (MLP) model is a feed-forward artificial neural network classifier that maps various sets of input data into a set of appropriate output. The topology of the MLP requires the determination of the number of layers and the number of perceptrons per layer. The connections between perceptrons in an MLP are forward and every perceptron is connected to all the perceptrons in the next layer except the output layer that directly gives the result. Every layer weights the results of the previous layers that are connected to it, sums the results and compares the result to a threshold. Depending on the result of the comparison, a non-linear function in most cases is applied to the data and the result is used as input to the next layer up to the output layer. MLP utilizes Back Propagation for training the network (Cazorla et al., 2008a; Macías et al., 2001; Mellit and Kalogirou, 2008).

Probabilistic neural networks (PNNs) are supervised forward feed networks that estimate the probability function of the input data to belong to a cloud class based on the samples of the training set. The hidden layer consists of the Pattern layer and the Summation layer. The Pattern layer compares the data input to the training set and computes the Gaussian distance of each feature to the corresponding feature of a selected sample from the training set. The Summation layer computes the probability of the input layer to belong to the training sample. The target function is the sum of the features, weighted by their distance as computed at the Pattern layer. Finally, the output layer defines the transfer function of the cloud class as the target function with the maximum value (Azimi-Sadjadi et al., 2001a, 2001b; Bankert, 1994; Bankert and Aha, 1996; Liu et al., 2009; Saitwal, 2006; Tian et al., 1999, 2000; Wang et al., 2004).

Self-Organizing Map (SOM) is the only Neural Network classifier that uses an unsupervised learning algorithm in order to reduce the dimensions of the data into a two-dimensional map that can visually represent the data space of the training samples. The model was first described as an artificial neural network by the Finnish professor Kohonen (1982), and is sometimes called a Kohonen map (Ambroise et al., 2000; Tian et al., 1999). The SOM operates in two stages. The first step is the training, where the map is constructed. The components of the map are called nodes or neurons and represent the weighted features of the data input. The weights are adapted without supervision in such a way, so that the density distribution of the input data is preserved and represented on the output nodes. The second step is the mapping where the algorithm classifies the image based on the training map (Christodoulou et al., 2001, 2003; Liu et al. 2009; Macías et al., 2001). Ambroise et al. (2000) proposed a technique that combined a classic probabilistic SOM with agglomerative hierarchical clustering in order to achieve the clustering of different clouds in a

mega-pixel image from the Meteosat satellite. Since the agglomerative hierarchical clustering can be used for much smaller data (kilo pixels), the SOM is used to constrain the input dataset into the appropriate size to be used in the clustering algorithm.

A Support Vector Machine (SVM) is a concept encompassing several supervised techniques that represent a multidimensional input into a 2D map. The classification is performed by constructing an N-dimensional hyperplane that optimally separates the data into two categories. The SVM embodies structural risk minimization which is achieved by selecting the best borderline for classifying the pixels in an image. The SVM training algorithm finds out the best borderline in order to maximize the margin of the separation line between the different cloud pixels, defined as a symmetric zone centered on the frontier with no training points included, and to minimize the number of wrong classification occurrences. SVM models are similar to the two layer perceptron neural networks (Azimi-Sadjadi and Zekavat, 2000; Lee et al., 2004; Liu et al., 2009; Mills, 2011).

A different approach to AI classifiers is the fuzzy logic classifier. The fuzzy logic classifier is a supervised learning approach that uses fuzzy logic during the construction of the training set (Baum et al., 1997; Key et al., 1989). The fuzzy logic is the ability of an algorithm to make decisions not based just on true of false, but depending on the input data, within the range of zero to one. The fuzzy logic is used to weight the dependence of a cloud type to a selected feature and optimized the classification using the adaptable values of the input features (Col and Mouchot, 1995; Ghosh et al., 2006; Mellit and Kalogirou, 2008).

4.3. Cloud base height calculation

The height of a cloud in the atmospheric column, defined as the Cloud Base Height (CBH) is a key parameter in the characterization of clouds (Hirsch et al., 2011), since its estimation limits the number of the potential cloud classes that a classifier or detection algorithm has to compare with, and thus maximizing the efficiency of the classification algorithm. There are several techniques used to estimate CBH and depend on the equipment being used.

A comparison of the ground based techniques for calculating CBH using the Nubiscope, WSI, Ceilometer and Radar equipment was presented by Feister et al. (2010) and by Hirsch et al. (2011) for CBH calculating using an RGB camera, Electron Multiplying Charge Coupled Devices (EMCCDs) and IR camera equipment. Furthermore, Seiz et al. (2002) compared six different ground based instruments for cloud base height measurements: visual observation, radiosonde, Ceilometer, Doppler LIDAR, Radar and stereoscopic cameras.

For satellite imagery, CBH is very difficult to be computed, since even though the CTH is very easy to compute, CBH can only be estimated (Forsythe et al., 2000), taking into consideration that low clouds are geometrically thinner than high clouds and that high clouds are much more heterogeneous (Stubenrauch et al., 2008). CBH is computed based on the effective brightness temperature of the image which is matched to the pressure height of the water vapor of clouds, using empirical height assignment techniques (Deb et al., 2008) as shown in Fig. 10 (Hutchison et al., 2006). The pressure of a cloud can be correlated to its vertical height, since pressure decreases at higher levels of the atmosphere. This correlation is estimated using a relation of the measured irradiance and empirical weights of the brightness temperature for clear and homogeneous single cloud irradiance at the different sky heights (Stubenrauch et al., 2008). As presented in Section 2, clouds are divided in three categories based on their height: low, middle and high clouds. Thus, the estimation of CBH limits the classification of a cloud in the three or four classes of the particular height level (Allmen and Kegelmeyer, 1996; Campbell and Holmlund, 2004; Janeiro et al., 2010). A very detailed presentation of the estimation method of cloud height, using the IR and IR/WV channels of Meteosat-7 and Kaplana-1 was presented by (Giri and Sharma, 2011; Li et al., 2008).

For ground based equipment, CBH is derived either by using an IR camera/pyranomenter (Feister et al., 2010; Forsythe et al., 2000) or by analyzing the vertical profiles of backscattered laser signal using a radar (Martucci et al., 2010). For the IR measurements, the cloud base temperature (or the temperature of each layer of clouds) is correlated to the CBH using an empirical statistical relation, taking into account the dependency of the cloud temperature on the zenith angle (Feister et al., 2010). Nowak

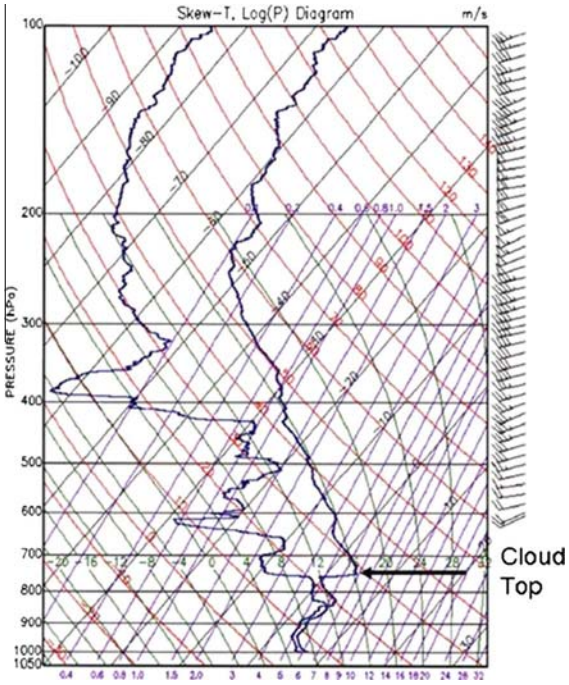

Fig. 10. A thermodynamic diagram presenting the correlation of cloud pressure to effective brightness temperature constructed from data collected by a radiosonde (Hutchison et al., 2006).

et al. (2008) presented a CBH measuring technique utilizing the complementing properties of a ceilometer and a cloud radar. Ceilometers detect clouds and estimate CBH, while radars detect CTH. With this technique, the measurements provide the 3D structure of the clouds.

A different approach was presented by several researchers who estimated CBH by triangulation from stereo photography using two ground based cameras as shown in Fig. 11 (Janeiro et al., 2010). The basis of this method is formed by the overlapping (common) area of two adjusted images. The overlapping area is analyzed by statistical analysis of the images (Allmen and Kegelmeyer, 1996; Janeiro et al., 2010; Kassianov et al., 2005; Seiz et al., 2007).

Finally, a third method relies on using radiosondes, where the estimation of the CBH is derived instantaneously during the uplift of the balloon (Chernykh and Eskridge, 1996; Hutchison et al., 2006). The detection of the base and top of the clouds is based on the Relative Humidity (RH). Zhang et al. (2010) proposed the following thresholds for the presence of moist layers and clouds based on RH: A moist layer (not necessarily a cloud) is determined when the minimum RH of the layer is above 84% and there is at least 3% difference in RH during the transition from the sky below the layer to the base of the layer and from the top of the layer to the sky above. If the maximum RH is above 87%, then the moist layer is considered to be a cloud. A similar approach, but with different thresholds was proposed by Minnis et al. (2005), and based on their results, by Jin et al. (2007) for clouds over the arctic sea. Chernykh and Eskridge (1996) and Chernykh et al. (2009) proposed a different method for the detection of clouds using radiosondes. In their method, the presence of a cloud was indicated at the point where the second derivative of at least one of the measured temperature and RH was zero.

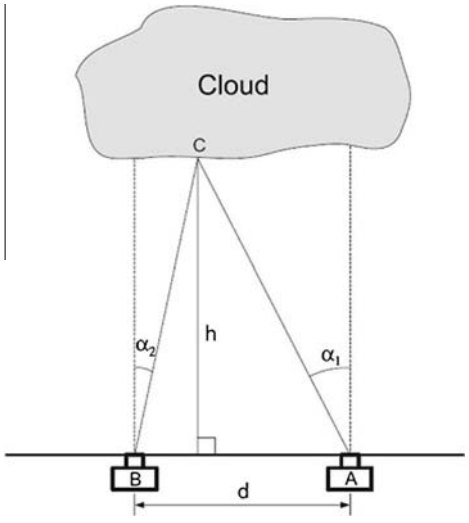

Fig. 11. Triangulation method used to measure CBH (Janeiro et al., 2010).

4.4. Experimental results

Table 3 presents the experimental results of the researchers that have conducted research on cloud classification. The columns of the table represent: (1) the instrument used to observe the clouds and if satellite based, the name of the satellite/imager, (2) the distinguisher/classifier, (3) the published date of the paper, (4) the location of the measurement equipment or of the satellite view, (5) the overall accuracy (given as the average accuracy of the method for all classes under consideration, either given by the researcher or calculated by us), (6) the best accuracy obtained (accuracy is the ratio of correctly classified records over the total number of records) and the specific class (i.e. cloud type, sky, land, sea, fog, contrails) it was obtained for, (7) the least accuracy and the specific class, (8) the number of cloud classes used for cloud classification (several researchers use less than ten classes as defined by WMO for classification purposes) and (9) the author name and year of publication.

The data in the table is grouped based primarily on the instrument used and secondary on the publication year of the paper, so as to be easier for the reader to compare progress in the obtained results of the researchers.

The overall, best and least accuracy of the results presented in Table 3 is a comparison of the cloud classification of the algorithm and the visual classification performed either by an expert meteorologist or by the researchers. This comparison was presented by the researchers as a confusion matrix. The confusion matrix is a visualization of the predicted and actual classification (Kohavi and Provost, 1998). The form of a 4-class confusion matrix is presented in Table 4. The columns of the matrix represent the occurrences in the predicted class from the classifier, while the rows represent the actual class, as defined visually by the expert meteorologist. The accuracy of the classification is computed as the ratio of the sum of the primary diagonal (true occurrences: A1, B2, C3 and D4) over the sum of all the occurrences (true and false, A1 to D4). For example, the accuracy of a classifier to distinguish low clouds is B2 over (B1 + B2 + B3 + B4). The same principles applies for any number of classes used by the researchers, ranging from a 2-class to a 15-class confusion matrix. However, some researchers prefer to use the percentage accuracy for each class rather than the occurrences, for faster evaluation of the results.

Unfortunately, a rational comparison of the data and accuracies presented in Table 3 cannot be performed, not only due to the differences in the equipment and the classification techniques used by the researchers, which could be comparable, but due to the parameters used and assumptions made by the researchers. First of all, the accuracy of the method resulted by the visual comparison was performed either by the researchers or by an expert meteorologist. Thus, the accuracy presented is subjective to the human factor. Moreover, each researcher used a different sample of pictures for the comparison, ranging from tenths

Table 3
Experimental results by researchers on cloud classification.

Instrument	Distinguisher/classifier	Publish	Location	Overall accuracy	Best accuracy	Least accuracy	Classes	Ref.
Pyranometer	Parallelepiped	1999	Oklahoma, USA	45%	89% Clear sky	6% Fog	7	Duchon and O'Malley (1999)
Pyrradiometer	Parallelepiped	2002	Antarctica	45%	94% Ci	33% Cs	3	Orsini et al. (2002)
Pyranometer	Maximum Likelihood	2003	Iberian Peninsula	73%	83.5% Clear sky	47% Broken or scattered clouds	4	Pagès et al. (2003)
Pyranometer	Maximum Likelihood	2001	Catalonia, Spain	57.5%	82.4% Clear sky	10.9% Overcast high clouds	5	Boers et al. (2000)
All sky camera	Parallelepiped	2003	New Zealand	65.9%	–	–	3	Pfister et al. (2003)
IR Pyrometer	Parallelepiped	2001	Belgium	85%	92% Homogeneous	65% Broken clouds	3	Gillotay et al. (2001)
Ground Based Camera	Bayesian classifier	1992	England	97.5%.	97.7% Cloud	97.3% Clear sky	2	Richards and Sullivan (1992)
Ground Based camera	k-nn Classifier	2005	UK	60.1%	83.3% Cb	31.2% Clear sky	5	Singh and Glennen (2005)
Ground Based Camera	Back propagation	2005	UK	60.6%	–	–	5	Singh and Glennen (2005)
Ground Based Camera	Principal component analysis	2005	World-wide	92.3%	100% Clear sky	86.2% High level clouds	4	Bajwa and Hyder (2005)
Ground Based Camera	Parallelepiped	2006	Antarctic Peninsula, Brazil	94% Clear	–	–	3	Souza-Echer et al. (2006)
Ground Based Camera	Principal component analysis	2009	World-wide	89%	100% Clear sky	86% Multilayer class	3	Bajwa et al. (2009)
All sky camera	Multilayer perceptron back propagation	2008	Granada, Spain	78.09%	88.11%	61.41% Thin clouds	3	Cazorla et al. (2008b)
All sky camera	k-nn Classifier GLCM	2009	Moving vehicle from Germany to South Africa	97.06%	98.8% Clear sky	94.34% St – As	7	Heinle et al. (2010)
All sky camera	Supervised parallelepiped (9D)	2008	Toowoomba, Australia	69%	100% Clear sky	10% Class D	8	Calbó and Sabburg (2008)
All sky camera Whole sky imager	Supervised parallelepiped (9D)	2008	Toowoomba, Australia Girona, Spain	76%	83% Clear sky	6% Class K	5	Calbó and Sabburg (2008)
Whole sky imager	k-nn Classifier	1995	New Mexico USA	61%	98% Clear sky	35% Ci	5	Buch et al. (1995)
Whole sky imager	Supervised parallelepiped (9D)	2008	Girona, Spain	54%	58.5 Clear sky	0% Class K	8	Calbó and Sabburg (2008)
WSIRCMS	Parallelepiped	2011	Nanjing, China	90.97%	93.33% Cu/Cb	90.2% Ci	4	Liu et al. (2011)
NOAA-1 AVHRR SMS-1	Maximum Likelihood	1977	–	96.3%	100% Ci	95.8% Cb	4	Parikh (1977) and Parikh (1978)
NOAA's AVHRR	Probalistic neural network	1994	–	77.1%	97.3% Clear sky	65.3% Cs	10	Bankert (1994)
NOAA's AVHRR	Probalistic neural network	1994	–	91.2%	98.6% Clear sky	70.1% As	5	Bankert (1994)
NOAA's AVHRR	Probalistic neural network	1996	–	86.8%	96.8% Clear sky	74.7% Cs	10	Bankert and Aha (1996)
NOAA-11,12 AVHRR	Bayesian classifier GLCM	1995	New Zealand	68.32%	100% Cb	41.12% Ac	8	Uddstrom and Warreb (1996)
NOAA-11 AVHRR	Fuzzy logic classifier (equatorial air mass over land)	1997	World-Wide	86.2%	94.6% Clear sky	74.4% Uniform high	8	Baum et al. (1997)
NOAA-11 AVHRR	Fuzzy logic classifier (maritime tropical air mass over land)	1997	World-Wide	85.6%	99.6% Clear sky	72.9% Broken high	8	Baum et al. (1997)

NOAA-11 AVHRR	Fuzzy logic classifier (continental tropical air mass over land)	1997	World-Wide	87.4%	97% Thick uniform high	80.8% Broken high class	8	Baum et al. (1997)
NOAA-11 AVHRR	Fuzzy logic classifier (maritime tropical/ equatorial air mass over water)	1997	World-Wide	88.6%	98% Clear sky	73.4%) for broken high class	8	Baum et al. (1997)
NOAA-11 AVHRR	Fuzzy logic classifier (marine polar air mass over land or water)	1997	World-Wide	88.6%	95.8% Clear sky	77%) Uniform mid	8	Baum et al. (1997)
NOAA-11 AVHRR	Fuzzy logic classifier (continental polar air mass over land)	1997	World-Wide	91.1%	99.4% Clear sky	80.4%) Broken high	8	Baum et al. (1997)
NOAA-11 AVHRR	Artificial neural network	2006	Pacific ocean	77.5%	97.7% Cu	63.8% Sc	6	Lafont et al. (2006)
NOAA-11 AVHRR	Artificial neural network	2006	Pacific ocean	79.4%	87.8% Low clouds	64.8% Middle clouds	3	Lafont et al. (2006)
NOAAs AVHRR	Fuzzy multidimensional parallelepiped	2005	Scandinavia	81.93%	93.5% Land	56% Snow	10	Dybbroe et al. (2005a, 2005b)
NOAA-14 AVHRR	Artificial neural network	1997	United States	82.4%	88% Cb	56.5% St	8	Miller and Emery (1997)
NOAA-14 AVHRR	Bayesian classifier	2003	–	99.73%	–	–	2	Murtagh et al. (2003)
TIRO-N AVHRR	Multi-dimensional parallelepiped	1996	Gulf Stream region of Cape Hatteras	86%	–	–	2	Cayula and Cornillon (1996)
GOES-8	Self-organizing map	1999	USA	81.2%	97.1% Warm land	56.5% Cloud water	10	Tian et al. (1999)
GOES-8	Probalistic neural network	1999	USA	83.8%	97.3% Warm land	66.2% As	10	Tian et al. (1999)
GOES-8	Probalistic neural network maximum likelihood	2000	USA	75.4%	84.2% Warm land	45.4% As	10	Tian et al. (2000)
GOES-8	Probalistic neural network maximum likelihood	2001	USA	82.67%	–	–	10	Azimi-Sadjadi et al. (2001b)
GOES-8	Support vector machine	2000	USA	78.5%	100% Warm water	0% Cold water	10	Azimi-Sadjadi and Zevakat (2000)
GOES-8	Probalistic neural network	2001	Eastern USA	85.1%	91.9% Water	83.0% Low level clouds	5	Azimi-Sadjadi et al. (2001a)
GOES 8	Probalistic neural network	2003	Midwest – Eastern USA	88%	98% Low level clouds	80% Middle level clouds	5	Saitwal (2006)
GOES-10, GOES-12	k-nn Classifier	2007	West USA	>77%	>77%	>77% Cc	15	Bankert and Wade (2007)
GOES-12	Bispectral composite threshold	2008	USA	87.6%	–	–	3	Jedlovec and Haines (2008)
FY-2C	Parallelepiped classifier	2008	China	88.89%	–	–	2	Li et al. (2008)
FY-2C	Self-organizing map	2009	Asia, Australia, Pacific Ocean	94.26%	99.01% Sea	88.79% Thick Ci	4	(Liu et al. (2009)
FY-2C	Unit-feature spatial classification method	2011	Asia	81.4%	86% Clear sky	72.2% Cb	8	Zhang et al. (2011)
FY-2C	Unit-feature spatial classification method (3D)	2011	Asia	83.6%	86.9% Clear sky	78.9% Tk–Ci	8	Zhang et al. (2011)
SMS-1	Maximum Likelihood	1980	–	–	–	–	5	Parikh and Ball (1980)
METEOSAT	Self-organizing map with agglomerative hierarchical clustering	2000	Atlantic Ocean	71.8%	98% High thick	59% Thin Ci	9	Ambroise et al. (2000)
METEOSAT	Multilayer perceptron	2001	Iberian Peninsula	92.25%	100% Various classes	67.5% Clouds with vertical growth	6	Macías et al. (2001)
METEOSAT	Self-organizing map	2001	Iberian Peninsula	90.9%	100% Various classes	66.7% Middle clouds	6	Macías et al. (2001)

(*continued on next page*)

Table 3 (*continued*)

Instrument	Distinguisher/classifier	Publish	Location	Overall accuracy	Best accuracy	Least accuracy	Classes	Ref.
METEOSAT 5	Supervised parallelepiped	2004	Greece	60%	94% Middle or high clouds with light precipitation	0% Low cloud – no rain	9	Anthis and Cracknell (2004)
METEOSAT 7	Self-organizing map	2001	Mediterranean Sea	75.6%	92.3% CB	60.3% Clear sky	6	Crhristodoulou et al. (2001)
METEOSAT 7	Self-organizing map	2003	Mediterranean Sea	60.7%	57.1	–	6	Crhristodoulou et al. (2003)
METEOSAT 7	k-nn Classifier	2003	Mediterranean Sea	64.2%	82.4% St	45.2% Ci–Cu	6	Crhristodoulou et al. (2003)
METEOSAT-8	Principal component analysis linear discriminant analysis	2008	Mediterranean-Western Europe	92–97%	–	–	2 For different background	Amato et al. (2008)
MSG-SEVIRI	k-nn Classifier	2008	Africa, Europe	98.16%	100% Clear over sea	95% High clouds over land	8	Ricciardelli et al. (2008)
MSG-SEVIRI	k-nn Classifier	2010	Africa, Europe	96.5%	100% Various classes	89.5% Very thin clouds over land	14	Ricciardelli et al. (2010)
MSG-SEVIRI	k-nn Classifier	2010	Africa, Europe	97.1%	100% Various classes	91% High thin clouds over sea	8	Ricciardelli et al. (2010)
Landsat-5	Heteroscedastic discriminant analysis parallelepiped	2011	–	–	–	–	–	Marais et al. (2011)
MOS-1	Parallelepiped	1994	Japan	–	–	–	5	Tokuno and Tsuchiya (1994)
MODIS	Support vector machine	2004	Gulf of Mexico	88.5%	98% Water clouds	43.9% Clear sky	3	Lee et al. (2004)
Terra MISR	Support vector machines	2005	Molucca sea – Indonesia	78%	99.7% Land	58.5% Ice	8	Mazzoni et al. (2005)
Terra MISR	Support vector machines	2007	Molucca sea – Indonesia	78%	99.7% Land	58.5% Ice	8	Mazzoni et al. (2007)
Terra MISR Terra MODIS	Quadratic discriminant analysis	2007	Arctic region	94.5%	94.67% Ocean	94.43% Land	3	Shi et al. (2007)
GMS-4 DMSP-10 SSM/I	Parallelepiped	1995	Western Pacific Ocean	–	–	–	8	Liu et al. (1995)
GMS-5 MMCR TRMM TMI	Parallelepiped	2004	New Guinea	–	–	–	5	Hamada et al. (2004)
GMS-5 NOAA-AVHRR TERRA-MODIS	Back propagation	2005	Pacific Ocean	77.8%	97% Water	53% Cu	9	Shi et al. (2005)
Radiosondes	Statistical methods	1996	USA	90% for cloud level	–	–	10	Chernykh and Eskridge (1996)
SGP CART instruments	Parallelepiped	2001	USA	67%	100% Ns	37% Ac	9	Wang and Sassen (2001)

Table 4
An example of a four class confusion matrix.

		Predicted			
		Clear sky	Low clouds	Mid clouds	High clouds
Actual class	Clear sky	A1	A2	A3	A4
	Low clouds	B1	B2	B3	B4
	Mid clouds	C1	C2	C3	C4
	High clouds	D1	D2	D3	D4

(Richards and Sullivan, 1992) to tenths of thousands (Azimi-Sadjadi and Zekavat, 2000). Furthermore, each researcher classified clouds in a different number of classes, ranging from two classes representing clear or cloudy sky (Cayula and Cornillon, 1996; Richards and Sullivan, 1992; Li et al., 2008) to 15 classes including all the cloud classes, snow, land, etc. (Bankert and Wade, 2007). Nevertheless, the classification accuracy is subjective to the number of classes, since the accuracy is increased as two or more cloud classes are merged (Bankert, 1994; Calbó and Sabburg, 2008). Additionally, another parameter that affects accuracy is the location of the measurements, since even using the same equipment and classification algorithm, the accuracy varies for different regions and seasons (Baum et al., 1997). Actually, several researchers presented regionally specific results that cannot be used in other regions (Ho et al., 2003; Mahesh et al., 2001; Schneider et al., 1994; Shi et al., 2007). Finally, the availability, portability and cost of the equipment which correspond to the final use of the measurements prohibit the comparison of the provided accuracies.

5. Synopsis

In this paper, an extensive review of the instruments and algorithms related to cloud detection and classification is presented along with a table of the experimental results of the up-to-date research in the field of cloud classification.

The continuous development of technologies that use solar energy, leads to the need of accurate knowledge of the amount of the incident solar irradiance on the surface of the earth. Several researchers have proposed various models to calculate the solar irradiance based on various parameters. From these parameters, the most profound parameter for solar irradiance variations is cloudiness, because it is the only parameter that has a large impact and is not deterministic. The other parameters may be computed using the existing numerical forecasting methods. The influence of clouds on solar irradiance is due to reflection and absorption of the irradiance by cloud particles and depends strongly on the volume, shape, thickness and composition of the clouds. Thus, the knowledge of the presence of clouds in the sky and the type of the clouds is essential for the prediction of the performance of solar RES, with an ultimate goal of forecasting their power production.

There are various classification techniques used for cloud classification which were developed due to the different instruments used to estimate the state of the sky. The instruments used for the detection of clouds range from spectral cameras/imagers (at VIS, IR, UV or MW wavelengths) to solar irradiance sensors. These instruments can be ground-based, integrated on a satellite (imagers), or on a weather balloon. Ground equipment is mainly used to measure data for a specific location whereas satellites are measuring data over whole continents. Ground equipment has a small field of view reducing the ability of monitoring the formation of clouds and their movement over a large sky area. On the other hand, satellite imagers provide large-scale cloud information, but the provided data is in low resolution and may contain errors; small clouds are often overlooked due to the limited resolution and low or thin clouds and land are frequently confused because of their similar brightness temperature.

Some of the cloud classification techniques are universal and could be used regardless of the technology used whereas other techniques may be used exclusively for a particular methodology. Cloud classification is based on the various features of clouds that represent the designated cloud characteristics. The first step for cloud classification is the distinction of clouds from sky/land followed by the computation of the cloud cover fraction. The simplest method used is the linear threshold distinction where, depending on the measurements of the instrument, the "ROI" is classified as cloud or not cloud. The distinction may be achieved directly applying a threshold to the measurements or indirectly, by digitizing the measurements and then using image processing techniques on the digital image. The second step is the classification of clouds using the different features of the clouds, although some methodologies distinguish clouds from the sky/land and classify clouds simultaneously.

The distinction of clouds from sky/land can be performed using spectrum analysis, irradiance or other complex techniques. The spectrum analysis method can be applied for data from both ground-based equipment and satellite imagers. The VIS spectrum distinction is based on the different color of the clouds compared to sky/land. The IR distinction method identifies and classifies clouds based on their absorbed and emitted IR radiance by either comparing their brightness temperature or directly by using a threshold. The UV distinction method is based on the absorption of UV radiation by clouds. Distinction based on irradiance is derived from the time series of the irradiance, by measuring global, diffuse and direct (if necessary) irradiance.

As for the classification of clouds, the classifiers are divided in two categories: supervised and unsupervised classification. Supervised classification is used when a training sample is used to train the classifier while unsupervised classification is an image processing technique that divides the pixels of an image into a number of classes based on the features of the image. We have also divided the classifiers in three groups: simple, statistical and artificial intelligence classifiers. The simple group consists of simple, linear mathematic algorithms that demand low computational power. The statistical group consists of more complex algorithms, where a statistical model is used to classify the clouds and may involve a training sample. Finally, artificial intelligence classifiers classify regions of interest using a methodology that performs the similar functions as the human's brain, such as understanding, learning, solving problems and taking decisions.

Researchers with the above knowledge can proceed to utilize it for estimation of solar irradiance under cloudy skies for monitoring the performance of solar RES.

References

Ahmad, M.J., Tiwari, G.N., 2011. Solar radiation models – a review. International Journal of Energy Research 35, 271–290.

Ahrens, C.D., 2009. Meteorology Today – An Introduction to Weather, Climate and Environment, ninth ed. Pacific Grove, California, Brooks/Cole.

Alados-Arboledas, L., Alados, I., Foyo-Moreno, I., Olmo, F.J., Alcántara, A., 2003. The influence of clouds on surface UV erythemal irradiance. Atmospheric Research 66, 273–290.

Allmen, M.C., Kegelmeyer Jr., W.P., 1996. The computation of Cloud-Base Height from paired whole sky imaging cameras. Journal of Atmospheric and Oceanic Technology 13, 97–113.

Amato, U., Antoniadis, A., Cuomo, V., Cutillo, L., Franzese, M., Murino, L., Serio, C., 2008. Statistical cloud detection from SEVIRI multispectral images. Remote Sensing of Environment 112, 750–766.

Ambroise, C., Sèze, G., Badran, F., Thiria, S., 2000. Hierarchical clustering of self-organizing maps for cloud classification. Neurocomputing 30, 47–52.

American Meteorological Society, 2011. <http://www.ametsoc.org/>.

Ameur, Z., Ameur, S., Adane, A., Sauvageot, H., Bara, K., 2004. Cloud classification using the textural features of Meteosat images. International Journal of Remote Sensing 25, 4491–4503.

Aminou, D.M.A., 2002. MSG's SEVIRI Instrument. ESA Bulletin, vol. 111.

Angstrom, A., 1924. Solar and terrestrial radiation. Quarterly Journal of Royal Meteorological Society 50, 121–125.

Anthis, A.I., Cracknell, A.P., 2004. Cloud and precipitation classification for a depression system approaching the south Balkan Peninsula. A case study of 26 March 1998. International Journal of Remote Sensing 25, 4471–4490.

Anzalone, A., Isgrò, F., Tegolo, D., 2009. A study for cloud parameter retrieval from the IR cloud cameras of the AUGER observatory. Nuclear Physics B 190 (Proc. Suppl.), 278–283.

Azimi-Sadjadi, M.R., Zekavat, S.A., 2000. Cloud classification using support vector machines. In: Proceedings of the 2000 IEEE Geoscience and Remote Sensing Symposium, vol. 2, Honolulu, Hawaii, pp. 669–671.

Azimi-Sadjadi, M.R., Wang, J., Saitwa, K., Reinke, D., 2001a. A multichannel temporally adaptable system for continuous cloud classification from satellite imagery. In: Proceedings of International Joint Conference on Neural Networks, pp. 1625–1630.

Azimi-Sadjadi, M.R., Gao, W., VonderHaar, T.H., Reinke, D., 2001b. Temporal updating scheme for probabilistic neural network with application to satellite cloud classification – further results. IEEE Transaction of Neural Networks 12, 1196–1203.

Badescu, V., 1999. Correlations to estimate monthly mean daily solar global irradiation: application to Romania. Energy 24, 883–893.

Badescu, V., 2002. A new kind of cloudy sky model to compute instantaneous values of diffuse and global solar irradiance. Theoretical Applied Climatology 72, 127–136.

Bajwa, I.S., Hyder, S.I., 2005. PCA based classification of single layered cloud types. Market Forces 1, 3–13.

Bajwa, I.S., Naweed, M.S., Asif, M.N., Hyder, S.I., 2009. Feature based image classification by using principal component analysis. ICGST-GVIP Journal 9, 11–17.

Bakirci, K., 2009. Models of solar radiation with hours of bright sunshine: a review. Renewable and Sustainable Energy Reviews 13, 2580–2588.

Bankert, R.L., 1994. Cloud classification of AVHRR imagery in maritime regions using a probabilistic neural network. Journal of Applied Meteorology 33, 909–918.

Bankert, R.L., Aha, D., 1996. Improvement to a neural network cloud classifier. Journal of Applied Meteorology 35, 2036–2039.

Bankert, R.L., Wade, R.H., 2007. Optimization of an instance-based GOES cloud classification algorithm. Journal of Applied Meteorology and Climatology 46, 36–49.

Barbaro, S., Cannata, G., Coppolino, S., Leone, C., Sinagra, E., 1986. Correlation between relative sunshine and state of the sky. Solar Energy 26, 537–550.

Barlev, D., Vidu, R., Stroeve, P., 2011. Innovation in concentrated solar power. Solar Energy Materials & Solar Cells 95, 2703–2725.

Baum, B.A., Tovinkere, V., Titlow, J., Welch, R.M., 1997. Automated cloud classification of global AVHRR data using a fuzzy logic approach. Journal of Applied Meteorology 36, 1519–1540.

Becker, S., 1991. Unsupervised learning procedures for neural networks. The International Journal of Neural Networks 1&2, 17–33.

Berger, L., Besnard, T., Genkova, I., Gillotay, D., Long, C.N., Zanghi, F., Deslondes, J.P., Perdereau, G., 2005. Image comparison from two cloud cover sensor in infrared and visible spectral regions. In: Proceedings of the 21st International Conference on Interactive Information Processing Systems (IIPS) for Meteorology, Oceanography, and Hydrology.

Biday, S., Bhosle, U., 2010. Relative radiometric correction of cloudy multitemporal satellite imagery. International Journal of Civil and Environmental Engineering 2, 138–142.

Black, K., Tooman, T., 2005. Whole-Sky Imager (WSI) Handbook. ARM TR-043, U.S. Department of Energy.

Boers, R., Van Lammeren, A., Feut, A., 2000. Accuracy of cloud optical depth retrievals from ground-based pyranometers. Journal of Atmospheric and Oceanic Technology 17, 916–927.

Boers, R., de Haij, M.J., Wauben, W.M.F., Baltink, H.K., van Ulft, L.H., Savenije, M., Long, C.N., 2010. Optimized fractional cloudiness determination from five ground based remote sensing techniques. Journal of Geophysical Research 115, D241161–D2411616.

Bonomo, F., Brignoli, V., 1998. Correlation between cloud frequency esteemed from Meteosat images at ground level <http://www.solar-thermalpower.it/documenti/1998%2001%2027%20Correlation%20between%20cloud%20frequency%20and%20transmittance%20measured%20-%20Bonomo%20Brignoli%20ISES%20Int%201998%20Harare.pdf>.

Borengasser, M., Hungate, W.S., Walkins, R., 2008. Hyperspectral Remote Sensing Principles and Applications. CRC Press, Taylor & Francis Group.

Brocard, E., Schneebeli, M., Mätzler, C., 2009. Deriving winds at Cloud-Base Height with an infrared camera. IEEE Transactions on Geoscience and Remote Sensing 47, 3319–3325.

Brocard, E., Schneebeli, M., Mätzler, C., 2011. Detection of cirrus clouds using infrared radiometry. IEEE Transactions on Geoscience and Remote Sensing 49, 595–602.

Brown, J.E.M., 2006. An analysis of the performance of hybrid infrared and microwave satellite precipitation algorithms over India and adjacent regions. Remote Sensing of Environment 101, 63–81.

Buch Jr., K.A., Sun, C.H., Thorne, L.R., 1995. Cloud classification using whole-sky imager data. In: Proceedings of the Fifth Atmospheric Radiation Measurement (ARM) Science Team Meeting, pp. 35–39.

Cahalan, R.F., Oreopoulos, L., Wen, G., Marshak, A., Tsay, S.C., DeFelice, T., 2001. Cloud characterization and clear-sky correction from Landsat-7. Remote Sensing of Environment 78, 83–98.

Calbó, J., Sabburg, J., 2008. Feature extraction from whole-sky ground-based images for cloud-type recognition. Journal of Atmospheric and Oceanic Technology 25, 3–14.

Calbó, J., González, J.A., Pagès, D., 2001. A method for sky-condition classification from ground-based solar radiation measurements. Journal of Applied Meteorology 40, 2193–2199 (Notes and Correspondence).

Calbó, J., Pagès, D., González, J.A., 2008. Empirical studies of cloud effects on UV radiation: a review. Reviews of Geophysics 43, 1–28.

Campbell, G.G., Holmlund, K., 2004. Geometric cloud heights from Meteosat. International Journal of Remote Sensing 25, 4505–4519.

Campbell, J.B., Wynne, R.H., 2011. Introduction to Remote Sensing, fifth ed. The Guilford Press, New York.

Casanova, C., Romo, A., Hernández, E., Casanova, J.L., 2010. Operational cloud classification for the Iberian Peninsula using Meteosat Second Generation and AQUA-AIRS image fusion. International Journal of Remote Sensing 31, 93–115.

Cayula, J.F., Cornillon, P., 1996. Cloud detection from a sequence of SST images. Remote Sensing of Environment 88, 80–88.

Cazorla, A., Olmo, F.J., Alados-Arboledas, L., 2008a. Using a sky imager for aerosol characterization. Atmospheric Environment 42, 2739–2745.

Cazorla, A., Olmo, F.J., Alados-Arboledas, L., 2008b. Development of a sky imager for cloud cover assessment. Journal of the Optical Society of America 25, 29–39.

Chernykh, I.V., Eskridge, R.E., 1996. Determination of cloud amount and level from radiosonde soundings. Journal of Applied Meteorology 35, 1362–1369.

Chernykh, I.V., Alduchov, O.A., Eskridge, R.E., 2009. Trends in low and high cloud boundaries and errors in height determination of cloud boundaries. Bulletin American Meteorological Society 82, 1941–1947.

Cheruy, F., Aires, F., 2009. Cluster analysis of cloud properties over the southern European Mediterranean area in observations and a model. Monthly Weather Review 137, 3161–3176.

Chiu, J.C., Marshak, A., Knyazikhin, Y., Wiscombe, W.J., Barker, H.W., Barnard, J.C., Luo, Y., 2006. Remote sensing of cloud properties using ground-based measurements of zenith radiance. Journal of Geophysical Research 111, D16201.

Cho, H.M., Yang, P., Kattawar, G.W., Nasiri, S.L., Hu, Y., Minnis, P., Trepte, C., Winker, D., 2008. Depolarization ratio and attenuated backscatter for nine cloud types: analyses based on collocated CALIPSO LIDAR and MODIS measurements. Optics Express 16, 3931–3948.

Chow, C.W., Urquhart, B., Dominguez, A., Kleissl, J., Shields, J., Washom, B., 2011. Intra-hour forecasting with a total sky imager at the UC San Diego solar energy testbed. Solar Energy 85, 2881–2893.

Christodoulou, C.I., Michaelides, S.C., Pattichis, C.S., Kyriakou, K., 2001. Classification of satellite cloud imagery based on multi-feature texture analysis and neural networks. In: Proceedings of International Conference on Image Processing, Thessaloniki, Greece, pp. 497–500.

Christodoulou, C.I., Michaelides, S.C., Pattichis, C.S., 2003. Multifeature texture analysis for the classification of clouds in satellite imagery. IEEE Transactions on Geoscience and Remote Sensing 41, 2662–2668.

Clark, W.J., 1983. Cloud cover as a factor in the utilization of landsat data for limnological research. Remote Sensing of Environment 13, 453–460.

Clarke, E.T., Korff, S.A., 1941. The radiosonde: the stratosphere laboratory. Journal of the Franklin Institute 232, 217–238.

Clothiaux, E.E., Miller, M.A., Albrecht, B.A., Ackerman, T.P., Verlinde, J., Babb, D.M., Peters, R.M., Syrett, W.J., 1995. An evaluation of a 94-GHZ radar for remote sensing of cloud properties. Journal of Atmospheric and Oceanic Technology 12, 201–229.

Clothiaux, E.E., Mace, G.G., Ackerman, T.P., Kane, T.J., Spinhirne, J.D., Scott, V.S., 1998. An automated algorithm for detection of hydrometeor returns in Micropulse Lidar Data. Journal of Atmospheric and Oceanic Technology 15, 1035–1042 (Notes and Correspondence).

Cloud Appreciation Society, 2011. <www.cloudappreciationsociety.org>.

Centre National d' Etudes Spatiales (CNES), 2011. http://smsc.cnes.fr/.

Col, B., Mouchot, M.C., 1995. Cloud Classification using Passive Microwave Satellite Measurements from the SSMn Radiometer. In: Proceedings of International Geoscience and Remote Sensing Symposium, pp. 1889–1891.

Collet, M., Besnard, T., Zanghi, F., Chan, P.W., Berger, L., Long, C.N., Gillotay, D., 2009. Improvement of algorithm in cloud thermal infrared spectroscopy. In: Proceedings of the 25th Conference on International Interactive Information and Processing Systems (IIPS) for Meteorology, Oceanography, and Hydrology, USA.

Cotton, W.R., Bryan, G.H., Van de Heever, S.C., 2011. Storm and cloud dynamics, second ed.. In: International Geophysics Series, vol. 99 Elsevier, UK.

Davis, G.B., Griggs, D.J., Sullivan, G.D., 1992. Automatic estimation of cloud amount using computer vision. Journal of Atmospheric and Oceanic Technology 9, 81–85.

de Haij, M., Wauben, W., Baltink, H.K., 2006. Determination of mixing layer height from ceilometer backscatter profiles. Proceedings of SPIE 6362.

Deb, S.K., Kishtawal, C.M., Pal, P.K., Joshi, P.C., 2008. A modified tracer selection and tracking procedure to derive winds using water vapor imagers. Journal of Applied Meteorology and Climatology 47, 3252–3263.

Degrand, J.Q., Carleton, A.M., Travis, D.J., Lamb, P.J., 2000. A satellite-based climatic description of jet aircraft contrails and associations with atmospheric conditions, 1977–79. Journal of Applied Meteorology 39, 1434–1458.

Deneke, H.M., Feijt, A.J., Roedebeling, R.A., 2008. Estimating surface solar irradiance from METEOSAT SEVIRI-derived cloud properties. Remote Sensing of Environment 112, 3131–3141.

Dong, C., Yang, J., Zhang, W., Yang, Z., Lu, N., Shi, J., Zhang, P., Liu, Y., Cai, B., 2009. An overview of a new Chinese weather satellite FY-3A. Bulletin of the American Meteorological Society 90, 1531–1544.

Duchon, C.E., O'Malley, M.S., 1999. Estimating cloud type from pyranometer observations. Journal of Applied Meteorology 38, 132–141.

Dupont, J.C., Haeffelin, M., Long, C.N., 2008. Evaluation of cloudless-sky periods detected by shortwave and longwave algorithms using lidar measurements. Geophysical Research Letters 35, L108151–L108154.

Dybbroe, A., Karlsson, K.G., Thoss, A., 2005a. NWCSAF AVHRR cloud detection and analysis using dynamic thresholds and radiative transfer modeling. Part I: Algorithm description. Journal of Applied Meteorology 44, 39–54.

Dybbroe, A., Karlsson, K.G., Thoss, A., 2005b. NWCSAF AVHRR cloud detection and analysis using dynamic thresholds and radiative transfer modeling. Part II: Tuning and validation. Journal of Applied Meteorology 44, 55–71.

Eck, M., Hirsch, T., 2007. Dynamics and control of parabolic trough collector loops with direct steam generation. Solar Energy 81, 268–279.

Egmont-Petersen, M., de Ridder, D., Handels, H., 2002. Image processing with neural networks – a review. Pattern Recognition 35, 2279–2301.

El Chaar, L., Lamont, L.A., El Zein, N., 2011. Review of photovoltaic technologies. Renewable and Sustainable Energy Reviews 15, 2165–2175.

Emck, P., Richter, M., 2008. An upper threshold of enhanced global shortwave irradiance in the troposphere derived from field measurements in tropical mountains. Journal of Applied Meteorology and Climatology 47, 2828–2845.

Emeis, S., Münkel, C., Vogt, S., Müller, W.J., Schäfer, K., 2004. Atmospheric boundary-layer structure from simultaneous SODAR,

RASS, and ceilometer measurements. Atmospheric Environment 38, 273–286.
Estupiñán, J.G., Raman, S., Crescenti, G.H., Streicher, J.J., Barnard, W.F., 1996. Effects of clouds and haze on UV-B radiation. Journal of Geophysical Research 101, 807–816.
European Space Agency, Earthnet Online, 2011. <http://earth.esa.int>.
Feister, U., Gericke, K., 1998. Cloud flagging of UV spectral irradiance measurements. Atmospheric Research 49, 115–138.
Feister, U., Shields, J., Karr, M., Johnson, R., Dehne, K., Woldt, M., 2000. Ground-based cloud images and sky radiances in the visible and near infrared region from whole sky imager measurements. In: Proceedings in Climate Monitoring – Satellite Application Facility Training Workshop Dresden Germany.
Feister, U., Möller, H., Sattler, T., Shields, J., Görsdorf, U., Güldner, J., 2010. Comparison of macroscopic cloud data from ground-based measurements using VIS/NIR and IR instruments at Lindenberg, Germany. Atmospheric Research 96, 395–407.
Flach, P.A., Lachiche, N., 2004. Naive Bayesian classification of structured data. Machine Learning 57, 1–37.
Forsythe, J.M., Vonder Haar, T.H., Reinke, D.L., 2000. Cloud-base height estimates using a combination of meteorological satellite imagery and surface reports. Journal of Applied Meteorology 39, 2336–2347.
Foyo-Moreno, I., Alados, I., Olmo, F.J., Alados-Arboledas, L., 2003. The influence of cloudiness on UV global irradiance (295–385 nm). Agricultural and Forest Meteorology 120, 101–111.
Fukunaga, K., 1999. Introduction to Statistical Pattern Recognition, second ed. Elsevier Academic Press, London, UK.
Gaffen, D.J., Elliot, W.P., 1993. Column water vapor content in clear and cloudy skies. Journal of Climate 6, 2278–2287.
Gao, Y., Zheng, B., Chen, G., Li, Q., 2010. Algorithms for constrained k-nearest neighbor queries over moving object trajectories. Geoinformatica 14, 241–276.
Gao, B.C., Li, R.R., Shettle, E.P., 2011. Cloud remote sensing using midwave IR CO_2 and N_2O slicing channels near 4.5 μm. Remote Sensing 3, 1006–1013.
Getzelman, S.D., 1989. Cloud classification before Luke Howard. Bulletin American Meteorological Society 70, 381–395.
Ghosh, A., Pal, N.R., Das, J., 2006. A fuzzy rule based approach to cloud cover estimation. Remote Sensing of Environment 100, 531–549.
Gillotay, D., Besnard, T., Zanghi, F., 2001. A systematic approach of the cloudcover by thermic infrared measurements. In: Proceedings of the 18th Conference on Weather Analysis and Forecasting, Fort Lauderdale, pp. 292–295.
Giri, R.K., Sharma, R.K., 2011. Atmospheric motion vectors height assignment by IRW and water vapour (H_2O) intercept methods. Indian Journal of Science and Technology 4, 1041–1050.
Glickman, T.S., 2000. Glossary of Meteorology, second ed. American Meteorological Society, Boston.
Gómez-Chova, L., Camps-Valls, G., Calpe-Maravilla, J., Guanter, L., Moreno, J., 2007. Cloud screening algorithm for ENVISAT/MERIS multispectral images. IEEE Transactions on Geoscience and Remote Sensing 45, 4105–4118.
Gómez-Chova, L., Camps-Valls, G., Bruzzone, L., Calpe-Maravilla, J., 2010. Mean map kernel methods for semisupervised cloud classification. IEEE Transactions on Geoscience and Remote Sensing 48, 207–220.
Goodman, A.H., Henderson-Sellers, A., 1988. Cloud detection and analysis: a review of recent progress. Atmospheric Research 21, 203–228.
Hahn, C.J., Warren, S.G., London, J., Cherrin, R.M., Jenne, R., 1982. Atlas of Simultaneous Occurrence of Different Cloud Types Over the Ocean. NCAR Tech. Note TN-2011STR.
Hakn, B.H., Chahine, M.T., Stephens, G.L., Mace, G.G., Marchand, R.T., Wang, Z., Barnet, C.D., Aldering, A., Holz, R.E., Kuehn, R.E., Vane, D.G., 2008. Cloud type comparisons of AIRS, CloudSat and CALIPSO cloud height and amount. Atmospheric Chemistry and Physics 8, 1231–1248.
Halthore, R.N., Eck, T.F., Holben, B.N., Markham, B.L., 1997. Sun photometric measurements of atmospheric water vapor column abundance in the 940-nm band. Journal of Geophysical Research 102, 4343–4352.
Hamada, A., Nishi, N., Kida, H., Shiotani, M., Iwasaki, S., Kamei, A., Ohno, Y., Kuroiwa, H., Kumagai, H., Okamoto, H., 2004. Cloud type classification by GMS-5 infrared split-window measurements with millimeter-wave radar and TRMM-PR observations in the Tropics. In: Proceedings of the 2nd TRMM International Science Conference.
Hammer, A., Heinemann, D., Hoyer, C., Kuhlemann, R., Lorenz, E., Muller, R., Beyer, H., 2003. Solar energy assessment using remote sensing technologies. Remote Sensing of Environment 86, 423–432.
Haralick, R.M., Shanmugam, K., Dinstein, I., 1973. Texture features for image classification. IEEE Transactions of Systems, Man and Cybernetics 3, 610–621.
Harrison, L., Michalsky, J., Berndt, J., 1994. Automated multifilter rotating shadow-band radiometer: an instrument for optical depth and radiation measurements. Applied Optics 33, 5118–5125.
He, Q.J., 2011. A daytime cloud detection algorithm for FY-3A/VIRR data. International Journal of Remote Sensing 32, 6811–6822.
Heinle, A., Macke, A., Srivastav, A., 2010. Automatic cloud classification of whole sky images. Atmospheric Measurement Techniques 3, 557–567.
Hendricks, J., Falbi, A., Stubenrauch, C.L., Emde, C., 2010. A method for comparing properties of cirrus clouds in global climate models with those retrieved from IR sounder satellite observations. Meteorologische Zeitschrift 19, 577–589.
Herrmann, U., Kelly, B., Price, H., 2004. Two-tank molten salt storage for parabolic trough solar power plants. Energy 29, 883–893.
Hirsch, E., Agassi, E., Koren, I., 2011. A novel technique for extracting clouds base height using ground base imaging. Atmospheric Measuring Technology 4, 17–130.
Ho, S.P., Lin, B., Minnis, P., Fan, T.F., 2003. Estimates of cloud vertical structure and water amount over tropical oceans using VIRS and TMI data. Journal of Geophysical Research 108, AAC101–AAC1016.
Hong, Y., Hsu, K.L., Sorooshian, S., Gao, X., 2004. Precipitation estimation from remotely sensed imagery using an artificial neural network cloud classification system. Journal of Applied Meteorology 43, 1834–1852.
Houborg, R., Soegaard, H., Emmerich, W., Moran, S., 2007. Inferences of all-sky solar irradiance using Terra and Aqua MODIS satellite data. International Journal of Remote Sensing 28, 4509–4535.
Howard, L., 1803. On the Modifications of Clouds, third ed. J. Taylor, London.
Hutchison, K.D., Pekker, T., Smith, S., 2006. Improved retrievals of cloud boundaries from MODIS for use in air quality modeling. Atmospheric Environment 40, 5798–5806.
Illingworth, A.J. et al., 2007. CloudNet: continuous evaluation of cloud profiles in seven operational models using ground-based observations. Bulletin American Meteorological Society 88, 883–898.
Irish, R.R., Barker, J.L., Goward, S.N., Arvidson, T., 2006. Characterization of the landsat-7 ETM+ automated cloud-cover assessment (ACCA) algorithm. Photogrammetric Engineering & Remote Sensing 72, 1179–1188.
ISO 9060:1990. Solar Energy – Specification and Classification of Instruments for Measuring Hemispherical Solar and Direct Solar radiation <http://www.iso.org/iso/catalogue_detail.htm?csnumber=16629>.
Janeiro, F.M., Ramos, P.M., Wagner, F., Silva, A.M., 2010. Developments of low-cost procedure to estimate cloud base height based on a digital camera. Measurements 43, 684–689.
Japan Aerospace Exploration Agency (JAXA), 2011. <http://www.jaxa.jp/index_e.html>.
Jedlovec, G., 2009. Automated detection of clouds in satellite imagery. Advances in Geoscience and Remote Sensing, 303–316.
Jedlovec, G., Haines, S., 2008. Spatial and temporal varying thresholds for cloud detection in GOES imagery. IEEE Transactions on Geoscience and Remote Sensing 46, 1705–1717.

Jian, L., Jianmin, X., 2008. An Automated, Dynamic Threshold Cloud Detection Algorithm for FY-2C Images. National Satellite Meteorological Center, Beijing, China.

Jin, X., Hanesiak, J., Barber, D., 2007. Detecting cloud vertical structures from radiosondes and MODIS over Arctic first-year sea ice. Atmospheric Research 83, 64–76.

Johnson, R., Hering, W., Shields, J., 1989. Automated Visibility and Cloud Cover Measurements with a Solid-state Imaging System. Tech. Rep., University of California, San Diego, Scripps Institution of Oceanography, Marine Physical Laboratory, SIO Ref. 89-7, GL-TR-89-0061, 128 pp.

Joiner, J., Vasilkov, A.P., Bhartia, P.K., Wind, G., Platnick, S., Menzel, W.P., 2010. Detection of multi-layer and vertically-extended clouds using A-train sensors. Atmospheric Measurement Techniques 3, 2333–2347.

Kaskaoutis, D.G., Kambezidis, H.D., Kharol, S.K., Badarinath, K.V.S., 2008. The diffuse-to-global spectral irradiance ratio as a cloud-screening technique for radiometric data. Journal of Atmospheric and Solar-Terrestrial Physics 70, 1597–1606.

Kassianov, E., Long, C.N., Christy, J., 2005. Cloud-base-height estimation from paired ground-based hemispherical observations. Journal of Applied Meteorology 44, 1221–1233.

Kassianov, E., Barnard, J., Berg, L.K., Flynn, C., Long, C.N., 2011a. Sky cover from MFRSR observations: cumulus clouds. Atmospheric Measurements Techniques Discussions 4, 715–735.

Kassianov, E., Barnard, J., Berg, L.K., Flynn, C., Long, C.N., 2011b. Sky cover from MFRSR observations. Atmospheric Measurements Techniques 4, 1463–1470.

Kasten, F., Czeplak, G., 1980. Solar and terrestrial radiation dependent on the amount and type of cloud. Solar Energy 24 (177), 189.

Kato, S., Mace, G.G., Clothiaux, E.E., Liljegren, J.C., Austin, R.T., 2001. Doppler cloud radar derived drop size distributions in liquid water stratus clouds. Journal of Atmospheric Sciences 58, 2895–2911.

Kegelmeyer Jr., W.P., 1994. Extraction of Cloud Statistics from Whole Sky Imaging Cameras. SANDIA Report. SAND94-8222, pp. 1–14.

Key, J.R., Maslanik, J.A., Barry, R.G., 1989. Cloud classification from satellite data using a fuzzy sets algorithm: a polar example. International Journal of Remote Sensing 10, 1823–1842.

Kiedron, P., Schlemmer, J., Klassen, M., 2006. Rotating Shadowband Spectroradiometer (RSS) Handbook. ARM TR-051, U.S. Department of Energy.

Kim, J.E., Ryu, S.Y., He, Z., Kim, Y.J., 2006. Spectral aerosol optical depth variation with different types of aerosol at Gwangju, Korea. Journal of Atmospheric and Solar Terrestrial Physics 68, 1609–1621.

Kohavi, R., Provost, F., 1998. Glossary of terms. Machine Learning 30, 271–274.

Kohonen, T., 1982. Self organized formation of topologically correct feature maps. Biological Cybernetics 43, 59–69.

Kokhanovsky, A., 2004. Optical properties of terrestrial clouds. Earth-Science Reviews 64, 189–241.

Kollias, P., Clothiaux, E.E., Miller, M.A., Albrecht, B.A., Stephens, G.L., Ackerman, T.P., 2007. Millimeter-wavelength radars: new frontier in atmospheric cloud and precipitation research. Bulletin of the American Meteorological Society 88, 1608–1624.

Kongtragool, B., Wongwises, S., 2003. A review of solar-powered Stirling engines and low temperature differential Stirling engines. Renewable and Sustainable Energy Reviews 7, 131–154.

Kubota, T., Kachi, M., Oki, R., Shimizu, S., Yoshida, N., Kojima, M., Nakamura, K., 2010. Rainfall observation from space-applications of tropical rainfall measuring mission (TRMM) and global precipitation measurement (GPM) mission. International Archives of the Photogrammetry, Remote Sensing and Spatial Information Science 38, 63–73.

Lafont, D., Jourdan, O., Guillemet, B., 2006. Mesoscale cloud pattern classification over ocean with a neural network using a new index of cloud variability. International Journal of Remote Sensing 27, 3533–3552.

Lavanant, L., Fourrié, N., Gambacorta, A., Grieco, G., Heilliette, S., Hilton, F.I., Kim, M.J., McNally, A.P., Nishihata, H., Pavelin, E.G., Rabier, F., 2011. Comparison of cloud products within IASI footprints for the assimilation of cloudy radiances. Quarterly Journal of the Royal Meteorological Society, http://dx.doi.org/10.1002/qj.917.

Lee, Y., Wahba, G., Ackerman, S.A., 2004. Cloud classification of satellite radiance data by multicategory support vector machines. Journal of Atmospheric and Oceanic Technology 21, 159–169.

Lester, A., Myers, D.R., 2006. A method for improving global pyranometer measurements by modeling responsivity functions. Solar Energy 80, 322–331.

Levelt, P.F., Van den Oord, G.H.J., Dobber, M.R., Mälkki, A., Visser, H., de Vries, J., Stammes, P., Lundell, J.O.V., Saari, H., 2006. The ozone monitoring instrument. IEEE Transaction on Geoscience and Remote Sensing 44, 1093–1101.

Li, J., Menzel, W.P., Yang, Z., Frey, R.A., Ackerman, S.A., 2003. High-spatial-resolution surface and cloud-type classification from MODIS multispectral band measurements. Journal of Applied Meteorology 42, 204–226.

Li, Z., Li, J., Menzel, W.P., Schmit, T.J., Ackerman, S.A., 2007. Comparison between current and future environmental satellite imagers on cloud classification using MODIS. Remote Sensing of Environment 108, 311–326.

Li, D., Dong, X., Liu, L., Xiang, D., 2008. A new cloud detection algorithm for FY-2C images over China. In: Proceedings of the Workshop on Knowledge Discovery and Data Mining, pp. 289–292.

Liu, G., Curry, J.A., Sheu, R.S., 1995. Classification of clouds over the western equatorial Pacific Ocean using combined infrared and microwave satellite data. Journal of Geoscience Research 100, 811–826.

Liu, C., Zisper, E.Z., Cecil, D.J., Nesbitt, S.W., Sherwood, S., 2008. A cloud and precipitation feature database from nine years of TRMM observations. Journal of Applied Meteorology and Climatology 47, 2712–2728.

Liu, Y., Xia, J., Shi, C.X., Hong, Y., 2009. An improved cloud classification algorithm for China's FY-2C multi-channel images using artificial neural network. Sensors 9, 5558–5579.

Liu, L., Sun, X., Chen, F., Zhao, S., Gao, T., 2011. Cloud classification based on structure features of infrared images. Journal of Atmospheric and Oceanic Technology 28, 410–417.

Long, C.N., 2010. Correcting for circumsolar and near-horizon errors in sky cover retrievals from sky images. The Open Atmospheric Science Journal 4, 45–52.

Long, C.N., Sabburg, J., Calbó, J., Pagès, D., 2006. Retrieving cloud characteristics from ground-based daytime color all-sky images. Journal of Atmospheric and Oceanic Technology 23, 633–652.

Loyola, D.G.R., Thomas, W., Spurr, R., Mayer, B., 2010. Global patterns in daytime cloud properties derived from GOME backscatter UV–VIS measurements. International Journal of Remote Sensing 31, 4295–4318.

Macías, M.M., Aligué, J.L., Pérez, A.S., Vivas, A.A., 2001. A comparative study of two neural models for cloud screening of Iberian Peninsula Meteosat images. In: Proceedings of the International Work Conference on Artificial and Neural Networks, pp. 184–191.

Maghrabi, A., Clay, R., Wild, N., Dawson, B., 2009. Design and development of a simple infrared monitor for cloud detection. Energy Conversion and Management 50, 2732–2737.

Mahesh, A., Walden, V.P., Warren, S.G., 2001. Ground-based infrared remote sensing of cloud properties over the Antarctic Plateau. Part I: Cloud-base heights. Journal of Applied Meteorology 40, 1265–1278.

Manoj, S.O., Kavitha, V., Arul, J.S., 2010. Recognizing the cloud type and estimation of rainfall. In: Proceedings of the International Conference on Communication and Computational Intelligence, India, pp. 178–183.

Marais, I.V.Z., du Preez, J.A., Steyn, W.H., 2011. An optimal image transform for threshold-based cloud detection using heteroscedastic discriminant analysis. International Journal of Remote Sensing 32, 1713–1729.

Martínez-Chico, M., Batlles, F.J., Bosch, J.L., 2011. Cloud classification in a Mediterranean location using radiation data and sky images. Energy 36, 4055–4062.

Martner, B.E., Bartram, B.W., Gibson, J.S., Campbell, W.K., Reinking, R.F., Matrosov, S.Y., 2002. An overview of NOAA/ETL'S scanning Ka-band cloud radar. In: Preprints, 16th Conf. on Hydrology, Orlando, FL, American Meteorology Society, pp. 102–103.

Martucci, G., Milroy, C., O'Dowd, C.D., 2010. Detection of Cloud-Base Height using Jenoptik CHM15K and Vaisala CL31 ceilometers. Journal of Atmospheric and Oceanic Technology 27, 305–318.

Massons, J., Domingo, D., Grau, J., 1996. Automatic classification of VIS-IR METEOSAT images. Computers & Geosciences 22, 1137–1146.

Mayer, B., Kylling, A., Madronich, S., Seckmeyer, G., 1998. Enhanced absorption of UV radiation due to multiple scattering in clouds: experimental evidence and theoretical explanation. Journal of Geophysical Research 103, 241–254.

Mazzetti, P., Nativi, S., Giuli, D., 2001. Case-study on the use of microwave sensors for cloud detection over Tuscany. In: Proceedings of IEEE International Geoscience and Remote Sensing Symposium, Sydney, pp. 1055–1057.

Mazzoni, D., Horváth, A., Garay, M., Tang, B., Davies, R., 2005. A MISR cloud-type classifier using reduced support vector machines. Proceedings of the Eighth Workshop on Mining Scientific and Engineering Datasets. SIAM.

Mazzoni, D., Garay, M.J., Davies, R., Nelson, D., 2007. An operational MISR pixel classifier using support vector machines. Remote Sensing of Environment 107, 149–158.

Mckenzie, R.L., Paulin, K.J., Bodeker, G.E., Liley, J.B., Sturman, A.P., 1998. Cloud cover measured by satellite and from the ground: relationship to UV radiation at the surface. International Journal of Remote Sensing 19, 2969–2985.

Mecikalski, J.R., Watts, P.D., Koenig, M., 2011. Use of Meteosat Second Generation optimal cloud analysis fields for understanding physical attributes of growing cumulus clouds. Atmospheric Research 102, 175–190.

Medrano, M., Gil, A., Martorell, I., Potau, X., Cabeza, L.F., 2010. State of the art on high-temperature thermal energy storage for power generation. Part 2 – Case studies. Renewable and Sustainable Energy Reviews 14, 56–72.

Mellit, A., Kalogirou, S.A., 2008. Artificial intelligence techniques for photovoltaic applications: a review. Progress in Energy and Combustion Science 34, 574–632.

Mendoza, A., Flynn, C., 2006. Micropulse Lidar (MPL) Handbook, ARM TR-019, U.S. Department of Energy (2006).

Menzel, W.P., 2001. Cloud tracking with satellite imagery: from the pioneering work of Ted Fujita to the present. Bulletin of the American Meteorological Society 82, 33–47.

Menzel, W.P., Frey, R.A., Zhang, H., Wylie, D.P., Moeller, C.C., Holz, R.E., Maddux, B., Baum, B.A., Strabala, K.I., Gumley, L.E., 2008. MODIS global cloud-top pressure and amount estimation: algorithm description and results. Journal of Applied Meteorology and Climatology 47, 1175–1198.

Merchant, C.J., Harris, A.R., Maturi, E., MacCallum, S., 2005. Probabilistic physically based cloud screening of satellite infrared imagery for operational sea surface temperature retrieval. Quarterly Journal of the Royal Meteorological Society 131, 2735–2755.

Michalsky, J.J., Min, Q., Kiedron, P.W., Slater, D.W., Barnard, J.C., 2001. A differential technique to retrieve column water vapor using sun radiometry. Journal of Geophysical Research 106, 433–442.

Michie, D., Spiegelhalter, D.J., Taylor, C.C., 1994. Machine Learning, Neural and Statistical Classification. Ellis Horwood, Upper Saddle River, NJ, USA.

Miller, S.W., Emery, W.J., 1997. An automated neural network cloud classifier for use over land and ocean surfaces. Journal of Applied Meteorology 36, 1346–1362.

Mills, P., 2011. Efficient statistical classification of satellite measurements. International Journal of Remote Sensing 32 (2011), 1–24.

Mills, A., Ahlstrom, M., Brower, M., et al., 2009. Understanding Variability and Uncertainty of Photovoltaics for Integration with the Electric Power System. USDOE, Lawrence Berkeley National Laboratory.

Min, Q., Wang, T., Long, C.N., Duan, M., 2008. Estimating fractional sky cover from spectral measurements. Journal of Geophysical Research 113, D20.

Minnis, P., Ayers, J.K., Paliconda, R., Phan, D., 2004. Contrails, cirrus trends, and climate. Journal of Climate 17, 1671–1685.

Minnis, P., Yi, Y., Huang, J., Ayers, K., 2005. Relationships between radiosonde and RUC-2 meteorological conditions and cloud occurrence determined from ARM data. Journal of Geophysical Research 110, D23204.

Minnis, P., Trepte, Q.Z., Sun-Mack, S., Chen, Y., Doelling, D.R., Young, D.F., Spangenberg, D.A., Miller, W.F., Wielicki, B.A., Brown, R.R., Gibson, S.C., Geier, E.B., 2008. Cloud detection in nonpolar regions for CERES using TRMM VIRS and Terra and Aqua MODIS data. IEEE Transaction on Geoscience and Remote Sensing 46, 3857–3884.

Morris, V., Klebe, D., 2010. A demonstration of the Solmirus all sky infrared visible analyzer. Poster presented in ASR Science Team Meeting.

Mukherjee, D.P., Acton, S.T., 2002. Cloud tracking by scale space classification. IEEE Transactions on Geoscience and Remote Sensing 40, 405–415.

Murtagh, F., Barreto, D., Marcello, J., 2003. Decision boundaries using Bayes factors: the case of cloud masks. IEEE Transactions on Geoscience and Remote Sensing 41, 2952–2958.

National Aeronautics and Space Administration – MODIS Web, 2011. <http://modis.gsfc.nasa.gov/>.

National Oceanic and Atmospheric Administration's – National Weather Service, 2011. <http://www.nws.noaa.gov/>.

National Oceanic and Atmospheric Administration's – Office of Satellite Operations, 2011. <http://www.oso.noaa.gov/>.

Newson, R.K., 2009. Raman Lidar (RL) Handbook. ARM TR-038, U.S. Department of Energy.

Nowak, D., Ruffieux, D., Agnew, J.L., Vuilleumier, L., 2008. Detection of fog and low cloud boundaries with ground-based remote sensing systems. Journal of Atmospheric and Oceanic Technology 25, 1357–1368.

National Snow and Ice Data Center (NSIDC), 2011. <http://www.nsidc.org/>.

Ocelíková, E., Krištof, J., 2001. Classification of multispectral data. Journal of Information and Organizational Sciences 25, 35–41.

Ododo, J.C., Agbakwuru, J.A., Ogbu, F.A., 1996. Correlation of solar radiation with cloud cover and relative sunshine duration. Energy Conversation and Management 37, 1555–1559.

Orsini, A., Tomas, C., Calzolari, F., Nardino, M., Cacciari, A., Georgiadis, T., 2002. Cloud cover classification through simultaneous ground-based measurements of solar and infrared radiation. Atmospheric Research 61, 251–275.

Orun, A.B., Natarajan, K., Aslan, Z., 2000. A Comparative study of meteosat, ECMWF, and radiosonde wind vectors at Istanbul. Remote Sensing of Environment 72, 309–316.

Pagès, D., Calbó, J., González, J.A., 2003. Using routine meteorological data to derive sky conditions. Annales Geophysicae 21, 649–654.

Paliwal, M., Kumar, U.A., 2009. Neural networks and statistical techniques: a review of applications. Expert Systems with Applications 36, 2–17.

Parida, B., Iniyanb, S., Goic, R., 2011. A review of solar photovoltaic technologies. Renewable and Sustainable Energy Reviews 15, 1625–1636.

Parikh, J., 1977. A comparative study of cloud classification techniques. Remote Sensing on Environment 6, 67–81.

Parikh, J., 1978. Cloud classification from visible and infrared SMS-1 data. Remote Sensing of Environment 7, 85–92.

Parikh, J.A., Ball, J.T., 1980. Analysis of cloud type and cloud amount during GATE from SMS infrared data. Remote Sensing on Environment 9, 225–245.

Parisi, A., Downs, N., 2004. Variation of the enhanced biologically damaging solar UV due to clouds. Photochemical and Photobiological Sciences 3, 643–647.

Parisi, A.V., Sabburg, J., Turner, J., Dumn, P.K., 2008. Cloud observations for the statistical evaluation of the UV index at Toowoomba, Australia. International Journal of Biometeorology 52, 159–166.

Partamies, N., 2004. Meso-scale Auroral Physics from Ground-based Observations. Ph.D. Dissertation, Dept. of Physical sciences, University of Helsinki, Finland.

Petty, G.W., 2006. A First Course in Atmospheric Radiation, second ed. Sundog Publishing, Madison, Wisconsin.

Pfister, G., McKenzie, R.L., Liley, J.B., Thomas, A., Forgan, B.W., Long, C.N., 2003. Cloud coverage based on all-sky imaging and its impact on surface solar irradiance. Journal of Applied Meteorology 42, 1421–1434.

Piacentini, R.D., Saluma, G.M., Fraidenraich, N., Tibad, C., 2011. Extreme total solar irradiance due to cloud enhancement at sea level of the NE Atlantic coast of Brazil. Renewable Energy 36, 409–412.

Poyer, A.J., 2008. Evaluation of an MPL cloud detection algorithm as a reference for ceilometer testing within the ASOS PI program. In: The 88th American Meteorological Society Annual Meeting, New Orleans, USA.

Prakash, S., Mahesh, C., Mishra, A., Gairola, R.M., Varma, A.K., Pal, P.K., 2009. Combined use of microwave and IR data for the study of Indian monsoon rainfall. In: Proceedings of Impact of Climate Change on Agriculture Workshop, XXX-VIII-8/W3, pp. 227–230.

Pretorius, J.P., Kroger, D.G., 2006. Critical evaluation of solar chimney power plant performance. Solar Energy 80, 535–544.

Pujol, O., Georgis, J.F., Féral, L., Sauvageot, H., 2007. Degradation of radar reflectivity by cloud attenuation at microwave frequency. Journal of Atmospheric and Oceanic Technology 24, 640–657.

Randriamampianina, R., Nagy, J., Balogh, T., Kerényi, J., 2000. Determination of cloud top height using meteorological satellite and radar data. Physics and Chemistry of the Earth 25, 1103–1106.

Ricciardelli, E., Romano, F., Cuomo, V., 2008. Physical and statistical approaches for cloud identification using Meteosat second generation-spinning enhanced visible and infrared imager data. Remote Sensing of Environment 112, 2741–2760.

Ricciardelli, E., Romano, F., Cuomo, V., 2010. A technique for classifying uncertain MOD35/MYD35 pixels through Meteosat second generation-spinning enhanced visible and infrared imager observations. IEEE Transactions on Geoscience and Remote Sensing 48, 2137–2149.

Richards, J.A., Jia, X., 1999. Remote Sensing Digital Image Analysis: An Introduction, third ed. Springer-Verlag, Germany.

Richards, K., Sullivan, G.D., 1992. Estimation of cloud cover using colour and texture. In: Proceedings of the British Machine Vision Conference (BMVC), pp. 436–442.

Rodriguez, D., 1998. On the Comparability of Cloud Fractions Derived from Whole Sky Imager and Ceilometer Data. Lawrence Livermore National Laboratory.

Rogalski, A., Chrzanowski, K., 2002. Infrared devices and techniques. Opto-Electronics Review 10, 111–136.

Rogers, R.P., Yau, M.K., 1989. A Short Course in Cloud Physics, third ed. Pergamon Press, Elmsford, NY.

Roy, G., Hayman, S., Julian, W., 2001. Sky analysis from CCD images: cloud cover. Lighting Research and Technology 33, 211–222.

Ruprecht, E., 1985. Statistical approaches to Cloud Classification. Advances in Space Research 5, 151–164.

Sabburg, J., Calbó, J., 2009. Five years of cloud enhanced surface UV radiation measurements at two sites (in the Northern and Southern Hemispheres). Atmospheric Research 93, 902–912.

Sabburg, J., Wong, J., 1999. Evaluation of a ground-based sky camera system for use in surface irradiance measurement. Journal of Atmospheric and Ocean Technology 16, 752–759.

Saitwal, K., 2006. A multichannel temporally adaptive system for continuous cloud classification from satellite imagery. IEEE Transactions on Geoscience and Remote Sensing 41, 1098–1104.

Schmetz, J., Klaes, D., König, M., Holmlund, K., 2007. Monitoring weather and climate with the Meteosat and Metop satellites. Revista de Teledetección 27, 5–16.

Schmid, J., 2000. The SEVIRI instrument. In: Proceedings of the 2000 EUMETSAT Meteorological Satellite Data Users' Conference, Bologna, Italy, pp. 23–32.

Schneider, W., Yamanouchi, T., Watanabe, O., Nishio, F., Masuko, H., 1994. Classification of MOS-1 VTIR images in the Antarctic, a case study. International Journal of Remote Sensing 15, 3675–3691.

Sebag, J., Krabbendam, V.L., Claver, C.F., Andrew, J., Barr, J.D., Klebe, D., 2008. LSST IR camera for cloud monitoring and observation planning. In: SPIE Proceedings, vol. 7012.

Sedano, F., Kempeneers, P., Strobl, P., Kucera, J., Vogt, P., Seebach, L., San-Miguel-Ayanz, J., 2011. A cloud mask methodology for high resolution remote sensing data combining information from high and medium resolution optical sensors. ISPRS Journal of Photogrammetry and Remote Sensing 66, 588–596.

Seiz, G., Baltsavias, E.P., Gruen, A., 2002. Cloud mapping from the ground: use of photogrammetric methods. Programmetric Engineering & Remote Sensing 68, 941–951.

Seiz, G., Shield, J., Feister, U., Baltsavias, E.P., Gruen, A., 2007. Cloud mapping with ground based photogrammetric cameras. International Journal of Remote Sensing 28, 2001–2032.

Sharma, A., Tyagi, V.V., Chen, C.R., Buddhi, D., 2009. Review on thermal energy storage with phase change materials and applications. Renewable and Sustainable Energy Reviews 13, 318–345.

Shaw, J.A., Thurairajah, B., 2005. Cloud statistics measured with the infrared cloud imager (ICI). IEEE Transactions on Geoscience and Remote Sensing 43, 2000–2007.

Shaw, J.A., Thurairajah, B., Edqvist, E., Mizutani, K., 2002. Infrared cloud imager deployment at the north slope of alaska during early 2002. In: Proceedings of the Twelfth ARM Science Team Meeting, St. Petersburg, Florida, pp. 1–7.

Shi, C., Zhang, W., Guo, W., Zhang, L., 2005. Study on cloud classifications by using AVHRR, GMS-5 and Terra/MODIS satellite data. In: Proceedings of fourteenth International TOVS Study Conference, Beijing, China.

Shi, T., Clothiaux, E.E., Yu, B., Braverman, A.J., Groff, D.N., 2007. Detection of daytime arctic clouds using MISR and MODIS data. Remote Sensing of Environment 107, 172–184.

Shields, J., Johnson, R., Karr, M., Wertz, J., 1998. Automated day/night whole sky imagers for field assessment of cloud cover distributions and radiance distributions. Tenth Symposium on Meteorological Observations and Instrumentation. American Meteorological Society.

Shields, J., Karr, M., Burden, A., Johnson, R., Mikuls, V., Streeter, J., Hodgkiss, W., 2009. Research toward Multi-Site Characterization of Sky Obscuration by Clouds. Marine Physical Laboratory, Scripps Institution of Oceanography, University of California San Diego, Technical Note 274.

Singh, M., Glennen, M., 2005. Automated ground-based cloud recognition. Pattern Analysis & Applications 8, 258–271.

Slater, D.W., Long, C.N., Tooman, T.P., 2001. Total sky imager/whole sky imager cloud fraction comparison. In: Proceedings of the Eleventh ARM Science Team Meeting, Atlanta, Georgia, pp. 1–11.

Smith, S., Toumi, R., 2008. Measuring cloud cover and brightness temperature with a ground-based thermal infrared camera. Journal of Applied Meteorology and Climatology 47, 683–693.

Souza-Echer, M.P., Pereira, E.B., Bins, L.S., Andrade, M.A.R., 2006. A simple method for the assessment of the cloud cover state in high-latitude regions by a ground-based digital camera. Journal of Atmospheric and Oceanic Technology 23, 437–447.

Stephens, G.L., Vane, D.G., Boain, R.J., Mace, G.G., Sassen, K., Wang, Z., Illingworth, A.J., O'Connor, E.J., Rossow, W.B., Durden, S.L., Miller, S.D., Austin, R.T., Benedetti, A., Mitrescu, C., CloudSat Science Team, 2002. The CloudSAT mission and the A-train – a new dimension of space-based observations of clouds and precipitation. Bulletin of the American Meteorological Society 83, 1771–1790.

Stowe, L.S., Davis, P.A., McClain, E.P., 1999. Scientific basis and initial evaluation of the CLAVR-1 global clear/cloud classification algorithm for the advanced very high resolution radiometer. Journal of Atmospheric and Oceanic Technology 16, 656–681.

Stubenrauch, C.J., Cros, S., Lamquin, N., Armante, R., Chédin, A., Crevoisier, C., Scott, N.A., 2008. Cloud properties from atmospheric infrared sounder and evaluation with cloud-aerosol Lidar and infrared pathfinder satellite observations. Journal of Geophysical Research 113, D00A101–D00A1017.

Syrjäsuo, M., 1996. All-sky Camera. M.Sc. Thesis, Dept. of Electrical Engineering, University of Helsinki, Finland.

Szantai, A., Désalmand, F., Desbois, M., 2002. A method for the construction of cloud trajectories from series of satellite images. International Journal of Remote Sensing 23, 1699–1732.

Tag, P.M., Bankert, R.L., Brody, L.R., 2000. An AVHRR multiple cloud-type classification package. Journal of Applied Meteorology 39, 125–134.

Thirugnanasambandam, M., Iniyan, S., Goic, R., 2010. A review of solar thermal technologies. Renewable and Sustainable Energy Reviews 14, 312–322.

Tian, B., Shaikh, M.A., Azimi-Sadjadi, M.R., Vonder Haar, T.H., Reinke, D.L., 1999. A study of cloud classification with neural networks using spectral and textural features. IEEE Transaction of Neural Networks 10, 138–151.

Tian, B., Azimi-Sadjadi, M.R., Vonder Haar, T.H., Reinke, D., 2000. Temporal updating scheme for probabilistic neural network with application to satellite cloud classification. IEEE Transaction of Neural Networks 11, 903–920.

Tokuno, M., Tsuchiya, K., 1994. Classification of cloud types based on data of multiple satellite sensors. Advances in Space Research 14, 199–206.

Tooman, T.P., 2003. Whole Sky Imager Retrieval Guide, DOE/SC-ARM/TR-011, U.S. Department of Energy.

Tsuchiya, K., Tokuno, M., 1992. Comparison of different sensor data and characteristics of cirrus clouds. Advances in Space Research 12, 343–352.

Tuinder, O.N.E., de Winter-Sorkina, R., Builtjes, P.J.H., 2002. Retrieval methods of effective cloud cover for the GOME instrument: an intercomparisson. Atmospheric Chemistry and Physics Discussions 2, 623–668.

Turner, D.D., Goldsmith, J.E.M., 1999. Twenty-four-hour Raman lidar water vapor measurements during the atmospheric radiation measurement program's 1996 and 1997 water vapor intensive observation periods. Journal of Atmospheric and Oceanic Technology 16, 1062–1076.

Uddstrom, M.J., Warreb, R.G., 1996. Satellite Cloud Classification and rain-rate estimation using multispectral Radiances and measures of special texture. Journal of Applied Meteorology 35, 839–858.

Ulgen, K., Hepbasli, A., 2004. Solar radiation models. Part 1: A review. Energy Sources 26, 507–520.

Vasaras, A., Bais, A.F., Feister, U., Zerefos, C.S., 2001. Comparison of two methods for cloud flagging of spectral UV measurements. Atmospheric Research 57, 31–42.

Vasquez, T., 1989. International Weather Watchers Observation Handbook. Weather Graphics Technologies, Washington, DC, USA.

Villán, D.M., de Miguel Castrillo, A., Santos, J.B., 2010. Empirical models of UV total radiation and cloud effect study. International Journal of Climatology 30, 1407–1415.

Vúrostková, J., Ocelíková, E., Klimešová, D., 2008. Simple and composed classifiers used for classification of experimental data. In: 6th International Symposium on Applied Machine Intelligence and Informatics, SAMI, pp. 25–28.

Wang, L., Dessler, A.E., 2006. Instantaneous cloud overlap statistics in the tropical area revealed by ICESat/GLAS data. Geophysical Research Letters 33, L15804.

Wang, Z., Sassen, K., 2001. Cloud type and macrophysical property retrieval using multiple remote sensors. Journal of Applied Meteorology 40, 1665–1681.

Wang, Z., Sassen, Z., 2004. An improved cloud classification algorithm based on the SGP CART site observations. In: Proceedings of the Fourteenth ARM Science Team Meeting, Albuquerque, New Mexico, pp. 1–11.

Wang, J., Azimi-Sadjadi, M.R., Reinke, D., 2004. A temporally adaptive classifier for multispectral imagery. IEEE Transactions on Neural Networks 15, 159–165.

Waquet, F., Riedi, J., Labonnote, L.C., Goloub, P., Cairns, B., Deuzé, J.L., Tanré, D., 2009. Aerosol remote sensing over clouds using A-train observations. Journal of Atmospheric Sciences 66, 2468–2480.

Wauben, W., 2006. Evaluation of the Nubiscope. Instrumental Department, INSA-IO, KNMI Royal Netherlands Meteorological Institute.

Weng, Q., 2011. Advances in Environmental Remote Sensing Sensors, Algorithms, and Applications. CRC Press, Taylor & Francis Group.

Wind, G., Platnick, S., King, D.K., Hubanks, P.A., Pavolonis, M.J., Heidinger, A.K., Yang, P., Baum, B.A., 2010. Multilayer cloud detection with the MODIS near-infrared water vapor absorption band. Journal of Applied Meteorology and Climatology 49, 2315–2333.

Winiecki, S., Frederick, J.E., 2005. Ultraviolet radiation and clouds: couplings to tropospheric air quality. Journal of Geophysical Research 110, D222021–D222028.

Wittmann, M., Breitkreuz, H., Schroedter-Homscheidt, H., Eck, M., 2008. Case studies on the use of solar irradiance forecast for optimized operation strategies of solar thermal power plants. IEEE Journal of Selected Topics in Applied Earth Observations and Remote Sensing 1, 18–27.

World Meteorological Organization, 1956. International Cloud Atlas, vol. 1, Geneva.

World Meteorological Organization, 2008. Guide to Meteorological Instruments and Methods of Observation, WMO-No. 8, seventh ed., Switzerland.

World Meteorological Organization, 2011. <http://www.wmo.int/>.

Wylie, D.P., Menzel, W.P., 1989. Two years of cloud cover statistics using VAS. Journal of Climate 2, 380–392.

Wylie, D.P., Menzel, W.P., 1999. Eight years of high cloud statistics using HIRS. Journal of Climate 12, 170–184.

Xiong, X., Chiang, K., Sun, J., Barnes, W.L., Guenther, B., Salomonson, V.V., 2008. NASA EOS Terra and Aqua MODIS on-orbit performance. Advances in Space Research 43, 413–422.

Yang, Z.R., 2010. Machine Learning Approaches to Bioinformatics. World Scientific Publishing Co. Pte. Ltd., London.

Zhang, J., Chen, H., Li, Z., Fan, X., Peng, L., Yu, Y., Cribb, M., 2010. Analysis of cloud layer structure in Shouxian, China using RS92 radiosonde aided by 95 GHz cloud radar. Journal of Geophysical Research 115, 1–13.

Zhang, C., Yu, F., Wang, C., Yang, J., 2011. Three-dimensional extension of the unit-feature spatial classification method for cloud type. Advances in Atmospheric Sciences 28, 601–611.

Zhou, X., Wang, F., Ochieng, R.M., 2010. A review of solar chimney power technology. Renewable and Sustainable Energy Reviews 14, 2315–2338.